Generation of dark matter in the early universe from BSM models

Dissertation

zur

Erlangung des Doktorgrades (Dr. rer. nat.)

der

Mathematisch-Naturwissenschaftlichen Fakultät

der

Rheinischen Friedrich-Wilhelms-Universität Bonn

vorgelegt von

Ernany Rossi Schmitz

aus

Farroupilha, Brasilien

Bonn 2018

Angefertigt mit Genehmigung der Mathematisch-Naturwissenschaftlichen Fakultät der Rheinischen Friedrich-Wilhelms-Universität Bonn

1. Gutachter: Prof. Dr. Manuel Drees
2. Gutachter: Prof. Dr. Herbert Karl Dreiner

Tag der Promotion: 08.10.2018
Erscheinungsjahr: 2018

Universität Bonn

Physikalisches Institut

Generation of dark matter in the early universe from BSM models

Ernany Rossi Schmitz

For several decades the nature of Dark Matter (DM) has been elusive to physics. Explanations for its evidences have been stacked up and most of them require new particle physics. In this work, we explore the standard thermal WIMP DM scenario as well as a non-thermal alternative for DM production. For the former framework, we introduce the foundations for its understanding: the FLRW metric for an isotropic and homogeneous universe, the Λ-CDM cosmological model and thermodynamics of the early universe. We also present theoretical tools such as the Boltzmann equation for the DM relic density calculation, after which experimental detection tests are discussed. Two applications of the thermal WIMP scenario are dealt with: (i) a study of a more precise calculation of the Standard Model (SM) degrees of freedom, discussing thereafter the impact of that evaluation on the DM relic density calculation in a model-independent way, comparing it to indirect detection tests; (ii) a BSM (Beyond SM) model with a $B - L$ extension, in which the possibility of a fermionic majorana DM is considered, and the cross section of the candidate is compared with spin-independent direct detection upper bounds.
In the end we explore the nonthermal scenario, where we consider fields motivated by string theory, the KL sector. Therein we introduce the feature of uplifting, whereby the AdS originated solely by the KL potential can be lifted to the dS vacuum by the addition of the ISS sector. Afterwards, the ISS fields oscillations and their subsequent decays are analyzed within a context of small entropy production as well as sufficient neutralino DM generation.

"Why are you truthful?"

Acknowledgements

I would like to thank Prof. Manuel Drees for the opportunity of being part of his group, and for the possibility of learning and working in this field of theoretical physics. I also would like to thank my former or current members of the group, Fazlollah, Raghuveer, Paulina, Bardia, Masaki, Manimala, Felipe, Zhong Yi, Meng Shi and Swasti for the enjoyable atmosphere and kindness. Special thanks to my former or current officemates Paul Oehlmann, Rahul Mehra and Yong Xu for sharing their time with me.

I thank my father, mother and brother for their love and caring, people who make life much more bearable. Many thanks to my longtime friends Renato, Fagner, Guilherme, Prieslei, Thaisa, Glauber, Felipe, Mariana, Gabrielle, Juca, Zeni, Isma and Fabi with whom I constantly laugh and learn.

For technical and organizational support I would like to thank Petra Weiß, Patrizia Zündorf, Andreas Wißkirchen and Dagmar Faßbender from the Physikalisches Institut and BCTP.

Contents

1 Introduction

In the year 1973, the theoretical formulation of the Standard Model (SM) of particle physics was completed after the invention of the QCD Lagrangian [1]. Experimental confirmations and devised theoretical tools for the SM ingredients were several along the years, with the most important being:

⇒ Discovery of the electron in cathode rays (1897) [2]; first observation of the muon decay (1940) [3]; first indication of the tau lepton (1975) [4];

⇒ Confirmation of the detection of the electron antineutrino $\bar{\nu}_e$ in the process $\bar{\nu}_e + p \to e^+ + n$ (1959) [5]; first evidence of the muon neutrino ν_μ from $\pi^+ \to \mu^+ + (\nu/\bar{\nu})$ (1962) [6]; first evidence that the number of light neutrinos is 3 (1989) [7];

⇒ Introduction of local gauge invariance in Quantum Field Theory (1954) [8]; prediction of unavoidable massless bosons if a global symmetry of the Lagrangian is spontaneously broken (1961) [9]; invention of the gauge principle as basis to construct quantum theories of interacting fundamental fields (1961) [10]; introduction of the neutral intermediate weak boson Z (1961) [11]; example of a field theory with spontaneous symmetry breakdown with massive vector boson and without massless Goldstone bosons (1964) [12–14]; rigorous proof of renormalizability of the massless and massive Yang-Mills quantum field theory with spontaneously broken gauge invariance (1971) [15];

⇒ First evidence for parity nonconservation in weak decays (1957) [16]; CP violation due to the mixing of $B^0 - \bar{B}^0$ (1987) [17];

⇒ Evidence for the gluon jet (1979) [18–21]; evidence for the charged intermediate bosons $W^\pm$ (1983) [22, 23]; evidence for the neutral intermediate boson Z (1983) [24, 25];

⇒ Evidence for the quarks u, d and s following the "scaling" behaviour for deep-inelastic scattering — joint effort of the SLAC experiment (1969) [26], Bjorken (1969) [27] and Feynman (1969) [28]; evidence for the J/ψ $(c\bar{c})$ (1974) [29,30]; first evidence of Υ $(b\bar{b})$ (1977) [31]; observation of the top quark production (1995) [32];

⇒ Discovery of the Higgs boson by the CMS and ATLAS collaborations (2015) [33,34].

Although the SM theory is the most precise theory of nature[1] and explains all the experimental data referred to above, it cannot account either for the neutrino oscillations

[1] Its greatest achievement is to predict the electron anomalous magnetic moment g_e up to 10 orders of magnitude precision.

discovery [35, 36] or the dark matter (DM) evidences (discussed in depth next), besides other issues such as baryogenesis and the hierarchy problem.

In its original form, the SM Lagrangian cannot include masses for the active neutrinos (ν_L) consistent with local gauge invariance. A strategy most BSM (Beyond Standard Model) models use for the active neutrinos masses generation is to employ the seesaw mechanism by introducing the so-called sterile right-handed neutrinos, often denoted by N_R. By setting the masses of the latter very high, $\mathcal{O}(1\text{ TeV})$, the active neutrinos are given very tiny masses, consistent with solar and atmospheric mass splittings which require the active neutrinos masses to be $\mathcal{O}(10^{-2}\text{ eV})$.

Before turning to dark matter, another reserach topic that is beyond the Standard Model is the matter-antimatter asymmetry (or baryogenesis). The amount of asymmetry encoded within the SM cannot account for the one observed, if one considers matter and antimatter were once in equal amount. Mechanisms attempting to solve this question must yield an asymmetry $(n_B - n_{\bar{B}})/s_0 \sim 10^{-10}$, where s_0 is the entropy density of today and n_B ($n_{\bar{B}}$) the baryon (antibaryon) number density.

In the 1930s, Fritz Zwicky obtained first evidence for dark matter when mapping the radial velocities of galaxies in the Coma Cluster, approximately $3.2 \cdot 10^8$ light years away from Earth; it was observed that galaxies did not move with the velocity they were supposed to move if only visible matter would be present within the cluster. One can take this observation as a failure of the newtonian dynamics and study the possibility of a Modified Newtonian Dynamics (so-called MOND). On the other hand, one can face this discrepancy from observation as the existence of a new kind of particle. In this work, we consider a new kind of particle as the explanation for the evidences of this new physics, particle which we call the Dark Matter (DM) particle.

From the particle perspective, since Zwicky, apart from the knowledge that dark matter cannot be electrically charged or baryonic, its nature remains a mistery. The simplest assumption is that it interacts through gravity and weakly with known SM elementary particles. Up to now, only upper bounds on both its cross sections and thermally averaged cross sections (both studied into several different channels, such as lepton l^+l^- or quark $\bar{q}q$ pairs) have been obtained, therefore dark matter direct or indirect detection still remains to be investigated.

The simplest possibility to implement dark matter theoretically is to consider a new scalar field or a new fermion within the SM. It is required to not exhibit baryonic number or electric charge and must possess a very low cross section in accordance with the direct and indirect detection experiments. Among the implementations, The Higgs portal is a mainstream strategy, which considers the DM to interact with the Higgs mostly and therefore simplifies the study since the analysis depends mostly on the Higgs-DM interaction coupling; also because the interaction DM-[other SM particles] happens via propagator and/or loop diagrams and is consequently small.

The active neutrinos have already been regarded as dark matter: their masses are too small to provide the necessary amount of DM relic density. Additionally they cannot behave as DM since they are relativistic and it is known that most of the DM energy

density is composed of cold particles, i.e. non-relativistic matter. Sterile neutrinos have been considered in the literature and are not ruled out as fermionic DM candidates.

Undoubtedly, the most studied and prominent DM candidate is the neutralino, which stems from the MSSM (Minimal Supersymmetric Standard Model). It is the lightest supersymmetric particle within MSSM and originates from the linear combination of four symmetry eigenstates: the superpartners of the W_3, B, h_1 and h_2 bosons. The four types of neutralino are then the so-called Wino, Bino and the two Higgsinos with main components on the $\tilde{W}_3$, $\tilde{B}$, $\tilde{h}_1$ and $\tilde{h}_2$ fields, respectively. Non-supersymmetric models models deserve reference here as well: the 3-3-1 models, with a local symmetry $\mathrm{SU}(3)_C \otimes \mathrm{SU}(3)_L \otimes \mathrm{U}(1)_X$; the 2HDM (Two-Higgs-doublet model) model which contains an additional doublet compared to the SM; and the B-L model, with a local symmetry $\mathrm{SU}(3)_C \otimes \mathrm{SU}(2)_L \otimes \mathrm{U}(1)_{Y'} \otimes \mathrm{U}(1)_{B-L}$, among many others.

The standard treatment of dark matter is realized assuming a period in which all the particles in the universe were in thermal equilibrium. This way, one needs to solve the differential *Boltzmann* equation in order to obtain the DM energy of today. For non-relativistic particles, that amounts basically to their energy at the time a little after their decoupling from the interacting relativistic plasma. The thermal WIMP (Weakly Interacting Massive Particle) DM was suggested as a particle which interacts with a strength typical to the SM Weak interaction and its natural mass is around $\sim 10^{-1}$–1 TeV. Another candidate particle is the thermal SIMP (Strongly Interacting Massive Particle) DM, a particle which interacts with itself strongly, fact which yields interactions of the kind $3\,\mathrm{SIMPs} \to 2\,\mathrm{SIMPs}$ leading to self-heating; its natural mass is around ~ 100 MeV. These are examples of thermal DM.

Opposed to thermal relics, non-thermal relics are particles which are not generated by the usual freezout (decoupling from the relativistic plasma), but rather by the late decay of more massive particles, e.g. moduli fields or FIMPs (Feebly Interacting Massive Particles). The latter is a kind of particle which is used sometimes as the DM particle itself. Opposed to the standard freezout, the FIMPs may suffer *freezein*: one or more bath particles decay into the FIMP itself, thus yielding its energy and consequently its relic density.

This work deals theoretically with the question of DM production, both thermal and non-thermal, and is organized as follows. In chapter 2, we provide evidences for the existence of dark matter. In chapter 3, we cover the basics of general relativity to provide the background framework of this work, explaining the FLRW metrc and its implications as well as the Λ-CDM cosmological model. Still in this chapter, we provide the basics to obtain the relic density of a thermal species, along with an example of how the Boltzmann equation works. In chapter 4, dark matter direct and indirect detection frameworks are explained since they provide constraints on our dark matter candidates which will be dealt with in chapter 5. In the latter, we provide the reader a detailed view on two works which were completed in the thesis period and focus on the thermal DM, the first with emphasis on the calculation of the particles relativistic degrees of freedom near the QCD phase transition and the second focusing on dark matter relic density calculation

within a specific BSM model. In chapter 6 we talk about non-thermal sources of dark matter, including the basic framework and a specific study performed during the thesis period, where we explain its properties, including field content and its masses, decay rates, post-inflation dynamics, dark matter production as well as the achievement of vacuum uplifting. Finally, in the last chapter we draw our conclusions.

List of publications

Parts of this work have been published in scientific journals:

- M. Drees, F. Hajkarim, E. R. Schmitz. "The effects of QCD Equation of State on the Relic Density of WIMP Dark Matter". Journal of Cosmology and Astroparticle Physics **2015**(06):025 (2015).
- B. L. Sánchez-Vega, E. R. Schmitz. "Fermionic Dark Matter and Neutrino Masses in a B-L Model", Phys. Rev. D **92**, 053007 (2015).
- B. L. Sánchez-Vega, J. C. Montero, E. R. Schmitz. "New Constraints on the 3-3-1 Model with Right-Handed Neutrinos". The European Physical Journal C**78**:166 (2018).
- T. C. da Guio, E. R. Schmitz. "Dark matter in the KL moduli stabilizationscenario with SUSY breaking sector from $\mathcal{N} = 1$ SQCD". arXiv:1805.01521 [hep-ph] (*accepted to be published by Journal of High Energy Physics*).

2 Evidences

Within this chapter, we try to provide the reader an overview to the problem of dark matter, exposing the discrepancy between observations and theory expectations. We review below the most important evidences to the existence of dark matter[1].

- In 1933, Fritz Zwicky measured the mass of the Coma Cluster of galaxies outside of our local group [38]. The technique used by Zwicky was to measure the relative velocities of the galaxies in the cluster via Doppler shift; and use the virial theorem[2] to obtain the gravitational potential in which these galaxies were moving, and then get the mass distribution that would generate such a potential. He found for the mass of the cluster the value of about 400 times the mass that could be computed from the visible galaxies in the cluster. The observation was soon confirmed by similar measurements of the Virgo Cluster by Smith [39].

- Evidence for dark matter is also found by relating X-ray emission from clusters of galaxies to the distribution of the respective cluster masses [40]. Clusters form via a collapse of matter over the region of several megaparsecs (1 parsec = 3.26 light-years). They generate deep gravitational potential wells because of their high masses. This way, hydrogen gas from the galaxies leaks out and fills the whole volume of the cluster. These atoms, with large velocities[3], emit X-rays when they collide. Thus, in this manner, the X-ray luminosity probes the depth of the cluster gravitational potential. Therefore, one can estimate the mass that generates such a potential, providing the contradiction between the observed matter and the matter necessary to account for the measured X-ray luminosity.

- In the decade of 1970, astronomers started to measure sistematically the profiles of rotational velocity for several galaxies. If all the mass of the galaxy is made of stars that are visible, outside the region with visible matter the objects velocities behave as follows,

$$F_{\text{centripetal}} = F_{\text{gravitational}} \quad \therefore \quad v^2 = \frac{GM_{\text{gal}}}{r} \;\rightarrow\; v \propto \frac{1}{\sqrt{r}} \quad , \tag{2.0.1}$$

  where M_{gal} is the mass of the visible galaxy, and r is the distance of the test subject to the center of the galaxy; here we suppose that the galaxy is spherically symmetric.

[1] This section is based mostly on [37].

[2] The virial theorem states that the time average of the kinetic and potential of the considered system are related by $\langle K \rangle_t = -\frac{1}{2} \langle V \rangle_t$ (the minus sign for gravitational force) provided that the system remains bounded (spatially and also in terms of finite momentum values.)

[3] For a typical cluster mass of $\left(10^{14} - 10^{15}\right) M_{\odot}$, the gas reaches temperatures of several 10^7 K.

Something unexpected was observed: the velocities are almost constant or slightly increasing with distance [41]. Particularly, in the galaxy NGC 3067, Rubin et al. [42] showed that the rotational velocity profile maintains its large value at a distance of 40 Kpc from the center of the galaxy, even though the density of stars outside of 3 Kpc becomes very rare if compared to the halo of the galaxy.

Another way to measure the mass of a particular galaxy, other than rotation curves of its stars and X-ray emitting gas belonging to the galaxy, is to take positions and velocities of test particles such as globular clusters of stars or satellite galaxies, i.e. object not belonging to the chosen galaxy. By measurements of the velocities of globular clusters of the Milky Way, it was found that there is extra contribution to the mass of our galaxy up to distances of ~ 100 Kpc from its center [43]. The distance, from where stars of Milky way begin to become rare, to the center of the galaxy is approximately 15 Kpc (for reference, the solar system is at ~ 8.5 Kpc).

- Another sort of measurements concerning the existence of dark matter comes from the cosmic microwave background (CMB) [44, 45]. The CMB was emitted at the time of recombination, epoch when protons and electrons — particles that earlier were not bounded to each other because of high temperatures of the particle plasma which contained them — became bounded, forming Hydrogen; from this time on, the Universe became neutral for the photon (the photon cannot interact at as high a rate as before with proton and electron). Recombination ocurred when protons and neutrons were at the temperature of ~ 1 MeV. The most recent measurements of the PLANCK satellite require a medium in which a very weakly interacting species in nonrelativistic motion, usually called CDM (Cold Dark Matter), dominates. These measurements can be converted to the density ratios of baryonic and dark matter:

$$\Omega_{\text{baryon}}h^2 = 0.02226 \pm 0.00016 \ , \quad \Omega_{\text{CDM}}h^2 = 0.1193 \pm 0.0014 \quad , \tag{2.0.2}$$

  where $\Omega_i = \frac{\rho_i}{\rho_{\text{crit}}}$[4] and h is defined as $h \equiv H/\left(100 \text{ Km/s/Mpc}\right)$, where H is the current Hubble parameter value.

- Up to now, we referred to the name "dark matter". But that does not need to be the case. Instead, one could modify gravity [46] and then he would not have to introduce this new kind of matter. That approach had great phenomenological success at scales ranging from dwarf spheroidal galaxies to superclusters. However, the interpretation in terms of a new matter was encouraged by the observations in fig. 2.1, extracted from [47].

  The parameter κ is defined as the surface mass density. It is given by the integral of the energy density $\rho\left(\vec{r}\right)$ over the line of sight distance. Thus, it is related to the concentration of energy that bends the incoming source light.

[4] ρ_i is the i-species energy density, and $\rho_{\text{crit}} = 3H^2/8\pi G$ is the universe energy density that would make the universe be spatially flat.

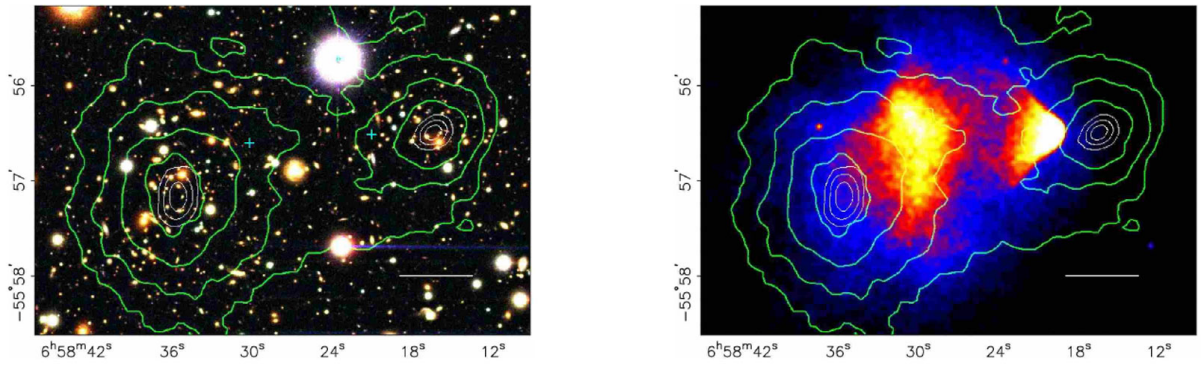

(a) (b)

Figure 2.1: In this figure are shown (a) a color image of the merging cluster 1E0657-558 and (b) a X-ray image of the same cluster. The white bar indicates 200 Kpc. The green contours in both images come from the reconstruction from the weak lensing method: the innermost contour has the highest κ and the outermost one the lowest κ. The white contours show the positions of the κ peaks and correspond to 68.3%, 95.5% and 99.7% confidence levels.

The actual existence of dark matter can be confirmed either by a laboratory detection or inferred by the discovery of a system in which the observed baryons and the hypothesized dark matter are spatially separated. The galaxy cluster 1E0657-558 is such a system.

During a merger of two clusters, galaxies behave as collisionless particles, while the fluid-like X-ray emitting plasmas (belonging to the respective galaxy concentrations) collide. Therefore, in this figure the two galaxy concentrations moved ahead of their plasma clouds which suffered ram pressure. In the absence of dark matter, the gravitational well depends only on the dominant visible component, i.e. the X-ray plasma. If, on the other hand, the total mass was dominated by collisionless dark matter, the potential would trace its distribution, which is expected to be spatially coincident with the collisionless galaxies. Hence, by extracting a map of the gravitational potential, one is able to infer that this phenomenon is probably caused by an unknown particle, usually called *dark matter*.

3 Thermal relics

In this chapter, we explain the tools and assumptions which underlie the calculations of relic abundance for particles which were in thermal equilibrium within the era of the radiation-dominated universe and eventually decoupled from it. We provide important concepts of General Relativity (GR), also thermodynamics and finally explain how the Boltzmann equation can provide information on the density of a generic species after they decoupled from the primordial thermal plasma. This discussion will also lay the foundations for the introdution of non-thermal relics in chapter 6.

3.1 Basic General Relativity

3.1.1 Introduction

The Standard Cosmological Model is based on the Einstein equation of gravity,

$$R^{ab} - \frac{1}{2}Rg^{ab} + \Lambda g^{ab} = 8\pi G T^{ab} \quad , \tag{3.1.1}$$

where g^{ab} is the metric tensor (which is found from Einstein equation). Locally in $3+1$ dimensions, by the Equivalence Principle, its components are reduced to the Minkowski metric ones, i.e. diag$(-1, 1, 1, 1)$,[1] which is the metric of Special Relativity. Λ is the cosmological constant which accounts for the accelerated expansion of the universe (it parametrizes the content of dark energy in the universe). G is the Newton's constant of gravitation, T^{ab} is the symmetric energy-momentum tensor of matter and radiation. The Ricci tensor R^{ab} and the Ricci scalar R are defined by

$$R^{ab} = R^{acb}{}_{c} \qquad \text{and} \qquad R = R^{a}{}_{a} \quad , \tag{3.1.2}$$

where $R_{abc}{}^{d}$ is the Riemann tensor,

$$R_{abc}{}^{d} = \partial_b \Gamma^{d}{}_{ac} - \partial_a \Gamma^{d}{}_{bc} + \left(\Gamma^{e}{}_{ac}\Gamma^{d}{}_{eb} - \Gamma^{e}{}_{bc}\Gamma^{d}{}_{ea}\right) \quad . \tag{3.1.3}$$

The Christoffel symbols $\Gamma^{c}{}_{ab}$ are given by (provided null torsion[2] and $\nabla_a g_{bc} = 0$)

$$\Gamma^{c}{}_{ab} = \frac{1}{2}g^{cd}\left(\partial_a g_{bd} + \partial_b g_{ad} - \partial_d g_{ab}\right) \quad . \tag{3.1.4}$$

[1] expressed in cartesian coordinates.

[2] $\nabla_a \nabla_b f = \nabla_b \nabla_a f$, where f is a function which takes from the manifold M to the reals $\mathbb{R}$; ∇_a is the covariant derivative which acts as $\nabla_a t^b = \partial_a t^b + \Gamma^{b}{}_{ac} t^c$ on a vector t^b, for example.

They determine the motion of free-falling bodies via the geodesic equation,

$$\frac{d^2x^\mu}{d\tau^2} + \Gamma^\mu{}_{\sigma\nu}\frac{dx^\sigma}{d\tau}\frac{dx^\nu}{d\tau} = 0 \quad . \tag{3.1.5}$$

An assumption of vital importance in general relativity is the *Equivalence Principle*, which is based on the equality of inertial and gravitational masses. It states that a free-falling observer does not experience any gravitational effect (dynamometers attached to his body would not register any force). This means that a free-falling observer can describe spacetime with a metric which is locally flat (Minkowski metric) and has a locally vanishing Christoffel symbol. One is able to verify that the geodesic equation then reduces to the special relativity equation of motion for an inertial body, i.e. $d^2x^\mu/d\tau^2 = 0$.

3.1.2 FLRW metric

Since observations of the universe have shown that it is spatially homogeneous and isotropic on large scales (100 Mpc), the Standard Cosmological Model assumes this is valid for a reference frame (this frame will be later defined). If one takes these considerations ahead, he is led to the following form of the interval,

$$ds^2 = -dt^2 + R^2(t)\left[\frac{dr^2}{1-kr^2} + r^2\left(d\theta^2 + \sin^2\theta d\phi^2\right)\right] \quad , \tag{3.1.6}$$

which is called Friedmann-Lemaitre-Robertson-Walker metric, for short FLRW metric. k specifies three different spatial sections of the universe:

- $k = 1$ means we have a 3-sphere, defined as the surface in 4-D flat Euclidean space $\mathbb{R}^4$ whose Cartesian coordinates satisfy

  $$x^2 + y^2 + z^2 + w^2 = R^2 \quad , \tag{3.1.7}$$

  where R can vary, depending on the 3-sphere. In spherical coordinates, the metric of the unit 3-sphere ($R = 1$) is

  $$ds^2 = d\psi^2 + \sin^2\psi\left(d\theta^2 + \sin^2\theta d\phi^2\right) \quad . \tag{3.1.8}$$

  If we change variables in the following way:

  $$d\psi \equiv \frac{1}{\sqrt{1-kr^2}} \ , \quad \text{with } k = 1 \quad , \tag{3.1.9}$$

  we obtain the interval of (3.1.6).

- $k = 0$ means we have a plane, defined in the 3-D flat Euclidean space $\mathbb{R}^3$. This plane is generated by not constraining the three coordinates, let us say x, y and z.

In cartesian and spherical coordinates, respectively, the metric of the plane is

$$ds^2 = dx^2 + dy^2 + dz^2 \quad , \tag{3.1.10}$$
$$ds^2 = d\psi^2 + \psi^2 \left(d\theta^2 + \sin^2\theta d\phi^2\right) \quad , \tag{3.1.11}$$

If one changes variables as in (3.1.9) (now with $k = 0$), he obtains (3.1.6).

- $k = -1$ means that the spatial section is a three-dimensional hyperboloid, defined as the surfaces in a 4-D Lorentz signature space whose cartesian coordinates satisfy

$$t^2 - x^2 - y^2 - z^2 = r^2 \quad , \tag{3.1.12}$$

where r can vary, depending on the 3-D hyperboloid.

In hyperbolic coordinates, the metric of the unit hyperboloid is

$$ds^2 = d\psi^2 + \sinh^2\psi \left(d\theta^2 + \sin^2\theta d\phi^2\right) \quad , \tag{3.1.13}$$

which turns into (3.1.6) if one changes variables according to (3.1.9), for $k = -1$.

All that is left to determine is the evolution with time of the function $R(t)$. For that, we have to introduce dynamics via Einstein's equation, which contains a quantity we did not define yet, that is the energy-momentum tensor T_{ab}. Some considerations are necessary. Just considering ordinary matter, we can say that at large scales each galaxy can be considered as a grain of dust. The *random* velocities of the galaxies are small, so the pressure of the dust galaxies is negligible. Thus, to an approximation the energy-momentum tensor of the universe is given by the one of dust (which is a perfect fluid, but its pressure is null)

$$T_{ab} = \rho u_a u_b \quad , \tag{3.1.14}$$

where ρ is the average matter density, and u_a is the four velocity of each galaxy. However, there are other energy contributions. Radiation has to be considered: we know that there exists radiation at a temperature of about 3 K filling the universe. That energy density can be described by a perfect fluid energy-momentum tensor, with nonzero pressure ($P_{\text{rad}} = \rho_{\text{rad}}/3$). Therefore, we take its energy-momentum tensor to be of the perfect fluid form

$$T_{ab} = \rho u_a u_b + P\left(g_{ab} + u_a u_b\right) \quad . \tag{3.1.15}$$

This tensor is the most general one respecting homogeneity and isotropy because it is formed by a combination of the only tensors which do not specify a privileged direction, i.e. tensors g_{ab} and u_a. Therefore, also the content of dark matter can be assumed to have that general form. Thus, assuming an energy-momentum tensor of a perfect fluid,

one can solve Einstein equation to obtain the so-called Friedmann equations

$$\frac{\ddot{R}}{R} = -\frac{4\pi G}{3}(\rho + 3p) + \frac{\Lambda}{3} \quad , \tag{3.1.16}$$

$$\left(\frac{\dot{R}}{R}\right)^2 = \frac{8\pi G}{3}\rho - \frac{k}{R^2} + \frac{\Lambda}{3} \quad . \tag{3.1.17}$$

For completeness, the cosmological constant Λ can be moved to the right side of (3.1.1) as a contribution to the energy-momentum tensor,

$$T^{\Lambda}_{ab} = -\frac{\Lambda}{8\pi G} g_{ab} \quad . \tag{3.1.18}$$

If we identify T^{Λ}_{ab} with the T_{ab} of a perfect fluid, we can obtain

$$P_\Lambda = -\frac{\Lambda}{8\pi G} \quad , \tag{3.1.19}$$

$$\rho_\Lambda = -P_\Lambda = \frac{\Lambda}{8\pi G} \quad . \tag{3.1.20}$$

Substituting the vacuum energy density into (3.1.16) and (3.1.17), it yields

$$\frac{\ddot{R}}{R} = -\frac{4\pi G}{3}(\rho - 2\rho_\Lambda + 3p) \quad , \tag{3.1.21}$$

$$\left(\frac{\dot{R}}{R}\right)^2 = \frac{8\pi G}{3}(\rho + \rho_\Lambda) - \frac{k}{R^2} \quad . \tag{3.1.22}$$

With them we can then find how $R(t)$ evolves in time, and consequently know how the geometry of the isotropic and homogeneous universe evolves.

3.2 Λ-CDM Cosmological Model

The model on which this work will be based is the Λ-CDM Cosmological Model. It assumes that general relativity, with cosmological constant Λ, is the correct theory of gravity on cosmological scales, using the FLRW metric. Then, into this framework, one can introduce a field to describe dark matter (if one deals with the dark matter particle description), besides the fields that describe the usual matter, which is basically the Standard Model of particles. This is in short the Λ-CDM model.

It manages to match with well stablished observational tests, for example:

- the accelerating expansion of the universe observed in the light from distant type Ia Supernovae (SNe Ia) [48, 49];
- the structure of the cosmic microwave background [50];
- the large-scale structure in the distribution of galaxies [51];

- the baryon acoustic oscillations, which have possibly been formed in the initial plasma via perturbations and have been carried through the epoch of recombination [52];
- the measurements of dark energy parameters through weak lensing [53];

But there are still some challenges the model faces [54], among which is the most important one:

- the *too big to fail* problem. Simulations for the substructure of the Milky Way and Acquarius halos imply ~ 10 subhalos, that are so massive and so dense that they would be too big to fail to form lots of stars. The problem lies on the observation that none of the satellite galaxies of the Milky Way or Andromeda have stars moving as fast as expected in these dense subhalos [55, 56].

There are modifications to the Λ-CDM model and some of which can be found in [57]. However, we assume Λ-CDM throughout this work.

3.3 Thermodynamics of the early Universe

In order to study the early universe, we have to define the following quantities:

$$n_\chi = \frac{\boldsymbol{g}_\chi}{(2\pi)^3}\int f_\chi(\vec{p})\, d^3p \quad , \tag{3.3.1}$$

$$\rho_\chi = \frac{\boldsymbol{g}_\chi}{(2\pi)^3}\int E_\chi(\vec{p})\, f_\chi(\vec{p})\, d^3p \quad , \tag{3.3.2}$$

$$p_\chi = \frac{\boldsymbol{g}_\chi}{(2\pi)^3}\int \frac{|\vec{p}|^2}{3E_\chi(\vec{p})} f_\chi(\vec{p})\, d^3p \quad , \tag{3.3.3}$$

where n_χ, ρ_χ and p_χ denote respectively number of the particle species χ per volume, energy of the particle species χ per volume and pressure associated to the particle species χ. $\boldsymbol{g}_\chi$ is the number of internal degrees of freedom (spin) and $E_\chi(\vec{p}) = \sqrt{|\vec{p}|^2 + m_\chi^2}$ is the energy of the particle. The statistical equilibrium distribution $f_\chi(\vec{p})$ depends on the energy E_χ, the chemical potential μ_χ, and the temperature T_χ, and is given by

$$f_\chi(\vec{p}) = \frac{1}{e^{(E_\chi - \mu_\chi)/T_\chi} \pm 1} \quad , \tag{3.3.4}$$

where the plus sign applies to fermions and the minus sign to bosons. We might as well provide the relativistic and the nonrelativistic limits of (3.3.4).

Nonrelativistic limit. For $m_\chi \gg T_\chi$ and $m_\chi \gg \mu_\chi$, we have both bosons and fermions

$$f_\chi(\vec{p}) \simeq e^{-m_\chi/T_\chi} e^{-|\vec{p}|^2/2m_\chi T_\chi} \quad , \tag{3.3.5}$$

which leads to

$$n_\chi \simeq \boldsymbol{g}_\chi \left(\frac{m_\chi T_\chi}{2\pi}\right)^{3/2} e^{-m_\chi/T_\chi} \quad , \tag{3.3.6}$$

$$\rho_\chi \simeq m_\chi n_\chi \left(1 + \frac{3}{2}\frac{T_\chi}{m_\chi}\right) \quad , \tag{3.3.7}$$

$$p_\chi \simeq n_\chi T_\chi \ll \rho_\chi \quad . \tag{3.3.8}$$

Relativistic limit. For $T_\chi \gg m_\chi$ and $T_\chi \gg \mu_\chi$, we have

$$f_\chi(\vec{p}) \simeq \frac{1}{e^{|\vec{p}|/T_\chi} \pm 1} \quad , \tag{3.3.9}$$

which leads to

$$n_\chi(\text{boson}) \simeq \frac{\zeta(3)}{\pi^2}\boldsymbol{g}_\chi T_\chi^3 \quad , \tag{3.3.10}$$

$$n_\chi(\text{fermion}) \simeq \frac{3}{4}\frac{\zeta(3)}{\pi^2}\boldsymbol{g}_\chi T_\chi^3 \quad , \tag{3.3.11}$$

$$\rho_\chi(\text{boson}) \simeq \frac{\pi^2}{30}\boldsymbol{g}_\chi T_\chi^4 \quad , \tag{3.3.12}$$

$$\rho_\chi(\text{fermion}) \simeq \frac{7}{8}\frac{\pi^2}{30}\boldsymbol{g}_\chi T_\chi^4 \quad , \tag{3.3.13}$$

$$p_\chi \simeq \frac{\rho_\chi}{3} \quad , \tag{3.3.14}$$

where $\zeta(3) \simeq 1.20206$ is the Riemann zeta evaluated at 3.

Now we define the total energy density (including both relativistic and nonrelativistic kinds) by

$$\rho = \sum_\chi \rho_\chi = \frac{\pi^2}{30}\left(\sum_\chi \rho_\chi \frac{30}{\pi^2}\frac{1}{T_\gamma^4}\right) T_\gamma^4 \equiv \frac{\pi^2}{30} g T_\gamma^4 \quad , \tag{3.3.15}$$

where we defined

$$g \equiv \sum_\chi g^{(\chi)} \quad , \tag{3.3.16}$$

$$g^{(\chi)} \equiv \rho_\chi \frac{30}{\pi^2}\frac{1}{T_\gamma^4} \quad . \tag{3.3.17}$$

We can express $g^{(\chi)}$ as

$$g^{(\chi)} = \boldsymbol{g}_\chi \frac{15}{\pi^4}\left(\frac{T_\chi}{T_\gamma}\right)^4 \int_{x_\chi}^{\infty} dz \frac{z^2\sqrt{z^2 - x_\chi^2}}{e^{z-\xi_\chi} \pm 1} \quad , \tag{3.3.18}$$

with $x_\chi \equiv m_\chi/T_\chi$ and $\xi_\chi \equiv \mu_\chi/T_\chi$. The plus sign for fermions, the minus sign for bosons. Note that if the particle is relativistic, its $g^{(\chi)}$ value can be evaluated from (3.3.12) and

(3.3.13), which yield

$$g^{(\chi)}\,(\text{boson}) \;=\; \boldsymbol{g}_\chi \left(\frac{T_\chi}{T_\gamma}\right)^4 \quad , \tag{3.3.19}$$

$$g^{(\chi)}\,(\text{fermion}) \;=\; \frac{7}{8}\,\boldsymbol{g}_\chi \left(\frac{T_\chi}{T_\gamma}\right)^4 \quad . \tag{3.3.20}$$

The contribution from nonrelativistic particles is negligible compared to the relativistic ones, as can be seen from the limits of the integral in (3.3.18). We can then approximately obtain

$$g \simeq \sum_{\chi=\text{relativistic bosons}} \boldsymbol{g}_\chi \left(\frac{T_\chi}{T_\gamma}\right)^4 + \sum_{\chi=\text{relativistic fermions}} \frac{7}{8}\,\boldsymbol{g}_\chi \left(\frac{T_\chi}{T_\gamma}\right)^4 \quad . \tag{3.3.21}$$

To first approximation, the value of g changes when the temperature drops below the mass of a particle in the interacting plasma (i.e. the particle is no longer relativistic). Then, this particle does not contribute to the sum (3.3.21) anymore. The exact transition between the two values of g must be calculated numerically using the expression (3.3.18).

For a clearer understanding of the contribution of a particle to g, we consider three different temperature regimes for the SM:

- For $m_e \simeq 0.5$ MeV $\ll T_\gamma \ll 105$ MeV $\simeq m_\mu$, the relativistic particles within the plasma are the photons γ, electrons e^-, positrons e^+ and neutrinos ν_i (which we will consider to be Majorana and therefore are their own antiparticles), all with the same temperature, yielding

$$g \simeq 2 + 2\frac{7}{8}2 + 3\frac{7}{8}2 = \frac{43}{4} = 10.75 \quad . \tag{3.3.22}$$

- For $m_\mu \simeq 105$ MeV $\ll T_\gamma \ll 300$ MeV $\sim T_c$[3], there are also muons μ^- and anti-muons μ^+ (which give the same contribution as e^- and e^+, yielding 7/2), thus leading to

$$g \simeq \frac{57}{4} = 14.25 \quad . \tag{3.3.23}$$

- For $T_\gamma \gg 300$ MeV, there are tau τ^- and anti-tau τ^+ (contributing 7/2 for $T_\gamma > m_\tau \simeq 1800$ MeV); u and $\bar{u}$, d and $\bar{d}$, s and $\bar{s}$ quarks (contributing 63/2 for $T_\gamma \gg (m_u, m_d, m_s) \sim (1 - 100)$ MeV); c and $\bar{c}$ quarks (21/2 for $T_\gamma \gg m_c \simeq 1200$ MeV); b and $\bar{b}$ quarks (21/2 for $T_\gamma \gg m_b \simeq 4.2$ GeV); t and $\bar{t}$ quarks (21/2 for $T_\gamma \gg m_t \simeq 170$ GeV); eight gluons g^a (yielding 16); $W^\pm$ and Z (9 for $T_\gamma \gg m_Z \simeq 90$ GeV); H (1 for $T_\gamma \gg m_H \simeq 125$ GeV) for a total

$$g \simeq \frac{427}{4} = 106.75 \quad . \tag{3.3.24}$$

[3] T_c is roughly the QCD transition temperature, around which the crossover between partons (gluons and quarks) and hadrons (pions, protons, ...) happens. It will be defined and discussed in detail at the subsection 5.1.1.

Two comments are in order:

(i) For $T_\gamma < m_e \simeq 0.5$ MeV, neutrinos are already decoupled ($T_{\rm dec} \sim 1$ MeV) and they are at different temperatures than the plasma. These temperatures T_{ν_i} can be calculated [58], but we will not do this step here;

(ii) The first and second regimes are not realistic since it is not possible to have at the same time $T_\gamma \ll 105$ MeV and $T_\gamma \gg 0.5$ MeV (or even worse $T_\gamma \ll 300$ MeV and $T_\gamma \gg 105$ MeV), but are shown for enlightenment of the reader. An exact calculation should be performed via (3.3.18), accounting for the mixture of relativistic and nonrelativistic behaviour.

We plot in fig. 3.1 a numerical evaluation of g as a function of the temperature of the plasma T_γ, using (3.3.18), summing over all pertinent particles of the SM within the different temperature regimes. The calculation is considered within a temperature region quite above the QCD transition temperature $T_c \sim 300$ MeV.

At this point, we turn to another important quantity, the entropy density, which is used within the Boltzmann equation (we talk about the latter in sec. 3.4). To derive it, we first use the second law of thermodynamics, which states

$$đQ = dU + đW \quad , \tag{3.3.25}$$

where the heat differential $đQ$ is given by $đQ = TdS$, where $S = S(T, V, N)$ is a function of state of the system called entropy, U is the system internal energy and W stands for work, the energy added to or taken from the system. From (3.3.25), we have

$$\begin{aligned} TdS(T,V,N) &= d[\rho(T)V] + p(T)\,dV + \mu(T)\,dN \\ &= V\frac{d\rho}{dT}dT + [\rho(T) + p(T)]\,dV + \mu(T)\,dN \quad . \end{aligned} \tag{3.3.26}$$

Notice that the functions μ, p and ρ depend on the temperature T only. First, $\mu = \mu(T)$ cannot depend either on the volume or the number of particles because the observable which determines whether an hypothetical process $\phi_1 + \phi_2 \leftrightarrow \phi_3 + \phi_4$ will happen is the cross section, which depends ultimately on $s = (p_1 + p_2)^2$; s is related to T since the latter is what provides the necessary kinetic energy for that process to occur. Thus, when T becomes sufficiently small, the process considered is not likely to happen anymore because of the consequent s drop. In the end, the ϕ_i in our example is forced to decouple from the surrounding particles.

Now for the case of $\rho = \rho(T)$ and $p = p(T)$, it is clear from (3.3.6), (3.3.7), (3.3.8), (3.3.12), (3.3.13), (3.3.14) that they can only depend on m_χ, μ_χ and T_χ. m_χ enters as an input parameter, therefore in the end we have the functions μ, ρ and p depending only on T. Hence,

$$\frac{\partial S(T,V,N)}{\partial T} = \frac{V}{T}\frac{d\rho(T)}{dT}\,, \quad \frac{\partial S(T,V,N)}{\partial V} = \frac{\rho(T) + p(T)}{T}\,, \quad \frac{\partial S(T,V,N)}{\partial N} = \frac{\mu(T)}{T}\,.$$

On $S(T,V,N)$ is imposed the condition

$$\frac{\partial^2 S(T,V,N)}{\partial V \partial T} = \frac{\partial^2 S(T,V,N)}{\partial T \partial V} \quad , \tag{3.3.27}$$

which implies

$$\frac{dp(T)}{dT} = \frac{\rho(T) + p(T)}{T} \quad . \tag{3.3.28}$$

Also, we can find from

$$\frac{\partial^2 S(T,V,N)}{\partial N \partial T} = \frac{\partial^2 S(T,V,N)}{\partial T \partial N} \tag{3.3.29}$$

the expression

$$\frac{d\mu(T)}{dT} = \frac{\mu(T)}{T} \quad . \tag{3.3.30}$$

Putting (3.3.28) and (3.3.30) into (3.3.26), we obtain

$$\begin{aligned} TdS(T,V,N) &= d[\rho(T)V] + p(T)V + \left[V\frac{dp(T)}{dT}dT - V\frac{dp(T)}{dT}dT\right] \\ &\quad + \mu(T)dN + \left[N\frac{d\mu(T)}{dT}dT - N\frac{d\mu(T)}{dT}dT\right] \\ dS(T,V,N) &= d\left[\frac{p+\rho+\mu\frac{N}{V}}{T}V\right] \equiv d\left[\frac{p+\rho+\mu n}{T}V\right] \quad . \end{aligned} \tag{3.3.31}$$

Therefore, apart from an additive constant, the entropy $S(T,V,N)$ and the entropy density $s(T,n)$ are given by

$$S(T,V,N) = \frac{p+\rho+\mu n}{T}V \ , \quad s(T,n) \equiv \frac{S(T,V,N)}{V} = \frac{p+\rho+\mu n}{T} \quad . \tag{3.3.32}$$

We will neglect the chemical potential μ for the following reasons:

- In thermodynamic equilibrium, the chemical potential for neutral particles is null. In fact, if one considers the following reversible processes: $\phi_0 + \phi_0 \rightleftharpoons \phi_+ + \phi_-$ and $\phi_0 + \phi_0 + \phi_0 \rightleftharpoons \phi_+ + \phi_-$, which are allowed by charge conservation, they yield $2\mu_0 = \mu_+ + \mu_-$ and $3\mu_0 = \mu_+ + \mu_-$. They imply that $\mu_0 = 0$;
- For charged particles, as indicated in the frist item, we obtain $\mu_+ = -\mu_-$. Also, considering thermal equilibrium, particle and antiparticle have roughly the same number densities, $n_+ \simeq n_-$, therefore the term $\frac{1}{T}(\mu_+ n_+ + \mu_- n_-)$ in the entropy density definition yields $\frac{\mu_+}{T}(n_+ - n_-) \simeq 0$.

In the end, we just have to calculate

$$s = \frac{\rho + p}{T} \quad . \tag{3.3.33}$$

As we did for the total energy density ρ (3.3.15), we can do the following definition for

the total entropy density (all species being fed by the temperature T_γ):

$$s = \sum_{\chi=\text{interacting}} s_\chi = \frac{2\pi^2}{45} h T_\gamma^3 \quad . \tag{3.3.34}$$

The sum over interacting particles means we consider all the particles which contribute to the entropy of the plasma when interacting in thermal equilibrium. We defined

$$h \equiv \sum_\chi h^{(\chi)} \quad , \tag{3.3.35}$$

$$h^{(\chi)} \equiv s_\chi \frac{45}{2\pi^2} \frac{1}{T_\gamma^3} \quad . \tag{3.3.36}$$

We can express $h^{(\chi)}$ as

$$h^{(\chi)} = \boldsymbol{g}_\chi \frac{15}{4\pi^4} \int_{x_\chi}^{\infty} dz \frac{\left(4z^2 - x_\chi^2\right)\sqrt{z^2 - x_\chi^2}}{e^{z-\xi_\chi} \pm 1} \quad , \tag{3.3.37}$$

where $x_\chi \equiv m_\chi / T_\gamma$ and $\xi_\chi \equiv \mu_\chi / T_\gamma$. The plus sign for fermions and minus sign for bosons. We can see from the last equation that relativistic particles contribute much more than nonrelativistic ones to the total entropy density due to $x_\chi \gg 1$ for the latter. Note also that if the particle is relativistic, its $h^{(\chi)}$ value can be evaluated from (3.3.12), (3.3.13), (3.3.14) and (3.3.33). Therefore, we can write

$$h = \sum_{\chi=\text{int. rel. bosons}} \boldsymbol{g}_\chi \quad + \sum_{\chi=\text{int. rel. fermions}} \frac{7}{8} \boldsymbol{g}_\chi \quad . \tag{3.3.38}$$

The value of h changes when the temperature drops below the mass of a particle in the plasma, as we observed for the function g. Then, this particle will not contribute to (3.3.38) anymore. The exact transition between the two stages should be calculated numerically using the expression (3.3.37) for the particle that becomes relativistic.

We avoid examplifying here, since when $T_\chi = T_\gamma$, h and g turn out to be identical. In fig. 3.1, we compare h and g above T_c.

The difference between the two curves lies on the following feature: the two functions would be equal if every particle was in equilibrium all the time ($T_\chi = T_\gamma$), which is visible in the figure for $T_\gamma \gtrsim 500$ GeV. However, when particles decouple from thermal equilibrium, they no longer share the same temperature as before the decoupling. g can still be calculated through (3.3.15) if we know T_χ of all decoupled particles, as well as h through (3.3.34), however their dependence on the temperature ratio $r \equiv (T_\chi / T_\gamma)$ is different, $\propto r^4$ for ther former and $\propto r^3$ for the latter; also one must note the term $\left(4z^2 - x_\chi^2\right)$ inside $h^{(\chi)}$ expression, as opposed to $(4z^2)$ within the $g^{(\chi)}$ definition. The difference between these terms is noticeably more important than the r^n discrepancy for the region considered in the figure, i.e. for 1 GeV $\leq T_\gamma \leq$ 1000 GeV. For the region $T \sim 0.1$ MeV, one can note

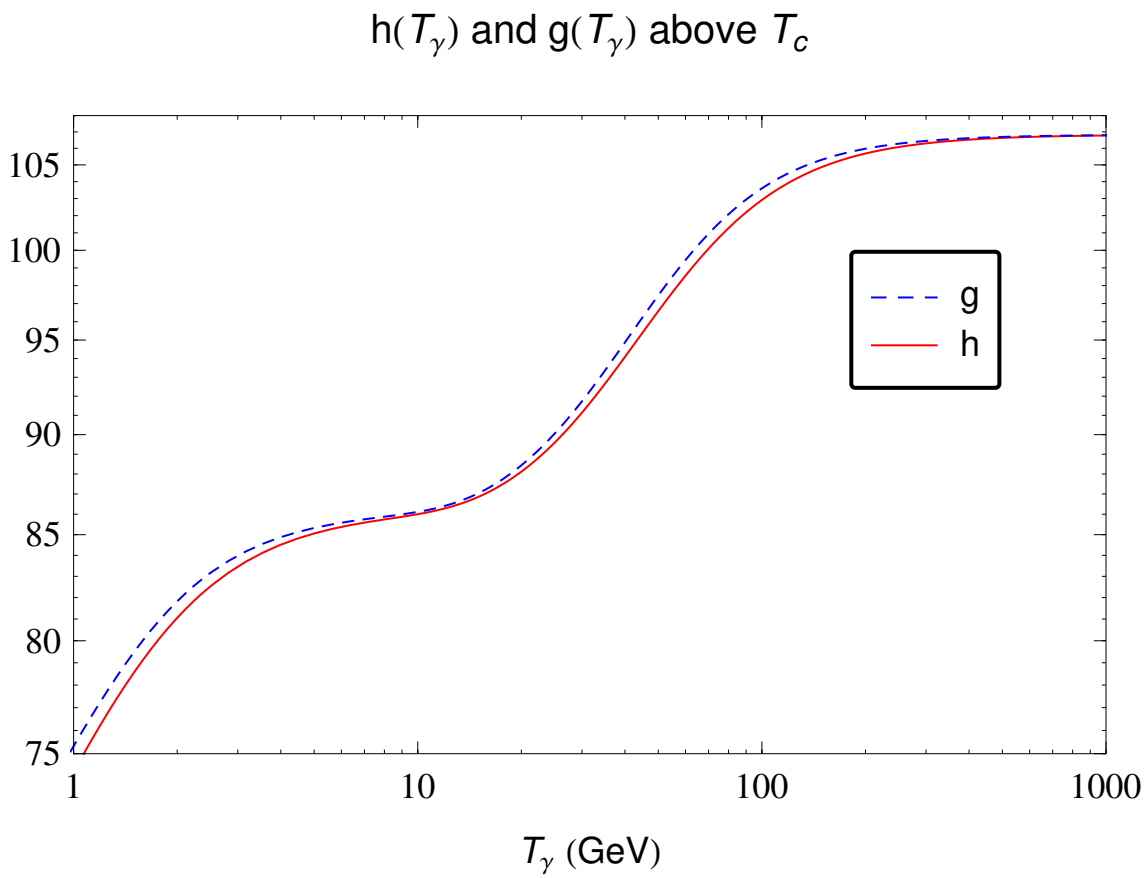

Figure 3.1: Plot of h and g as a function of the plasma temperature T_γ. We do not show the fine behaviour of the QCD deconfinement transition ($T \sim 0.3$ GeV), leaving this range to section 5.1, where it will be discussed more precisely.

that the r^n dependece is more prominent for the behaviour of g and h, as we will see sec. 5.1, where a wider temperature region is considered.

3.4 The Boltzmann equation

In this section, we are going to provide the tools to the calculation of thermal relic densities, i.e. the densities of particles which decoupled from the plasma. This task can be achieved through the Boltzmann equation. Since we will not go through the explicit derivation of the latter, we refer the reader to [59–61]. We will though provide the reader with an intuitive insight of the equation through an example an related observations.

Firstly, let us write the Boltzmann equation for a particle species χ interacting through the process $\chi + \chi \rightleftharpoons$ [any allowed species],

$$\dot{n}_\chi + 3Hn_\chi = -\langle \sigma v_{\text{Møl}} \rangle \left(n_\chi^2 - n_{\chi,\text{eq}}^2 \right) \quad , \tag{3.4.1}$$

where $\langle \sigma v_{\text{Møl}} \rangle$ is the thermally averaged annihilation cross section of the considered particle, $v_{\text{Møl}}$ is the Møller velocity involving the initial particles, H is the Hubble parameter, n_χ is the number density of the species χ, and $n_{\chi,\text{eq}}$ is the thermal equilibrium number

density of χ. The definition of $\langle \sigma v_{\text{Møl}} \rangle$ is

$$\langle \sigma v_{\text{Møl}} \rangle = \frac{\int\int \sigma v_{\text{Møl}} dn_\chi^{\text{eq}} dn_\chi^{\text{eq}}}{\int\int dn_\chi^{\text{eq}} dn_\chi^{\text{eq}}} = \frac{1}{8m^4 T \left[K_2\left(\frac{m}{T}\right)\right]^2} \int_{4m^2}^{\infty} \sigma\left(s - 4m^2\right) \sqrt{s} K_1\left(\frac{\sqrt{s}}{T}\right) \quad , \tag{3.4.2}$$

where $dn_\chi^{\text{eq}} = \boldsymbol{g}_\chi f_\chi\left(\vec{p}\right) \frac{d^3p}{(2\pi)^3}$ as defined in eq. (3.3.1), and $v_{\text{Møl}} = \left(|\vec{v}_1 - \vec{v}_2|^2 - |\vec{v}_1 \times \vec{v}_2|^2\right)^{1/2} = \frac{\left((p_1 \cdot p_2)^2 - m_1^2 m_2^2\right)^{1/2}}{E_1 E_2}$, where 1 and 2 are the initial colliding particles.

Let us describe every term in the eq. (3.4.1):

- The first term is simply the rate at which n_χ evolves with time;
- The second one accounts for the expansion of the universe. This term states that $\dot{n}_\chi < 0$ as the universe dillates, which is the effect one would expect since a number density n_i is inversely proportional to the considered volume, and as the volume turns bigger, n_i gets smaller;
- The third term accounts for the interaction of χ with the surrounding environment, and also has the effect of decreasing n_χ. $\langle \sigma v_{\text{Møl}} \rangle$ takes into its definition the cross section of the processes $\chi + \chi \to$ [any allowed particles], thus its interpretation as an interaction term; additionally, the squared $n_\chi^2 = n_\chi n_\chi$ means that the initial particles are 2 χ particles.

  When $n_\chi = n_{\chi,\text{eq}}$ — i.e. the particle χ is still in thermal equilibrium — the third term vanishes, which means that there is no preferred direction of the allowed processes, $\chi + \chi \rightleftharpoons$ [any allowed particles]. When the temperature of the plasma drops sufficiently so that $\langle \sigma v_{\text{Møl}} \rangle$ is not efficient enough to maintain the particle χ at thermal equilibrium, the particle χ is said to freeze out (or decouple). After its decoupling, the particle density evolves following the Hubble parameter.

We must comment that the form of the third term $\langle \sigma v_{\text{Møl}} \rangle \left(n_\chi^2 - n_{\chi,\text{eq}}^2\right)$ only applies to the case where two χ particles are in the initial state. For example, if the process $\chi + \chi \rightleftharpoons \chi +$ [any allowed particle] turns dominant, the Boltzmann equation third term becomes $\langle \sigma v_{\text{Møl}} \rangle \left(n_\chi^2 - n_\chi n_{\chi,\text{eq}}\right)$ and a different behaviour is to be expected: χ takes longer to decouple from the plasma, since its depletion is not as fast as the case $\chi + \chi \rightleftharpoons$ [any allowed particles]. We will nevertheless not consider such cases and refer to eq. 3.4.1 as the Boltzmann differential equation for n_χ.

For later use and convenience, we will define $\langle \sigma v \rangle \equiv \langle \sigma v_{\text{Møl}} \rangle$.

3.4.1 Rewriting the Boltzmann equation

It is convenient to replace time in the eq. (3.4.1) by the plasma temperature. For this task, we need our previous definitions for h and g:

$$h\left(T_\gamma\right) = \frac{45}{2\pi^2}\frac{s\left(T_\gamma\right)}{T_\gamma^3} \quad , \tag{3.4.3}$$

$$g\left(T_\gamma\right) = \frac{30}{\pi^2}\frac{\rho\left(T_\gamma\right)}{T_\gamma^4} \quad , \tag{3.4.4}$$

where $s\left(T_\gamma\right)$ and $\rho\left(T_\gamma\right)$ are respectively the total entropy and energy densities of the plasma of interacting particles, and T_γ is the plasma temperature. Now we define the variable $Y \equiv n_\chi/s$. Its time derivative reads:

$$\frac{dY}{dt} = \frac{1}{s}\frac{dn_\chi}{dt} - \frac{n_\chi}{s^2}\frac{ds}{dt} \quad , \tag{3.4.5}$$

$$\frac{ds}{dt} = \frac{d}{dt}\left(\frac{S}{R^3}\right) = -\frac{3S}{R^4}\dot{R} = -3sH \quad , \tag{3.4.6}$$

$$s\frac{dY}{dt} = \dot{n}_\chi + 3Hn_\chi \quad , \tag{3.4.7}$$

where we have used the condition of entropy conservation $\frac{dS}{dt} = 0$ (when no external energy is introduced).

Thus, the Boltzmann equation gets the form

$$\frac{dY}{dt} = -s\left\langle\sigma v\right\rangle\left(Y^2 - Y_{\rm eq}^2\right) \quad . \tag{3.4.8}$$

We now use the chain derivative rule to obtain the derivative of Y with respect to $x \equiv m_\chi/T_\gamma$: $dY/dt = dY/dx \cdot dx/dt$. Similarly, from eq. (3.4.6) we obtain

$$s = -\frac{1}{3H}\frac{ds}{dt} = -\frac{1}{3H}\frac{ds}{dx}\frac{dx}{dt} \quad . \tag{3.4.9}$$

At this point, we have

$$\frac{dY}{dx} = \frac{1}{3H}\frac{ds}{dx}\left\langle\sigma v\right\rangle\left(Y^2 - Y_{\rm eq}^2\right) \quad . \tag{3.4.10}$$

ds/dx can be expressed, following eq. (3.4.3), as

$$\frac{ds}{dx} = \frac{2\pi^2}{45}\left(\frac{dh}{dT_\gamma}T_\gamma^3 + 3hT_\gamma^2\right)\frac{dT_\gamma}{dx} \quad . \tag{3.4.11}$$

Within the FRLW cosmology with no curvature ($k = 0$), the Hubble constant can be written via one of the Friedmann equations,

$$H = \left(\frac{8}{3}\pi G\rho\right)^{1/2} \quad , \tag{3.4.12}$$

where ρ can be substituted by eq. (3.4.4), which yields

$$H = \left(\frac{4}{45}\pi^3 G g\right)^{1/2} T_\gamma^2 \quad , \tag{3.4.13}$$

Therefore,

$$\frac{1}{3H}\frac{ds}{dx} = \frac{\frac{2\pi^2}{45}\left(\frac{1}{3}\frac{dh}{dT_\gamma}T_\gamma + h\right)\frac{dT_\gamma}{dx}}{\left(\frac{4}{45}\pi^3 G g\right)^{1/2}} \quad . \tag{3.4.14}$$

In the end, the Boltzmann equation can be written as [59, 60]

$$\frac{dY}{dx} = -\frac{m_\chi}{x^2}\frac{\left(\frac{1}{3}\frac{dh}{dT_\gamma}T_\gamma + h\right)}{\left(\frac{45}{\pi}Gg\right)^{1/2}}\langle\sigma v\rangle\left(Y^2 - Y_{\rm eq}^2\right) \quad , \tag{3.4.15}$$

where we used $\frac{dT_\gamma}{dx} = -\frac{m_\chi}{x^2}$. For later use, we define the function

$$g_*^{1/2} = \frac{h}{g^{1/2}}\left[1 + \frac{1}{3}\frac{d\left(\ln h\right)}{d\left(\ln T_\gamma\right)}\right] \quad , \tag{3.4.16}$$

which yields eq. (3.4.15) as

$$\frac{dY}{dx} = \sqrt{\frac{\pi}{45G}} m_\chi g_*^{1/2}\langle\sigma v\rangle\frac{1}{x^2}\left(Y_{\rm eq}^2 - Y^2\right) \quad . \tag{3.4.17}$$

In the next subsection, we solve the last equation for a simple interaction.

Lastly we address the expression of the relic density. For WIMPs (weakly interacting massive particles), numerically solving eq. (3.4.17) from an initial point $x_i \lesssim 10$ is enough, yielding a final result independent of the initial value $Y\left(x_i\right)$. From x_i, one needs to numerically track the behaviour of $Y\left(x\right)$ up to x_0 (today), however for computational and accuracy reasons, $x_0 \simeq 1000$ is sufficient[4]. The present scaled relic density Ω_χ times the squared scaled Hubble parameter h can then be computed from

$$\Omega_\chi h^2 = \frac{\rho_\chi}{\rho_{\rm crit}}h^2 \quad , \tag{3.4.18}$$

$$= \frac{m_\chi Y_0 s_0}{3H_0^2/8\pi G}\left(\frac{H_0}{100\,{\rm km\,s^{-1}\,Mpc^{-1}}}\right)^2 \quad , \tag{3.4.19}$$

where $Y_0 = Y\left(x = 1000\right)$ and $s_0 = 2891.2\,{\rm cm}^{-3}$ (today's entropy density); and we substituted $\rho_{\rm crit} = 3H_0^2/8\pi G$ (today's critical energy density). Note that H_0 cancels on the right hand side, yielding in the end (after adding the values of G and s_0)

$$\Omega_\chi h^2 = 2.7889\cdot 10^8 Y_0\frac{m_\chi}{(1\,{\rm GeV})} \quad . \tag{3.4.20}$$

[4] If one takes into account the precision achieved by PLANCK observations, $\Omega h^2 = 0.1193 \pm 0.0014$, it is only necessary to obtain five orders of magnitude precision on the numerical solution of $Y\left(x_0\right)$.

Do not confuse here the symbol h for the scaled Hubble parameter and the function of entropy degrees of freedom.

3.4.2 An example: How the Boltzmann equation works

For sake of clarity, we now perform an example of numerical computation regarding the decoupling of a species from the plasma. For this task, we assume an effective interaction Lagrangian (for this species) of the kind

$$\mathcal{L}_{\text{eff}} = \frac{\lambda}{4}\chi^2\phi^2 \quad , \tag{3.4.21}$$

where χ is a real scalar field representing the pertinent particle, and ϕ is some SM real scalar field.

First, we need to find an expression for the cross section of the process $\chi+\chi \to \phi+\phi$. Up to tree-level Feynman diagrams, we have just a vertex diagram, which yields an amplitude

$$i\mathcal{M} = -i\lambda \quad , \tag{3.4.22}$$

For the cross section

$$\left(\frac{d\sigma}{d\Omega}\right)_{\text{CM}} = \frac{|\mathcal{M}|^2}{64\pi^2 s}\frac{\xi_{34}}{\xi_{12}} \quad , \tag{3.4.23}$$

where $\xi_{ij} = \left(s-(m_i+m_j)^2\right)^{1/2}\left(s-(m_i-m_j)^2\right)^{1/2}$, we obtain

$$\sigma_{\chi\phi} = \frac{|\lambda|^2}{16\pi s}\left(\frac{s-4m_\phi^2}{s-4m_\chi^2}\right)^{1/2} \quad . \tag{3.4.24}$$

Next, we calculate $\langle\sigma v\rangle$, considering $m_\phi = 0$ for simplicity, which yields

$$\langle\sigma v\rangle = \frac{|\lambda|^2}{32\pi m_\chi^2}\left[\frac{K_1\left(\frac{m_\chi}{T}\right)}{K_2\left(\frac{m_\chi}{T}\right)}\right]^2 \quad , \tag{3.4.25}$$

where K_1 and K_2 are modified Bessel functions of the first and second orders, respectively. We plot in fig. 3.1 the evolution of Y as x evolves according to (3.4.17).

As one can notice, there is an x_f (~ 20 for WIMPs) when the particle decouples, i.e. it stops interacting with the other particles. Before this event, the particle density followed the equilibrium function Y_{eq}. Thereafter, its Y settles at a constant value since its interaction rate is negligible compared to the Hubble term. Also, we see that the highest cross section $\sigma_{\chi\phi}$ (with $\lambda = 10^{-1}$) corresponds to the solution which shows the largest x_f, and therefore freezes out the latest; and the lowest $\sigma_{\chi\phi}$ represents the lowest x_f and decouples the earliest.

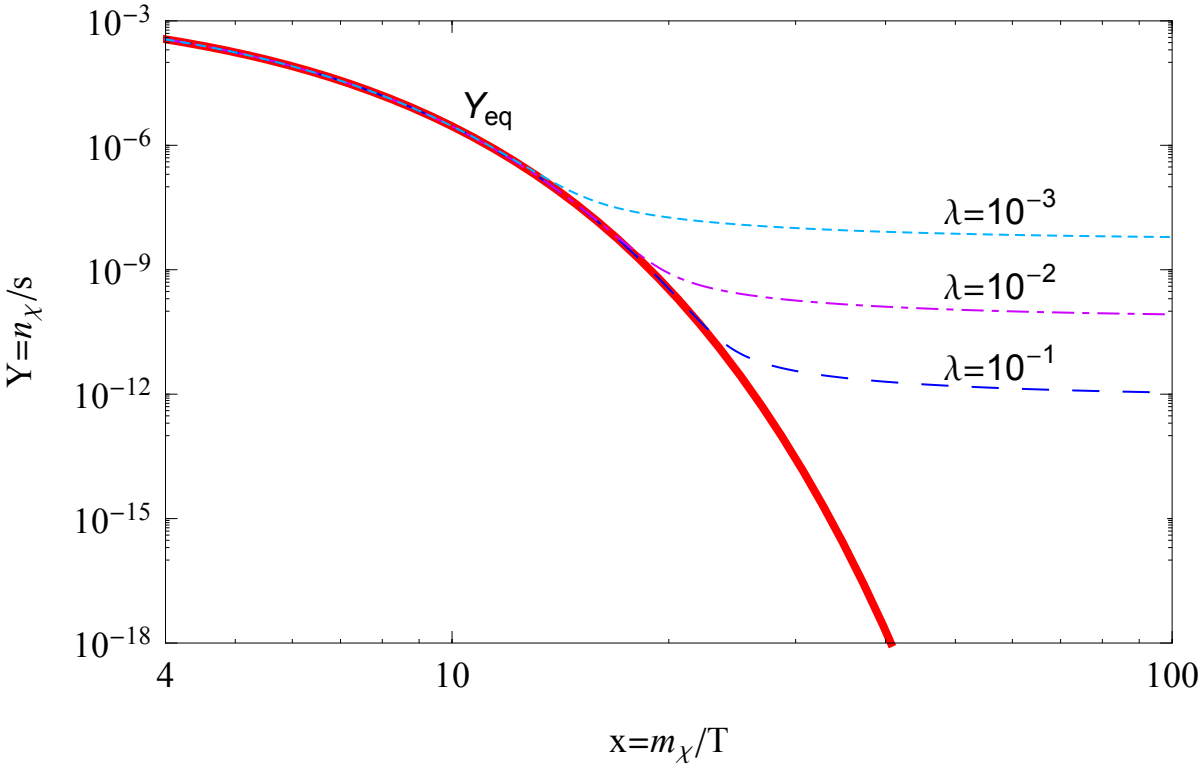

Figure 3.1: This figure shows how a nonrelativistic particle decouples. In it, are shown the equilibrium distribution $Y_{\rm eq}$ (red line) which behaves as $Y_{\rm eq} = n_{\rm eq}/s = \frac{45 g_\chi}{4\pi^4}\frac{x^2 K_2(x)}{h(m_\chi/x)}$; and numerical solutions of Y for $\lambda = 10^{-1}$, $\lambda = 10^{-2}$ and $\lambda = 10^{-3}$. We took $m_\chi = 100$ GeV and $m_\phi = 0$.

4 Dark Matter Detection

This chapter is dedicated to the overview of experiments and theoretical tools which are the basis for ruling out or constraining models which include possible dark matter candidates. Direct and indirect detection constraints will be used further in our text, therefore a brief survey and study of them will be provided.

4.1 Direct detection of Dark Matter

Although WIMPs are only weakly coupled to baryons, they can occasionally scatter elastically off nuclei. Several experiments [62] try to look for possible direct detection signals. Examples of such experiments are:

- **XENON1T** experiment [63];
- **LUX** (**L**arge **U**nderground **X**enon) experiment [64];
- and **PandaX-II** experiment [65],

whose limits we plot in figure 5.5 along with other sources, shown for reference, such as **CDMS** (**C**ryogenic **D**ark **M**atter **S**earch) [66] and **XENON100** [67].

The direct detection experiments try to measure the nuclei recoil energies, which are the result from interactions. The energies involved are estimated to be of order 10 keV, which is below the typical nuclear energy scales, therefore the non-relativistic limit ($v \ll c$) can be taken within the calculations. The magnitude of the WIMP-nucleus scattering cross section is sensitive to the exact form of the interactions of the dark matter particle with the individual nucleons. Because of that, we need to distinguish spin-dependent from spin-independent interactions for the experimental data are separated into these two classes.

For spin-dependent interactions, the scattering amplitude changes sign with spin direction, so that paired (null total spin) nucleons contribute zero to the full scattering amplitude and only the residual unpaired (nonzero total spin) nucleons contribute. Thus only nuclei with an odd number of protons plus neutrons can probe spin-dependent interactions. For spin-independent interactions, all the partial scattering amplitudes (related to each nucleon) are summed no matter the pairing of nuclear spins. The three collaborations cited above probe these two types of interactions.

Below we classify the interactions [68] relevant to direct detection for a dark matter χ (a scalar φ or a fermion ψ) in the low velocity regime (since we consider cold dark matter):

- **Vector-vector** interaction. $\bar{\chi} \overleftrightarrow{\partial}_\mu \chi \bar{q} \gamma^\mu q \overset{v \ll c}{\simeq} 2m\bar{\chi} \overleftrightarrow{\partial}_\mu \chi \left[a^\dagger a + b^\dagger b\right] \delta^{\mu 0}$ is spin-independent because no spin operators appear inside of it;

- **Vector-axial** interaction. $\bar{\chi}\overleftrightarrow{\partial}_\mu\chi\bar{q}\gamma^\mu\gamma_5 q \overset{v\ll c}{\simeq} 2m\bar{\chi}\overleftrightarrow{\partial}_\mu\chi\left[a^\dagger a\left(\xi^\dagger\sigma^i\xi\right)+b^\dagger b\left(\eta^\dagger\sigma^i\eta\right)\right]\cdot$ $\cdot\,\delta^{\mu i}$ is spin-dependent because σ^i are spin operators;
- **Scalar-pseudoscalar** interaction. $\bar{\chi}\chi\bar{q}\gamma_5 q \overset{v\ll c}{\simeq} \bar{\chi}\chi\times 0$ is spin-independent for it is negligible in this limit;
- **Scalar-scalar** interaction. $\bar{\chi}\chi\bar{q}q \overset{v\ll c}{\simeq} 2m\bar{\chi}\chi\left[a^\dagger a+b^\dagger b\right]$ is spin-independent for the same reason as for the vector-vector interaction,

where q represents a quark field; γ^μ is a dirac matrix and $\bar{\chi}$ represents either $\varphi^\dagger$ or $\bar{\psi}$. We choose not to describe interactions with $\Gamma^\mu=\gamma^\mu$, γ_5, $\gamma^\mu\gamma_5$ for the $\bar{\psi}\Gamma^\mu\psi$ bilinears, since the goal here is to define spin-dependent and spin-independent interactions; also because, later on in sec. 5.2.3, we deal with a WIMP which interacts with quarks with a trivial $\Gamma^\mu=1$, i.e. as $\bar{\psi}\psi$.

The scalar and vector quark bilinears just yield the number operator. Therefore, when these operators are evaluated in the nuclear state, they add coherently. The axial-vector bilinear $\bar{q}\gamma^\mu\gamma_5 q$ on the other hand yields the spin operator, and hence couples to the net spin of the nucleus. The sum over the entire nucleus for the two cases is given in [68].

There are no χ bilinear terms of the kind $\bar{\chi}\partial_\mu\partial_\nu(\chi)\,\bar{q}\sigma^{\mu\nu}q$ (two derivatives coupled to a totally antisymmetric tensor[1]) since they yield zero. Even if the operation of the derivatives was different, e.g. $\partial_\mu\bar{\chi}\partial_\nu\chi$ or $\partial_\mu\partial_\nu(\bar{\chi})\,\chi$, the result would be null.[2]

4.1.1 Theoretical description

In order to theoretically describe direct detection of WIMP collisions against nuclei, we need to introduce some tools. We describe theoretically only the SI cross section treatment, since only this kind will be necessary in sec. 5.2.3 where we describe the dark matter constraints on the $3-3-1$ model (the DM there is the fermion n_{R_3}). There we find out that the interaction of n_{R_3} with quarks is given mostly by $\propto\overline{(n_{R3})^c}n_{R3}\bar{q}_i q_i$, thus SI interaction.

For an interaction of the kind

$$\mathcal{L}_{\text{int}}=G_q\bar{\chi}\chi\bar{q}q \quad , \tag{4.1.1}$$

where χ is a majorana fermion and q is a quark flavour, the dark matter-nucleus cross section is spin-independent (SI) (see ref. [68]),

$$\sigma_{\chi N}=\frac{4}{\pi}\frac{m_N^2M_\chi^2}{(m_N+M_\chi)^2}\left[(A-Z)\,f_n+Zf_p\right]^2 \quad , \tag{4.1.2}$$

where A and Z are respectively the mass and the atomic numbers of the target nucleus. For example, xenon has $Z=54$ and $A=131$. m_N is the nucleon mass which is equal to

[1] $\sigma^{\mu\nu}=\frac{i}{2}\left[\gamma^\mu,\gamma^\nu\right]=\frac{i}{2}\left(\gamma^\mu\gamma^\nu-\gamma^\nu\gamma^\mu\right)$.

[2] Because of the hermiticity of the Lagrangian, the last term is zero. It can be shown that its hermitian conjugate is minus the term itself.

$m_p \simeq 938.27\,\mathrm{GeV}$ for the proton and $m_n \simeq 939.57\,\mathrm{GeV}$ for the neutron.

The effective coupling to neutrons and protons $f_{p,n}$ can be written in terms of the dark matter couplings to quarks[3]. In the case of a scalar interaction,

$$f_{p,n} = \sum_{q=u,d,s} \frac{G_q}{\sqrt{2}} f_{Tq}^{(p,n)} \frac{m_{p,n}}{m_q} + \frac{2}{27} f_{Tg}^{(p,n)} \sum_{q=c,b,t} \frac{G_q}{\sqrt{2}} \frac{m_{p,n}}{m_q} \quad , \tag{4.1.3}$$

where G_q denotes the dark matter effective coupling for a given quark species as in eq. (4.1.1). The first term on the right-hand side of eq. (4.1.3) reflects scattering with light quarks while the second term accounts for interactions with gluons through a heavy quark loop; $f_{Tq}^{(p,n)}$ are density functions of each quark q within the proton p or neutron n; and $f_{Tg}^{(p,n)}$ are density functions of gluons within p or n and are related to the quark density functions $f_{Tq}^{(p,n)}$ through $f_{Tg}^{(p,n)} = 1 - \sum_{q=u,d,s} f_{Tq}^{(p,n)}$. The values $f_{Tq}^{(p,n)}$ have been measured to be (we write only the mean values)

$$f_{Tu}^{p} = 0.020,\ f_{Td}^{p} = 0.026,\ f_{Ts}^{p} = 0.118 \quad \therefore \quad \sum_{q=u,d,s} f_{Tq}^{p} = 0.164 \quad , \tag{4.1.4}$$

$$f_{Tu}^{n} = 0.014,\ f_{Td}^{n} = 0.036,\ f_{Ts}^{n} = 0.118 \quad \therefore \quad \sum_{q=u,d,s} f_{Tq}^{n} = 0.168 \quad . \tag{4.1.5}$$

Consequently, they yield

$$f_{Tg}^{p} = 1 - \sum_{q=u,d,s} f_{Tq}^{p} \quad = \quad 0.836 \quad , \tag{4.1.6}$$

$$f_{Tg}^{n} = 1 - \sum_{q=u,d,s} f_{Tq}^{n} \quad = \quad 0.832 \quad . \tag{4.1.7}$$

If one can define $G_0 \equiv G_q/m_q$[4], this assumption leads to

$$\begin{aligned} f_{p,n} &= \frac{G_0 m_{p,n}}{\sqrt{2}} \left\{ \sum_{q=u,d,s} f_{Tq}^{(p,n)} + \frac{2}{9} f_{Tg}^{(p,n)} \right\} \quad , \\ &= \frac{G_0 m_{p,n}}{9\sqrt{2}} \left\{ 2 + 7 \sum_{q=u,d,s} f_{Tq}^{(p,n)} \right\} \quad . \end{aligned}$$

[3] Dark matter does not couple directly to gluons due to its non-coloured nature.

[4] In sec. 5.2.3, our fermion dark matter candidate n_{R3} interacts with quarks mainly through the scalars channel. On one hand we have $\propto \overline{(n_{R3})^c} n_{R3} \phi_2$, whereas on the other hand the Yukawa potential provides $\left(m_u^{ij} \bar{u}_{iL} u_{jR} \tilde{H} + m_d^{ij} \bar{d}_{iL} d_{jR} H + \text{h.c.} \right)$. In the end, the n_{R3} interaction with q is given through a scalar propagator, yielding the effective coupling $\propto m_{q_i} \overline{(n_{R3})^c} n_{R3} \bar{q}_i q_i$ (observe that a mixing of ϕ_2 with H is necessary for the interaction term to exist). Therefore, in our case, one can separate G_0 into G_q/m_q for each separate quark.

Since $\sum_{q=u,d,s} f_{Tq}^p \simeq \sum_{q=u,d,s} f_{Tq}^n$, consequently $f_p \simeq f_n$, we can write eq. (4.1.2) as

$$\sigma_{\chi N} \simeq \frac{4}{\pi} \frac{m_N^2 M_\chi^2}{(m_N + M_\chi)^2} A^2 f_p^2 \quad , \tag{4.1.8}$$

which enables the definition of a cross section per nucleon,

$$\sigma_{\chi,p} \equiv \frac{\sigma_{\chi N}}{A^2} = \frac{4}{\pi} \frac{m_N^2 M_\chi^2}{(m_N + M_\chi)^2} f_p^2 \quad , \tag{4.1.9}$$

with f_p given by

$$\begin{aligned} f_p &= \frac{G_0 m_{p,n}}{9\sqrt{2}} \left\{ 2 + 7 \sum_{q=u,d,s} f_{Tq}^p \right\} \\ &\simeq \frac{9.38 \cdot 10^{-1}\,\text{GeV}}{9\sqrt{2}} \left\{ 2 + 7 \cdot 0.164 \right\} G_0 \left[\text{GeV}^{-3}\right] \\ &\simeq 0.23 \cdot \left(\frac{G_0}{\text{GeV}^{-3}} \right) \text{GeV}^{-2} \quad . \end{aligned} \tag{4.1.10}$$

Substituting the latter into the $\sigma_{\chi,p}$ expression, it yields

$$\sigma_{\chi,p} \simeq 0.07 \cdot \frac{m_N^2 M_\chi^2}{(m_N + M_\chi)^2} \left(\frac{G_0}{\text{GeV}^{-3}} \right)^2 \text{GeV}^{-4} \quad . \tag{4.1.11}$$

Now, using the conversion factor

$$1\,\text{pbarn} = 10^{-36}\ \text{cm}^2 = 2.5681 \cdot 10^{-9}\ \text{GeV}^{-2} \quad , \tag{4.1.12}$$

we have

$$\begin{aligned} \sigma_{\chi,p} &\simeq \frac{0.07}{2.5681 \cdot 10^{-9}} \cdot \left(\frac{m_N^2 M_\chi^2 / (m_N + M_\chi)^2}{\text{GeV}^2} \right) \left(\frac{G_0}{\text{GeV}^{-3}} \right)^2 \text{pbarn} \\ &\simeq 2.7 \cdot 10^7 \cdot \left(\frac{m_N^2 M_\chi^2 / (m_N + M_\chi)^2}{\text{GeV}^2} \right) \left(\frac{G_0}{\text{GeV}^{-3}} \right)^2 \text{pbarn} \quad . \end{aligned} \tag{4.1.13}$$

Thus in the end we have the cross section per nucleon dependent on the coupling G_0 which is dependent on the coupling of the dark matter particle to the Higgs particle $C_{\text{DM}^2 H}$. Therefore the direct detection experiments will constrain the latter in a way that the cross section per nucleon will be below the limits set by them.

One comment is due. Note that we obtained eq. (4.1.13) through some approximations. Though this derivation provides enlightenment to the theoretical procedure, in reality if one desires to compare precisely theory with experiment, he must obtain $\sigma_{\chi,p} = \frac{\sigma_{\chi N}}{A^2}$ through eq. (4.1.2) and not via eq. (4.1.8).

Below, we present five upper bounds on the SI cross section $\sigma_{\chi,p}^{\text{SI}}$, as a function of the

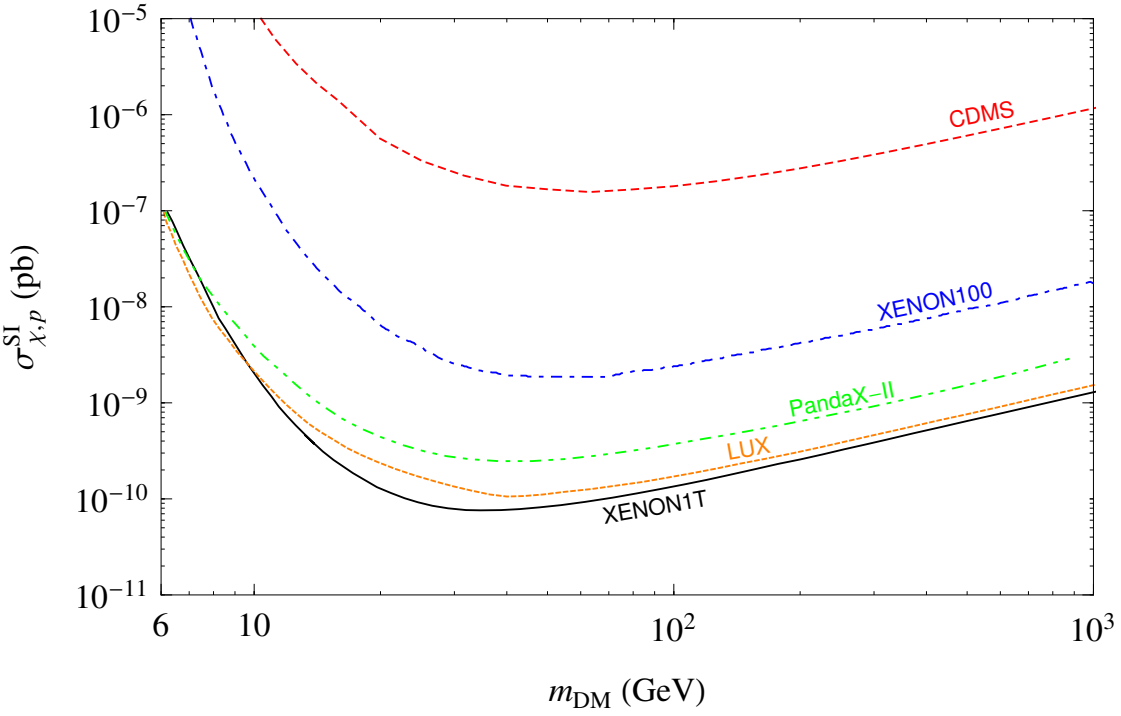

Figure 4.1: Spin-independent limits on $\sigma_{\chi,p}$ from XENON1T [63], PandaX-II [65], LUX [64], CDMS [66] and XENON100 [67] experiments.

dark matter particle mass m_{DM}.

4.2 Indirect detection of Dark Matter

The philosophy behind indirect detection of dark matter consists in detecting the signatures of the annihilations or decays of dark matter particles in the fluxes of cosmic rays, for example: charged particles (electrons, positrons, protons, antiprotons, ...), hard photons and neutrinos. Additonally, the measurements made by the PLANCK satellite (as well as WMAP and COBE before it) probe the anisotropies of the CMB as hints for dark matter.

We provide the references for some current experiments:

Neutrinos. Large neutrino detectors such as IMB [69], Kamiokande [70], Macro [71], Super-Kamiokande [72], AMANDA [73] and BAIKAL [74] have obtained constraints on DM neutrino fluxes;

Charged particles. Results have already been obtained with PAMELA [75], Fermi-LAT [76] and AMS [77] (all related to positron measurements). Searches for antiparticles (e^+, $\bar{p}$, antideuterons, ...) are cleaner for they are much less abundant than the corresponding particles;

Hard photons. Photons travel in straight lines through our galaxy due to its electric charge neutrality, making the task to locate its source simpler, while for charged

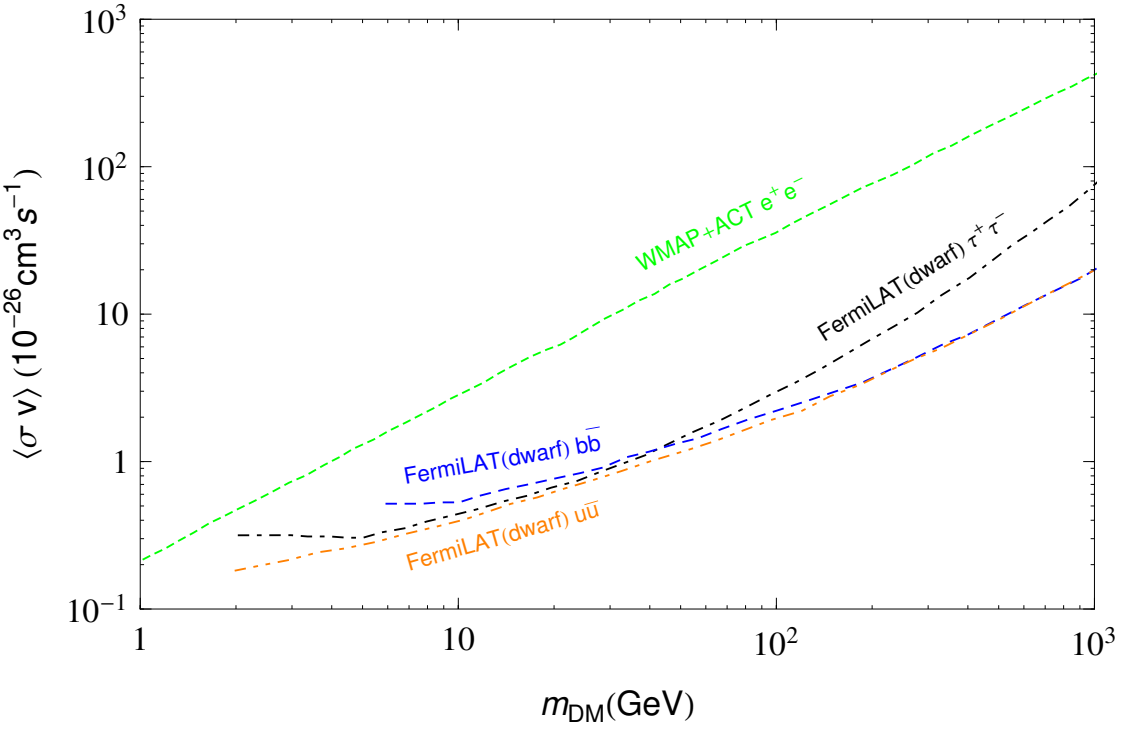

Figure 4.1: Indirect detection limits on $\langle\sigma v\rangle$ from CMB anisotropies analysis [84] for DM annihilation into e^+e^- pairs (green dashed line) and indirect searches from searches of the Milky Way dwarf spheroidal satellite galaxies [81] for DM annihilation into $\tau^+\tau^-$, $b\bar{b}$ and $u\bar{u}$ pairs (black dot-dashed, blue dashed and orange dot-dot-dashed lines respectively).

particles, the uncertainty on the source location is an extra factor since our knowledge about the galactic magnetic field is limited, thus it would be impossible to focus at a certain direction where the products signal would be particularly strong. Another advantage of γ rays is that they are present in a variety of possible final states: hard photons can originate from the decay of neutral pions and other hadrons that result from the hadronization of $\bar{q}q$ final states or the decay of τ leptons, and can be produced from energetic e^+ or e^- through inverse Compton scattering of ambient photons. The most stringent limits stem from [78–81] which assume the DM annihilation into different channels such as $b\bar{b}$ or $\tau^+\tau^-$, which in turn decay into γ rays; we plot [81] in fig. 4.1;

CMB photons. The limits on $\langle\sigma v\rangle$ stem from the fact that WIMP annihilations heat up the plasma in the recombination epoch when neutral atoms first formed [82,83], thereby delaying the decoupling of the CMB photons and distorting the pattern of CMB anisotropies. The strongest limit on $\langle\sigma v\rangle$ from spectral distortions of the CMB, assuming WIMP annihilation into e^+e^- pairs, is contained in ref. [84], which is also drawn in fig. 4.1.

The results of indirect searches and CMB analysis shown in fig. 4.1 are in terms of the thermal annihilation cross section $\langle\sigma v\rangle$. For the former, this fact is not hard to understand: after the WIMP freezout, if its number density is high enough, it can produce

through self-annihilation energetic standard model particles such as e^+e^-, $\bar{b}b$ or $\tau^+\tau^-$ (this production happens up to the point when $n_\chi \sim H/\langle\sigma v\rangle$, as will be explained in sec. 6.1). These particles in turn yield γ rays, consequently the γ signal flux ϕ_s (photons cm^{-2} s^{-1}) depends linearly on $\langle\sigma v\rangle$. Whereas for the CMB analysis, the dependence on $\langle\sigma v\rangle$ stems from the fact that WIMP annihilation heats up the plasma in the recombination epoch, thus delaying the decoupling of the CMB photons and distorting the pattern of CMB anisotropies. The energy release per unit time and unit volume $d\rho_\chi/dt$ depends linearly on $\langle\sigma v\rangle$.

5 Standard thermal scenario applications

In this section we focus on two works which rely on the the standard scenario of thermal WIMP. We will discuss in 5.1 the precise calculation of relativistic degrees of freedom in the early universe, considering an accurate treatment of the QCD phase transition [85], along with the consequences on the WIMP relic density evaluation in a model-independent way. The second work in sec. 5.2 is focused on a specific model, the $B-L$ extension of the SM [86], in which we assess the possibility of a fermionic dark matter candidate.

5.1 Behaviour of h and g near T_c and its consequences

We now pull the attention of the reader to the behaviour of the functions h and g for the temperature region around $T_c \sim 300\,\mathrm{MeV}$.

Why is a careful study around T_c necessary for the evaluation of h and g? For early studies [60,87], the entropy density s and energy density of the plasma ρ (and consequently h and g) were calculated treating the particles contained within the plasma as relativistic free particles, i.e. ignoring all the interactions between SM particles. However, it was realized [59, 60] that this approach is not valid for temperatures near the deconfinement transition from hadronic to partonic degrees of freedom, i.e. from protons, pions, kaons, etc. to quarks and gluons. For WIMP masses around $m_\chi \sim 20 \cdot T_c \sim 6$ GeV, the respective relic densities are affected by the QCD crossover transition, therefore a careful study should be carried.

Why should one worry about the precision on h and g? Currently, in the framework of the minimal cosmological model, measurements on the CMB by the PLANCK collaboration set the scaled CDM relic density to $\Omega_c h^2 = 0.1193 \pm 0.0014$ [45], thus with an error of less than 1.5%. Therefore, if one desires to take advantage of this precision and draw predictions from it, theoretical results should have an equal or higher precision.

5.1.1 Our calculation method of h and g

Much above the electron mass, we treat all the SM particles without strong interactions as free particles. Therefore, for leptons, electroweak gauge bosons and the SM Higgs boson, we use eqs. (3.3.18) and (3.3.37) to calculate their degrees of freedom. For $g(T)$ and $h(T)$ evaluation, we consider free massive $W^\pm$ and Z bosons (with three d.o.f. each) and one physical Higgs boson, even above the electroweak symmetry breaking where one

c_t	a_n	b_n	d_n
3.8706	−8.7704	3.9200	0.3419
t_0	a_d	b_d	d_d
0.9761	−1.2600	0.8425	−0.0475

Table 5.1: Parameters used in eq. (5.1.1) to describe the pressure of QCD with $2+1$ flavours.

should in principle use a more precise description and consider massless gauge bosons (with two d.o.f. each) and a massive complex Higgs doublet (with four d.o.f.). The difference between these treatments is small, and only affects WIMPs with massses above ~ 2 TeV. A final comment about this evaluation of free particles is in order: for the Higgs physical mass $m_H \simeq 125\,\mathrm{GeV}$, within the Standard Model, the electroweak symmetry breaking only leads to a smooth crossover [88–90], thus the comoving entropy density remains constant[1], as assumed in the derivation of eq. (3.4.17).

Now we focus on the evaluation of h and g evaluated near the deconfinement temperature (a smooth crossover [91]). Recall that the former can be found from the entropy density s, which from (3.3.33) reads $s(T) = [\rho(T) + p(T)]/T$, whereas the latter is evaluated from the energy density ρ. First we discuss the pressure $p(T)$.

We use the results of a lattice calculation with $N_f = 2+1$ active flavours (i.e. u and d quarks have same masses and the s quark has a higher mass) [92], where its temperature application range is 100 MeV to 400 MeV. This evaluation is consistent with the similiar, independent work [93]. The ref. [92] provides a parametrization of the pressure due to u, d, s quarks and gluons valid in that temperature interval:

$$\frac{p}{T^4} = \frac{1}{2}\left[1 + \tanh\left(c_t\left(\bar{t} - t_0\right)\right)\right] \times \frac{p_{\mathrm{id}} + a_n/\bar{t} + b_n/\bar{t}^2 + d_n/\bar{t}^4}{1 + a_d/\bar{t} + b_d/\bar{t}^2 + d_d/\bar{t}^4} \quad , \tag{5.1.1}$$

where $\bar{t} \equiv T/T_c$, $T_c = 154\,\mathrm{MeV}$ being the QCD transition temperature. $p_{\mathrm{id}} = 19\pi^2/36 = \pi^2/30 \cdot \left[7\left(\boldsymbol{g}_u + \boldsymbol{g}_d + \boldsymbol{g}_s\right)/8 + 8\boldsymbol{g}_g\right]$ is the ideal gas value of p/T^4 for QCD with three massless quarks. The values of the numerical parameters appearing in eq. (5.1.1) are given in table 5.1. For $T \gg T_c$ (or $\bar{t} \gg 1$), eq. (5.1.1) provides $\frac{p}{T^4} = p_{\mathrm{id}}$ since $\tanh(x) \simeq 1$ for large x. According to [92], eq. (5.1.1) is in agreement with the available perturbative calculations at temperatures higher than 400 MeV. Therefore, we use this pressure parameterization for the u, d, s quarks and gluons contribution for temperatures above 100 MeV.

Now we need to know the dependence of ρ on the plasma temperature. This is obtained from the relation between the trace of the energy-momentum tensor (also called trace anomaly) and the pressure [92]:

$$\frac{I(T)}{T^4} = \frac{\rho - 3p}{T^4} = T\frac{d}{dT}\left(\frac{p}{T^4}\right) \quad . \tag{5.1.2}$$

[1] If the SM electroweak breaking was a phase transition, the comoving entropy density would be discontinuous at $T = v_{\mathrm{SM}} \simeq 246\,\mathrm{GeV}$.

We now have two equations for two functions, $s(T)$ and $\rho(T)$. After evaluating them, one needs just to calculate eqs. (3.3.18) and (3.3.37) to find $h(T)$ and $g(T)$.

The effect of the charm quark is not negligible at temperatures around T_c [94]. Its contribution to the functions $g(T)$ and $h(T)$ using lattice QCD results from table 6 of [95] using the physical ratio of charm and strange quark masses, $m_c/m_s = 11.85$ [96]. This yields p_c/T^4, from which the charm contributions to $\rho(T)$ and $s(T)$ can be obtained as described above. This description is valid for $T \leq 1\,\mathrm{GeV}$. For larger temperatures we smoothly match to the ideal gas results (3.3.18) and (3.3.37), using a fit function similar to (5.1.1) with $p_{\mathrm{id}}^c = 7\pi^2/60 = \pi^2/90 \cdot 7\boldsymbol{g}_c/8$ and different values for coefficients and powers to interpolate between the two regimes. This ensures that the functions g and h, as well as their first derivatives, are smooth everywhere. Smoothness of h is specially important for the Boltzmann equation (3.4.17), since it depends on $g_*^{1/2} \propto T \cdot dh/dT + 3$.

For the bottom and top quarks, their contributions are only significant at high temperatures, where the QCD interactions have become relatively small. Therefore, we treat these quarks as free particles, with on-shell masses given by the Particle Data Group [97]. Their contributions to pressure are then $p_{\mathrm{b+t}} = 2 \cdot 7\pi^2/60 = 2 \cdot \pi^2/90 \cdot 7\boldsymbol{g}_c/8$.

For $T < T_c$, the QCD behaviour can be best described by the hadron resonance gas model [98], in which all the hadrons and hadron resonances are considered to contribute to the thermodynamics quantities as free particles. This has been used in the early treatments [99, 100]. Ref. [92] shows that for temperatures between 100 MeV and T_c, it matches well to the QCD results parameterized in eq. (5.1.1). A parametrization of the trace anoaly in this model can be given by [98]:

$$\frac{I(T)}{T^4} = \frac{\rho - 3p}{T^4} = a_1 T + a_2 T^2 + a_3 T^4 + a_4 T^{10} \quad , \tag{5.1.3}$$

where $a_1 = 4.654\,\mathrm{GeV}^{-1}$, $a_2 = -879\,\mathrm{GeV}^{-3}$, $a_3 = 8081\,\mathrm{GeV}^{-4}$, $a_4 = -7039000\,\mathrm{GeV}^{-10}$. This parametrization is valid for $70\,\mathrm{MeV} \leq T \leq T_c$. We use it to describe the contribution from strongly interacting particles for all temperatures $T < 100\,\mathrm{MeV}$, using cubic splines to interpolate smoothly to QCD results at $T > 100\,\mathrm{MeV}$. At very low temperatures, eq. (5.1.3) is not accurate, since the hadronic contributions to g and h should in principle account for charmed particles. However, this is not important for us since hadronic contributions become exponentially small at $T \ll m_\pi = 140\,\mathrm{MeV}$. Hence, for $T \ll 100\,\mathrm{MeV}$ the hadronic contribution is in any case very small and does need a very accurate description.

If one inverts eq. (5.1.2), the pressure can be calculated:

$$\frac{p(T)}{T^4} = \frac{p_0}{T_0^4} + \int_{T_0}^{T} dT' \frac{I(T')}{T'^5} \quad , \tag{5.1.4}$$

using the numerical result $p(T_0)/T_0^4 = 0.1661$ at $T_0 = 70\,\mathrm{MeV}$ [98]. The integral in eq. (5.1.4) can be analytically evaluated if $I(T)$ is given by eq. (5.1.3). Therefore, once again we are given an analytical parameterization of the pressure and can compute ρ and s as

described above.

At temperatures below 1 MeV, the effect of neutrino decoupling should be included[2]. At first, right after the neutrino decoupling the expansion of the universe affects photons and neutrinos in the same way, i.e. the photon and neutrino temperratures remain the same. This changes only once e^+e^- pairs begin to annihilate, at $T \simeq m_e$. Since neutrinos are already (almost) decoupled by this time, the entropy that was stored in electrons and positrons gets transferred (almost) entirely to photons, not to neutrinos. In the limit where neutrino decoupling was complete when electron decoupling began, this argument shows that for $T \ll m_e$ the ratio of relic photon and neutrino temperatures is $T_\gamma/T_\nu = (11/4)^{1/3}$. Actually (electrons) neutrinos were not completely decoupled at $T \sim m_e$, when e^+ and e^- start to annihilate. Therefore, some energy and entropy from e^+e^- annihilation goes to the neutrinos. This effect can be described by writing

$$h = 2\left[1 + \frac{7}{8} N_{\text{eff}} \left(\frac{4}{11}\right)\right] \quad , \tag{5.1.5}$$

$$g = 2\left[1 + \frac{7}{8} N_{\text{eff}} \left(\frac{4}{11}\right)^{4/3}\right] \quad , \tag{5.1.6}$$

with $N_{\text{eff}} \simeq 3.046$ [101].[3] Note that these expressions include the contribution from the photon, with $\boldsymbol{g}_\gamma = 2$. Eqs. (5.1.5) and (5.1.6) are valid for $T \ll m_e$, in practice for $T \leq 50\,\text{keV}$. As mentioned, for $T > 1\,\text{MeV}$ we have $T_\nu = T_\gamma$. For $50\,\text{keV} < T < 1\,\text{MeV}$, we use numerical results from figure 1 of [102] to determine the evolution of T_ν with respect to T_γ. This can then be plugged into eqs. (5.1.5) and (5.1.6) instead of $T_\nu/T_\gamma = (4/11)^{1/3}$ to compute the photon and neutrino contribution to $g(T)$ and $h(T)$. Note that the temperature T is defined to be that of the photons, $T = T_\gamma$.

After performing all the theoretical procedure described above, we obtain in fig. 5.1 the precise behaviour for h and g, as well as $g_*^{1/2}$. The behaviour of these functions will be in the next section compared with other calculation methods for obtaining h, g and $g_*^{1/2}$, which will then give us a notion of what has been accomplished with our new study.

What is important to notice here is that these functions do not have any discontinuity and behave smoothly at all temperatures, even for the most delicate regions [100 MeV, 1 GeV] and around 246 GeV, where respectively the QCD transition occurs and the electroweak gauge symmetry is restored. The smooth behaviour is a consequence of crossover transitions as opposed to phase transitions and should be observed for a correct theoretical result.

[2] The interaction rate of ν_μ and ν_τ actually becomes smaller than the Hubble parameter at a temperature of several MeV.

[3] Strictly speaking, the neutrinos cannot be assigned a temperature after electron decoupling, since their distribution is non-thermal: the part of the energy from e^+e^- annihilation which goes to neutrinos mostly goes to neutrinos with $E \simeq m_e$ at the time of the annihilation; and since neutrino oscillation probabilities are energy dependent, they also distort the thermal spectrum of individual neutrinos. Nevertheless eqs. (5.1.5) and (5.1.6) accurately describe the behaviour of the functions g and h at $T \ll m_e$.

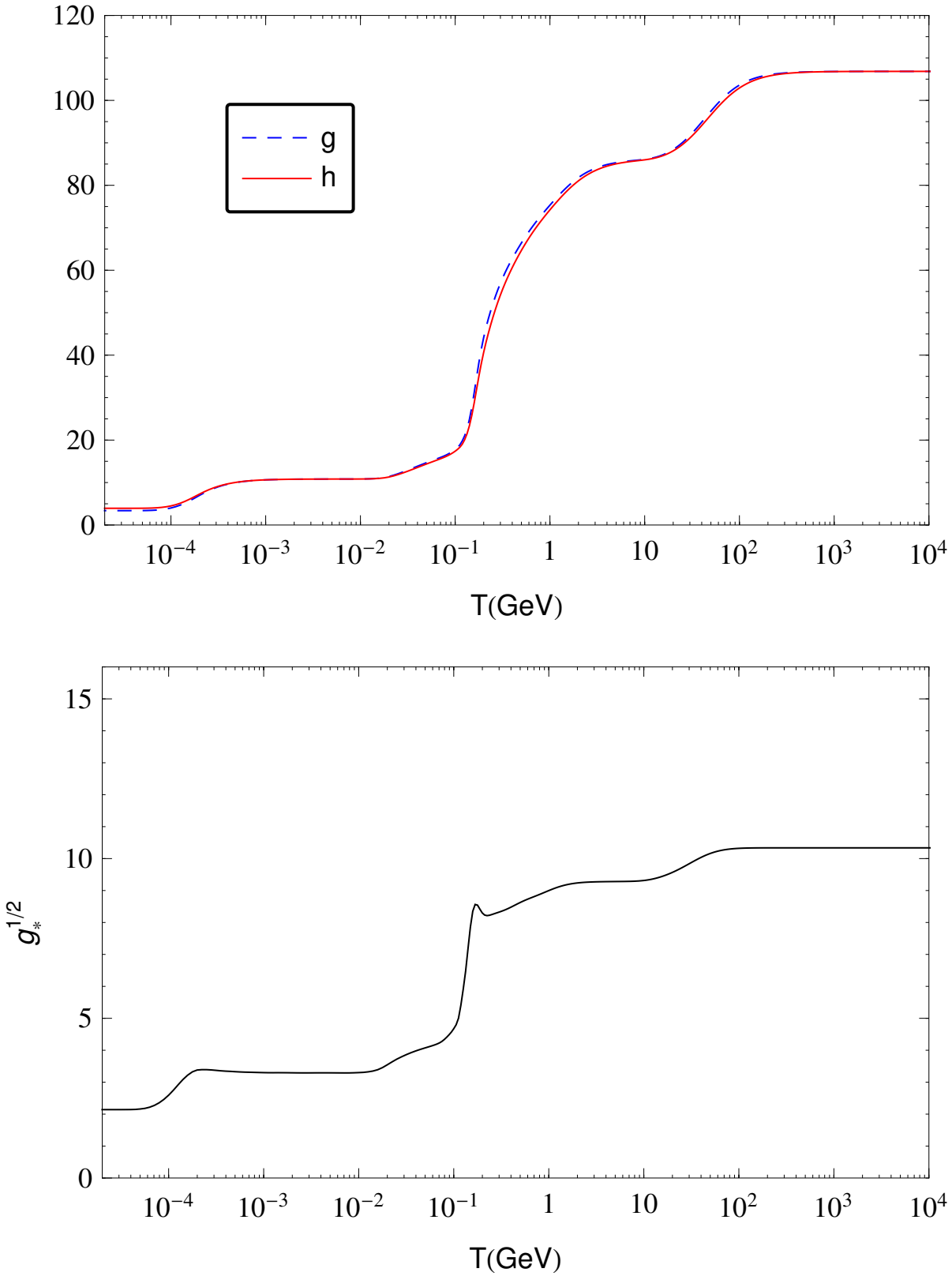

Figure 5.1: The functions $g(T)$, $h(T)$ (upper frame) and $g_*^{1/2}(T)$ (lower) defined in eqs. 3.4.4, 3.4.3 and 3.4.16 as a function of the plasma temperature. For $g_*^{1/2}(T)$, the peak at approximately $T = 10^{-1}$ GeV is due to the smooth crossover of the QCD deconfinement transition. These curves were obtained following our method described in the text.

5.1.2 Comparison with previous studies

In order to compare our work with known calculation studies for g, h and $g_*^{1/2}$, we first briefly review the evaluation methods encoded in the widely used program packages for the calculation of the WIMP relic density `DarkSUSY` [103], `micrOMEGAs` [104] and `SuperISO` [105].

There existed some attempts to describe the thermodynamics of the early universe around the deconfinement transition. In [99], the interactions between hadrons and between partons were approximated by simple non-relativistic potentials. On the other hand, ref. [100] used free particles and defined the transition temperature from the hadronic to the partonic phase as the temperature where the two calculations give the same entropy density. The *hadron resonance gas model*, description of the hadronic phase, was used in all subsequent calculations at sufficiently low temperatures, including our own.

One problem of the simple definition of the transition temperature used in [100] is that it leads to a discontinuity in $g(T)$. To avoid this problem, ref. [58] used smooth functions interpolating between hadronic and partonic phases. While these functions ensure that not only $g\,(T)$ and $h\,(T)$, but also their derivatives are smooth, they were not based on dynamical considerations. The authors advocated estimating the uncertainty by using two quite different values, 150 and 400 MeV, for the transition temperature. The same functions were used in [59], the functions for a transition temperature of 150 MeV are still used by default in the computer packages mentioned above.

The first attempt to include the results of lattice QCD calculations was due to Hindmarsh and Philipsen [106]. At the same time the most accurate lattice QCD calculations did not include dynamical quarks. There was some evidence that the ratio of the true pressure to the corresponding value for non-interacting particles shows little dependence on the number of quark flavors [107]. Therefore, ref. [106] scaled the contribution of all strongly interacting partons by the same correction function, determined from pure glue lattice calculations [107]; at $T = 1.2\,\mathrm{GeV}$, these were matched to perturbative calculations [108].

The treatment by Laine and Schroeder [94] is rather similar. However, their results are based on a different set of pure glue lattice QCD calculations [109–113]. Moreover, they match to perturbative calculations at the much lower temperature of 350 MeV. Finally, they include the quark mass dependence up to next-to-leading order, $\mathcal{O}\,(g^2)$, in the perturbative expansion. In particular, they point out that charm quarks make non-negligible contributions already at temperatures of a few hundred MeV.

After commenting about the differences in the literature for the methods of treating the deconfinement transition, we plot in figs. 5.2 and 5.3 the functions $g\,(T)$, $h\,(T)$ and $g_*^{1/2}\,(T)$ evaluated following four different approaches: our method, devised in subsec. 5.1.1; and the evaluations used in Gondolo and Gelmini's [59], Laine and Schroeder's [94], and Hindmarsh and Philipsen's [106] works.

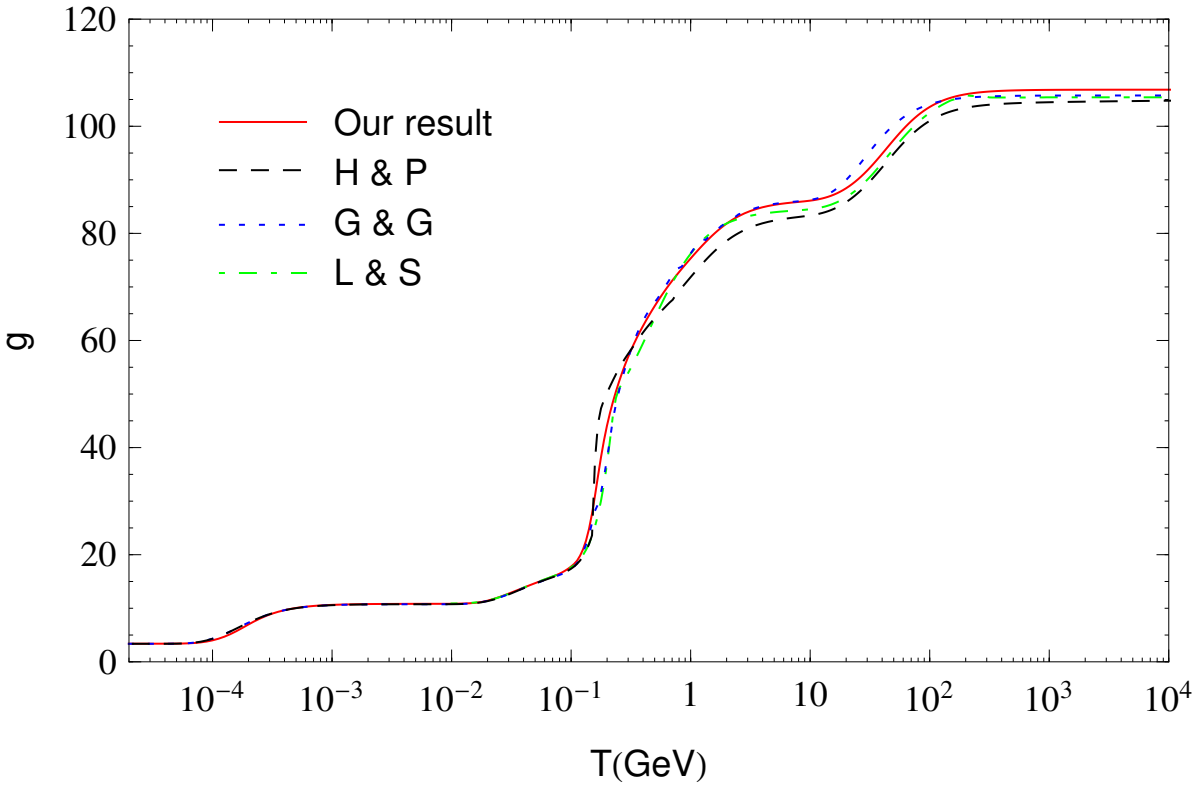

Figure 5.2: The function $g(T)$ defined in eq. (3.4.4), as a function of the temperature. The original calculation by Gondolo and Gelmini [59], based on results from [58], are shown by the blue dotted curve. The black dashed and green dot-dashed curves show results from Hindmarsh and Philipsen's [106] and Laine and Schroeder's [94] respectively, which are based on pure glue lattice QCD calculations. The red solid curves describe our results, which are based on lattice calculations with $N_f = 2+1$ dynamical quark flavours.

5.1.3 Impact of g, h and $g_*^{1/2}$ on the relic density value

Since we include the effect of e^+e^- decoupling on the neutrino bakground, described by $N_{\text{eff}} = 3.046$ in eq. (5.1.5), we obtained $h(T_{\gamma,0}) = 3.9387$ in our calculation; here the present temperature $T_{\gamma,0} = 2.7255 \pm 0.0006\,\text{K}$ [97]. Our current value of h is thus slightly higher than $h(T_{\gamma,0}) = 3.9138$ of ref. [106] and $h(T_{\gamma,0}) = 3.9139$ of ref. [103]. Note that for a given value of $Y_\chi(T_{\gamma,0})$, the final relic density $\Omega_\chi h^2$ is directly proportional to $h(T_{\gamma,0})\,T_{\gamma,0}^3$, since $\Omega_\chi h^2 \propto s_0$ from eq. (3.4.19).

There clearly are some differences between the four calculations. These are most visible near the QCD deconfinement transition. Moreover, the differences are more visible in $g_*^{1/2}$, largely due to the derivative term in eq. (3.4.16), which makes the differences between the four treatments more prominent. We notice that the older calculation [58] used in [59] overestimates $g_*^{1/2}$ to a moderate amount for $T \simeq 0.1\,\text{GeV}$, compared to all three calculations using results from lattice QCD. The treatment of ref. [106] yields a discontinuity at $T = T_c$, and hence a divergent derivative, giving a formally infinite spike in $g_*^{1/2}$. The continuity has been smoothed out in `micrOMEGAs` [104], from which we took

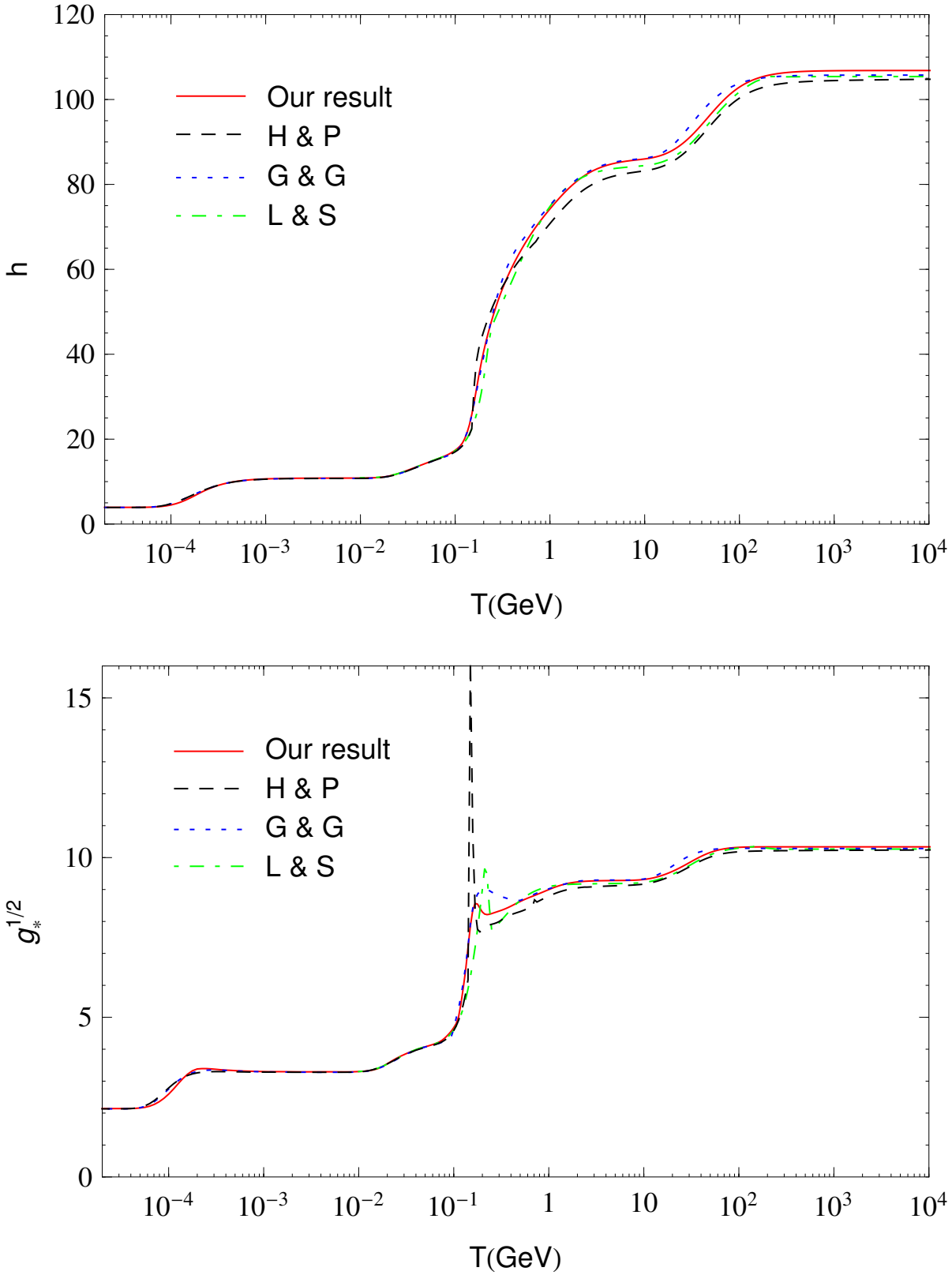

Figure 5.3: The functions $h(T)$ (top frame) and $g_*^{1/2}(T)$ (bottom) defined in eqs. (3.4.3) and (3.4.16), as a function of the temperature. The functions by Gondolo and Gelmini [59] based on [58] are shown by the blue dotted curves. The black dashed and green dot-dashed curves show results from Hindmarsh and Philipsen's [106] and Laine and Schroeder's [94]. The red solid curves describe our results.

the numerical results for g and h. We see that this treatment still gives a noticeable spike in $g_*^{1/2}$. Apart from this spike, ref. [106] predicts a smaller value of $g_*^{1/2}$ in this temperature range than we do. Finally, the prediction for $g_*^{1/2}$ from ref. [94] is quite close to our own result, except for some oscillatory behavior just above the QCD transition temperature.

In order to explore the effect of changes in h and $g_*^{1/2}$ on the WIMP relic density[4], we solve the Boltzmann equation (3.4.17) numerically, following the numerical procedure devised after that equation, in order to obtain the relic density $\Omega_\chi h^2 = 2.7889 \cdot 10^8 Y_0 \frac{m_\chi}{(1\,\mathrm{GeV})}$.

The change of the predicted WIMP relic density due to our more refined treatment of the functions h and $g_*^{1/2}$ is illustrated in figure 5.4. The upper frame shows results for a temperature independent $\langle\sigma v\rangle$, while in the lower frame we have assumed $\langle\sigma v\rangle \propto 1/x$. These behaviours describe the thermally averaged cross section at small velocity away from the poles (i.e. if the WIMPs cannot annihilate into any particle ϕ with $m_\phi \simeq 2m_\chi$) and thresholds (i.e. if the WIMPs are significantly heavier than all relevant final-state particles), for the cases where the annihilation occurs from a pure S-wave and pure P-wave initial state, respectively. The latter occurs, for example, for a Majorana WIMP annihilating into light SM fermions, or for a complex scalar annihilating through s-channel exchange of a gauge boson. Not unexpectedly, we observe the largest differences for WIMP masses of a few GeV, which decouple just above the QCD transition temperature. The differences amount to up to 9% for the pure S-wave, and up to 12% for the pure P-wave.

The results of figure 5.4 can be understood in more detail using the approximate analytical solution of the Boltzmann equation developed in refs. [60,61]:

$$Y_0 \;\propto\; \frac{x_f}{g_*^{1/2}\left(T_f\right)\langle\sigma v\rangle\left(T_f\right)} \quad , \qquad x_f \propto \ln\left(\frac{m_\chi g_*^{1/2}\left(T_f\right)\langle\sigma v\rangle\left(T_f\right)}{h\left(T_f\right)}\right) \quad . \tag{5.1.7}$$

Very roughly, $x_f \sim 20$ for WIMP masses and annihilation cross sections of interest. This equation shows that $g_*^{1/2}$ affects the final result more strongly than h does, which appears only logarithmically. The derivation of eq. (5.1.7) assumes that $g_*^{1/2}$ and h are constant around the WIMP decoupling temperature $T_f = m/x_f$. This is not a very good approximation near the QCD deconfinement transition, where these functions change rapidly, as we saw in fig. 5.3. However, we can see directly from the Boltzmann equation that the most relevant temperature range is around the decoupling temperature. At higher temperatures, Y is in any case close to its equilibrium value, which does not depend on $g_*^{1/2}$. At temperatures well below the decoupling temperature, i.e. for $x \gg x_f$, the right hand side of the Boltzmann equation (3.4.17) is suppressed by the explicit x^{-2} factor. If $\langle\sigma v\rangle \propto 1/x$, as in the lower frame of figure 5.4, the suppression at $x > x_f$ is even stronger. Sharp features in $g_*^{1/2}$ therefore give sharper features, with larger amplitudes, for pure P-wave annihilation than for pure S-wave annihilation.

We noticed earlier that the older treatment of [59] overestimates $g_*^{1/2}$ for some range of

[4] One needs to take into account only two of the three functions g, h and $g_*^{1/2}$, since only two of them are independent. However, it is more elucidating to perform the analysis with $g_*^{1/2}$ and h, since the solution Y_0 directly depends on the former and indirectly on the latter.

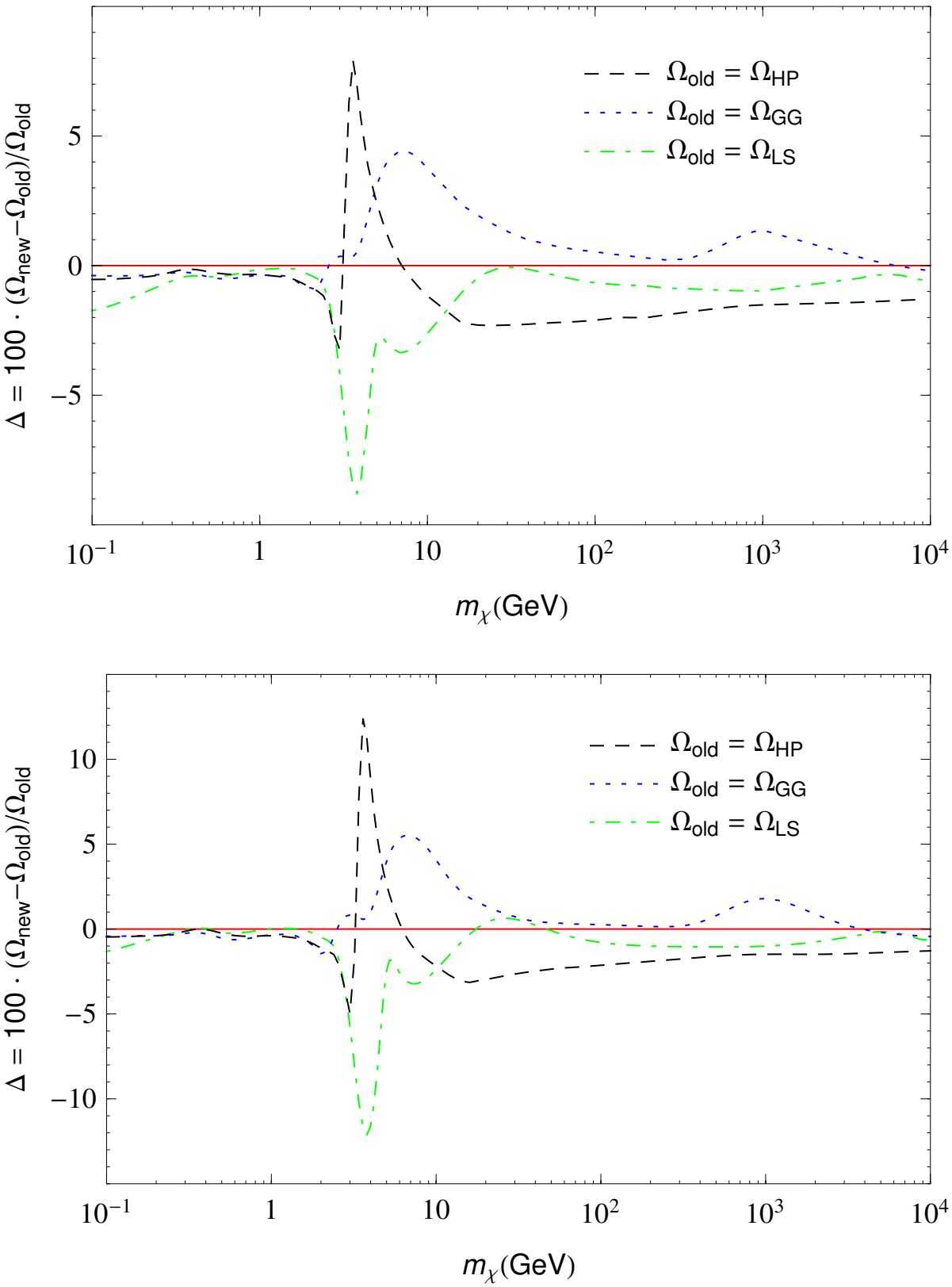

Figure 5.4: The relative difference between the predicted relic density of a Majorana WIMP between our calculation and a calculation using the same older results for the functions h and $g_*^{1/2}$ shown in fig. 5.3, as a function of the WIMP mass. The upper frame is for constant $\langle\sigma v\rangle$, chosen such that our prediction for $\Omega_\chi h^2 = 0.1193$, while the lower frame is for a pure P-ave annihilation, with $\langle\sigma v\rangle = 1.2 \cdot 10^{-24}\mathrm{cm}^3\mathrm{s}^{-1} \cdot T/m_\chi$. These results are almost independent of the numerical size of the annihilation cross section.

temperatures above T_c. Eq. (5.1.7) indicates that this should lead to a smaller predicted relic density, which is confirmed by figure 5.4. Since $g_*^{1/2}$ is overestimated for an extended range of temperatures, the effect on the relic density is about the same for S- and P-wave annihilation, amounting to about 5% near the peak of the ratio shown in figure 5.4. The second, much lower peak near $m_\chi = 1\,\mathrm{TeV}$ is probably due to lack of knowledge of the top mass at the time when [59] was written.

The spike in $g_*^{1/2}$ predicted in `micrOMEGAs` treatment of the results of [106] gives prominent spikes in the ratios shown in figure 5.4. These spikes are numerical artefacts that result from the smoothing procedure in `micrOMEGAs`. As argued in ref. [106], a true δ function spike in $g_*^{1/2}$ should not affect the numerical solution of the Boltzmann equation, which necessarily entails some discretization. The probability that the program then has to evaluate the right hand side of the Boltzmann equation at the precise value of x where the δ function diverges is zero. We nevertheless show results including the spike, since it results from the "standard treatment" encoded in `micrOMEGAs`. Outside the mass range affected by this spike, the results from [106] predict a slightly too large relic density, consistent with our observation that it predicts smaller values of $g_*^{1/2}$ and h than our treatment does. Note that for fixed $g_*^{1/2}$, reducing h will (slightly) increase x_f, leading to an increase of the predicted relic density. A decrease of h therefore goes into the same direction as a decrease of $g_*^{1/2}$. However, the fact that the relative difference between our calculation and the prediction based on ref. [106] is almost the same in both frames of figure 5.4 at large WIMP masses shows that the main effect still comes from the change of $g_*^{1/2}$.

We saw in fig. (5.3) that the prediction for $g_*^{1/2}$ from [94] lies below our prediction, except for a very narrow range of temperatures around T_c. As a result, for pure S-wave annihilation, the prediction for the relic density based on the treatment of [94] lies above our prediction for all WIMP masses larger than 2 GeV. We argued above that the relevant range of temperatures is (even) smaller for pure P-wave annihilation. This explains why the blue curve in the lower frame of fig. 5.4 goes slightly above 1 for $m_\chi \simeq 25\,\mathrm{GeV}$. Note also that the predictions using our treatment agrees with the prediciton using [94] to better than 1% for all WIMP masses, except in the range between 2 and 20 GeV where the difference reaches 9 (12) % for pure S- (P-) wave annihilation.

In order to put these results into perspective, it should be noted that the lattice QCD predictions for the energy and entropy densities listed in table 1 of [92], on which our treatment is based, still have significant uncertainties, which decrease from about to 14% at $T = 130\,\mathrm{MeV}$ to about 3% at $T = 400\,\mathrm{MeV}$. The corresponding uncertainty in the relic density is up to 2.5% for $2\,\mathrm{GeV} \leq m_\chi \leq 20\,\mathrm{GeV}$. Finally, we note that treating the charm quark as a free particle would increase the predicted relic density by about 2.2% for $m_\chi \simeq 30\,\mathrm{GeV}$.

We may comment that the results shown in the upper frame of fig. 5.4 do not depend greatly on the WIMP annihilation cross section as long as the relic density comes out roughly correctly. For the lower frame, the dependence of $\langle\sigma v\rangle$ on the temperature has implications on the final $\Omega_\chi h^2$. Also, eq. (5.1.7) shows that the thermodynamic effects

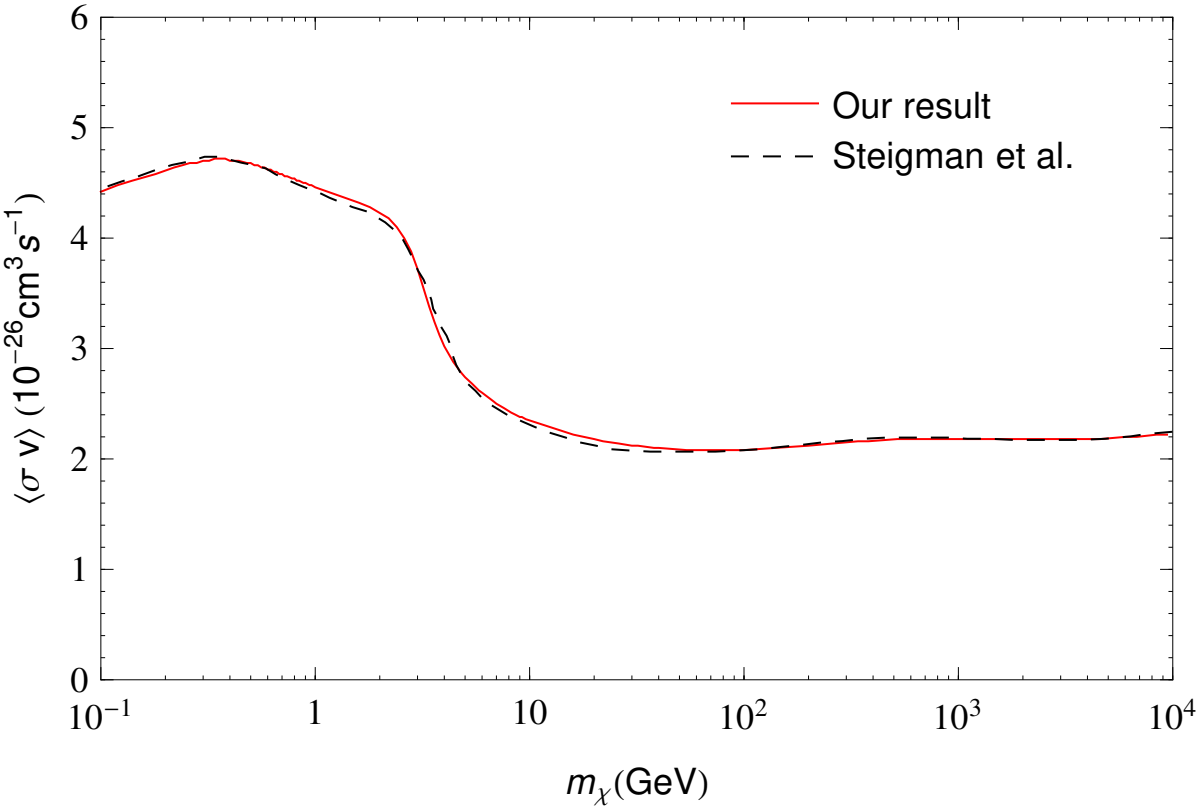

Figure 5.5: The value of $\langle\sigma v\rangle$, assumed to be completely independent of temperature, required to obtain a thermal relic density $\Omega_\chi h^2 = 0.1193$ within standard cosmology, as a function of WIMP mass (red solid line). Also, the result of ref. [114] scaled to $\Omega_\chi h^2 = 0.1193$ is shown (black dashed line).

enter primarily through $g_*^{1/2}(x_f)$, and x_f depends on the annihilation cross section only logarithmically.

However, the exact value of the annihilation cross section that reproduces the correct relic density, now (within the standard ΛCDM cosmology) constrained to be $\Omega_\chi h^2 = 0.1193 \pm 0.0014$ [45], does depend on $g_*^{1/2}(T_f)$, and less dramatically on $h\,(T_f)$. Precise knowledge of the cross section is important to constrain the free parameters of models of thermal WIMPs. Moreover, as we will see in more detail in sec. 5.1.4, indirect DM searches now begin to probe annihilation cross sections close to the required value of $\langle\sigma v\rangle$, if the latter is (approximately) independent of the temperature.

In fig. 5.5 we show the required value of $\langle\sigma v\rangle$, assumed to be independent of the temperature, for a Majorana fermion, obtained from our refined calculation of $g_*^{1/2}$ and h. This updates the results of ref. [114], which assumed $\Omega_\chi h^2 = 0.11$ and used [94] to compute $g_*^{1/2}$ and h. For comparison, we also show the result of ref. [114], scaled by $0.11/0.1193$ in order to (roughly) account for the different assumptions on $\Omega_\chi h^2$.

We see that for $10\,\mathrm{GeV} < m_\chi < 10\,\mathrm{TeV}$, the required value of $\langle\sigma v\rangle$ is in fact closer to $2 \cdot 10^{-26}\,\mathrm{cm}^3\mathrm{s}^{-1}$ than to the often cited value $3 \cdot 10^{-26}\,\mathrm{cm}^3\mathrm{s}^{-1}$. The near constancy of the required value over such a large range of WIMP masses results from an *accidental*

cancellation of two effects. This can again be understood from the approximate analytical solution (5.1.7) of the Boltzmann equation. On one hand, increasing m_χ increases x_f, which *increases* the relic density. Since x_f depends only logarithmically on m_χ, the freezout temperature $T_f = m_\chi/x_f$ still increases as m_χ is increased. As shown in the lower frame of fig. (5.3), this increases $g_*^{1/2}(T_f)$, which in turn *reduces* the relic density. For $m_\chi > 10$ TeV, all SM particles are essentially relativistic at T_f, i.e. $g_*^{1/2}$ becomes independent of T, reaching its asymptotic value of 106.75. For these very large masses, the required value of $\langle\sigma v\rangle$ would thus increase logarithmically with m_χ, in order to cancel the effect of the increase of x_f. However, since by dimensional analysis and unitary arguments $\langle\sigma v\rangle \propto 1/m_\chi^2$, it is very difficult to find scenarios with sufficiently large $\langle\sigma v\rangle$ for $m_\chi > 10\,\text{TeV}$.

On the other hand, for WIMP masses below 10 GeV, the rapid decrease of $g_*^{1/2}(T_f)$ with decreasing T_f shown in fig. 5.3 (lower frame) requires a rather rapid increase of $\langle\sigma v\rangle$, to a peak value of about $4.5 \cdot 10^{-26}\,\text{cm}^3\text{s}^{-1}$. Finally, for $m_\chi < 0.35\,\text{GeV}$, $g_*^{1/2}(T_f)$ becomes approximately constant again, with electrons, positrons, neutrinos, and photons contributing so that $g_*^{1/2} \simeq 3.29$. Since x_f keeps decreasing with decreasing m_χ, keeping the relic density constant requires that $\langle\sigma v\rangle$ also decreases logarithmically with decreasing WIMP mass for these very light WIMPs.

For WIMP masses of a few GeV, the rescaled result of ref. [114] gives a somewhat larger value of $\langle\sigma v\rangle$ than our calculation. This agrees with the observation that the calculation of $g(T)$ and $h(T)$ performed in ref. [94] leads to a larger relic density than our treatment, as illustrated in fig. 5.5.[5]

5.1.4 Experimental constraints on $\langle\sigma v\rangle$

In this section, we will compare experimental constraints from indirect WIMP searches and from analyses of the cosmic microwave background (CMB) with our prediction for $\langle\sigma v\rangle$ shown in fig. 5.5. This simultaneous comparison of $\langle\sigma v\rangle$ with these two types of constraint only makes sense if $\langle\sigma v\rangle$ is largely independent of the temperature. In fact, since the CMB decoupled much later than WIMPs did, and hence also at a much lower temperature ($\sim 0.3\,\text{eV}$ rather than $\sim m_\chi/20$), while the WIMPs in galaxies now have an average kinetic energy of $\sim 10^{-6} m_\chi$. If $\langle\sigma v\rangle \propto T$, as in pure P-wave annihilation, or for even stronger T-dependence, the bounds on $\langle\sigma v\rangle$ from the CMB and from indirect WIMP searches are still several orders of magnitude above the value required to obtain the correct relic density.

Currently the strongest and most robust upper bounds on $\langle\sigma v\rangle$ from indirect WIMP searches come from searches for hard γ rays (from dwaf galaxies) by the FermiLAT collaboration. The strongest WIMP signal is expected from near the center of our own galaxy. Unfortunately this region also hosts several backgrounds, both in form of point sources and in form of extended emission. It has been claimed that there is evidence for

[5] The comparison in figure 5.5 is less accurate than that in figure 5.4, since it relies on reading off numerical results of ref. [114], and since the relation $\Omega_\chi h^2 \propto 1/\langle\sigma v\rangle$ assumed in the rescaling is not exact.

an additional component in the GeV γ flux from near the galactic center which can be explained through WIMP annihilation [115–118], but other interpretations of this additional component exist [119–121]. We also note that FermiLAT collaboration itself has not published any analysis of their data on the galactic center.

In this paper we therefore focus on FermiLAT observations of nearby galaxies [78–81]. In contrast to big galaxies like our own, the mass density of dwarf galaxies should be dominated by dark matter even in the central region, yielding a much better signal-to-background ratio for indirect WIMP signals. No such signal has been seen. Our analysis is based on the very recent 6-year "Pass 8" analysis [81].

The results are shown in figure 5.6. We see that the upper bound on $\langle\sigma v\rangle$ is strongest if WIMPs predominantly annihilate into $u\bar{u}$ final states, but the bound for WIMP annihilation into $b\bar{b}$ is only slightly weaker. For the $\tau^+\tau^-$ final state the upper bound on the cross section is similar for WIMP masses below 40 GeV, but is somewhat weaker for heavier WIMPs; hadronic final states have higher multiplicity, and hence higher γ flux per WIMP annihilation, for larger WIMP masses, whereas for the $\tau^+\tau^-$ final state the photon multiplicity is essentially independent of the WIMP mass. These constraints exclude WIMPs with mass $m_\chi \leq 70$ to 100GeV annihilating into hadrons or τ leptons with temperature independent $\langle\sigma v\rangle$.

To WIMP annihilation into e^+e^-corresponds an upper bound on $\langle\sigma v\rangle$ (not shown) which is worse than that for WIMP annihilations into $\tau^+\tau^-$ [81], excluding WIMPs with mass $m_\chi \leq 15\,\mathrm{GeV}$ annihilating into e^+e^- pairs for the value of $\langle\sigma v\rangle$ shown in fig. 5.6.

WIMP annihilation also affects the CMB, as described in sec. 4.2. In figure 5.6 we show the bound on the WIMP annihilation cross section into e^+e^- pairs that results from an analysis [84] of data from the WMAP and ACT collaborations. It excludes a thermal WIMP with $m_\chi \leq 12\,\mathrm{GeV}$.

PLANCK data will lead to considerable stronger constraints [45, 122]. Unfortunately these papers only cite upper bounds on the product of the WIMP annihilation cross setion and an efficiency factor f_{eff} with whih energy of the WIMP annhilation products is absorbed in the thermal plasma. Using results from ref. [123], we estimate that the latest PLANCK data exclude WIMPs with $m < 40\,\mathrm{GeV}$ annihilating into e^+e^-pairs with temperature independent cross section; see also the recent analysis [124], which obtians the limite $m < 50\,\mathrm{GeV}$. The difference follows from the fact that we are using $f \simeq 0.8$ following [123], whereas [124] assumes $f = 1$.

Since the efficiency factor should be similar for other final states, the CMB constraint should also vary accordingly (with the factor f) for final channels such as $\mu^+\mu^-$ or $q\bar{q}$. The current CMB constraint is thus weaker than the bounds derived from the most recent FermiLAT data if WIMPs mostly annihilate into $q\bar{q}$ or $\tau^+\tau^-$ final states, but is stronger for WIMPs annihilating predominantly into e^+e^-. However, one should keep in mind that the CMB constraint is less direct. Is is conceivable that additional non-standard ingredients to the CMB fit — e.g., the presence of sterile neutrinos, a significant running of the spectral index of inflation, and/or large contribution from tensor modes — can (partly) compensate the distortions caused by early WIMP annihilation, thereby

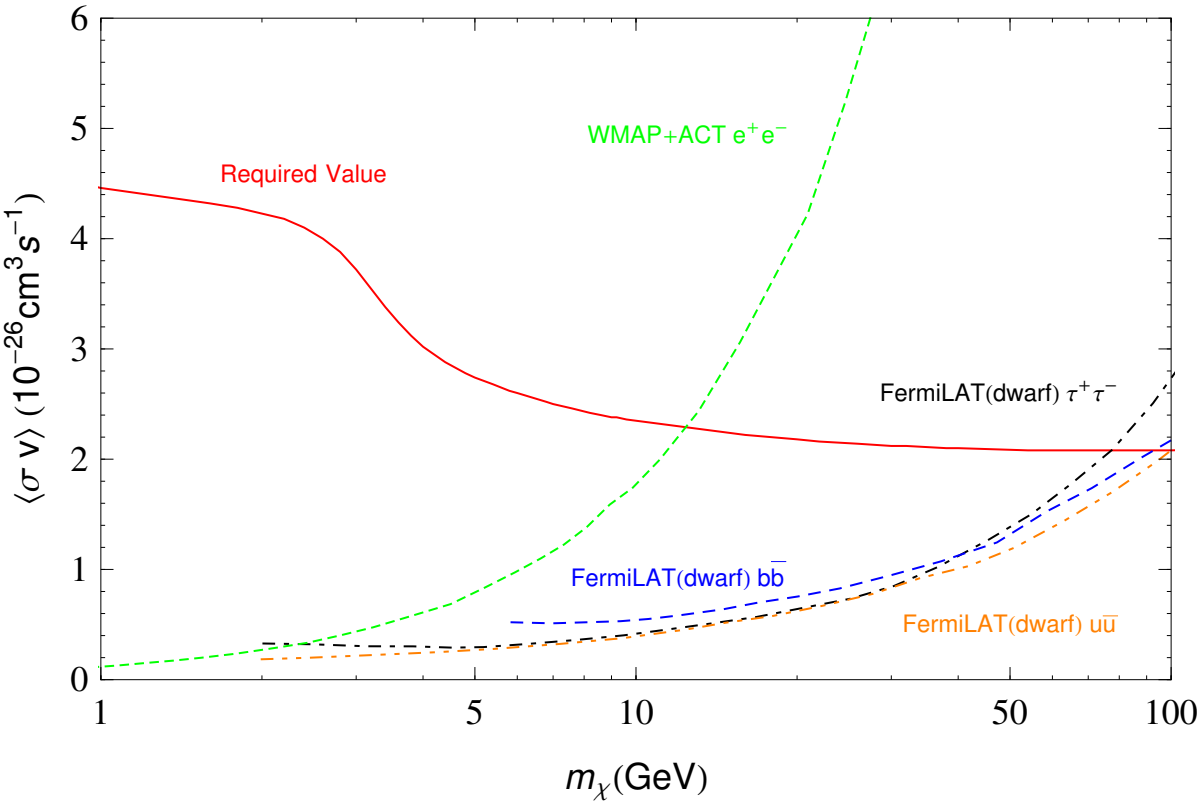

Figure 5.6: The result of fig. 5.5 is compared with several observational upper bounds on $\langle\sigma v\rangle$, which is assumed to be independent of temperature. The orange, blue and black curves follow from the FermiLAT upper bound [81] on the γ flux from dwarf galaxies, for different dominant WIMP annihilation channel ($u\bar{u}$, $b\bar{b}$ or $\tau^+\tau^-$), whereas the red curve results from an upper bound on spectral distortions of the CMB [84], assuming WIMP annihilation into e^+e^- pairs.

weakening the constrain on $\langle\sigma v\rangle$. On the other hand, the constraint derived from the observation of dwarf galaxies depends on the assumed dark matter distribution [78]. In any case, it is encouraging that recent astrophysical and cosmological observations begin to probe relatively light thermal WIMPs with temperature independent annihilation cross section.

5.2 Fermionic dark matter in a SM extension

In the last sections, much has been written about relic production, including detailed aspects about deconfinement. We obtained the behaviour of functions $h\,(T)$ and $g_*^{1/2}\,(T)$, essential for solutions of the Boltzmann equation, as well as a required $\langle\sigma v\rangle$ (for the S-wave case) in order to obtain the observed mean value $\Omega_\chi h^2 = 0.1193$. The treatment for the χ relic has been general, only assuming the χ particle is a Majorana particle. In this section, we take another viewpont and detail a specific case [86] in which a fermionic dark matter can be obtained, also majorana-like. Though this work also dealt with the neutrino mass generation in the $B-L$ SM extension, we will focus on dark matter generation. First we

Fermion	I_3	Y'	$B-L$	Scalar	I_3	Y'	$B-L$
ν_{eL}, e_L	$\pm 1/2$	0	-1	$H^{+,0}$	$\pm 1/2$	1	0
e_R	0	-1	-1	$\Phi^{0,-}$	$\pm 1/2$	-4	3
u_L, d_L	$\pm 1/2$	0	$1/3$	ϕ_1	0	-8	8
u_R	0	1	$1/3$	ϕ_2	0	10	-10
d_R	0	-1	$1/3$	ϕ_3	0	1	-1
n_{R1}, n_{R2}	0	4	-4	ϕ_X	0	3	-3
n_{R3}	0	-5	5				

Table 5.2: Quantum number assignment for the fields in the model. I_3, Y' and $B-L$ are the quantum numbers under the symmetry groups $\mathrm{SU}(2)_L$, $\mathrm{U}(1)_{Y'}$ and $\mathrm{U}(1)_{B-L}$ respectively.

describe the model, more specifically the gauge group and particles quantum numbers as well as the scalar and Yukawa lagrangians.

5.2.1 The model

We consider an extension of the SM based on the gauge symmetry $\mathrm{SU}(2)_L \otimes \mathrm{U}(1)_{Y'} \otimes \mathrm{U}(1)_{B-L}$ where B and L are respectively the usual baryonic and leptonic numbers and Y' is a new charge different from the hypercharge Y of the SM. The values of Y' are chosen in order to obtain the hypercharge Y through the relation $Y = [Y' + (B-L)]$, after the first spontaneous symmetry breaking. The fields of this model with their respective charges are shown in table 5.2. This model is a simplified variation of the one introduced in refs. [125, 126]. Specifically, we have removed one of the extra doublets of scalars considered there. As we will show below, this allows an almost automatic $\mathbb{Z}_2$symmetry that stabilizes the DM candidate, n_{R3}. The remaining scalar fields are enough to give mass to the neutrinos at tree level. It is also important to note that there is an exotic charge assignment for the $B-L$ charges where $(B-L)_{n_{R1},n_{R2}} = -4$ and $(B-L)_{n_{R3}} = 5$, different from the usual one where $(B-L)_{n_{Ri}} = 1$ with $i = 1, 2, 3$.

With the field content in table 5.2, we can write respectively the most general renormalizable Yukawa Lagrangian and scalar potential respecting gauge invariance as follows,

$$\begin{aligned} -\mathcal{L}_{\mathrm{Y}} \;=\; & Y_i^{(l)} \overline{L}_{Li} e_{Ri} H + Y_{ij}^{(d)} \overline{Q}_{Li} d_{Rj} H + Y_{ij}^{(u)} \overline{Q}_{Li} u_{Rj} \widetilde{H} + \mathcal{D}_{im} \overline{L}_{Li} n_{Rm} \Phi \\ & + \frac{1}{2} \mathcal{M}_{mn} \overline{(n_{Rm})^c} n_{Rn} \phi_1 + \frac{1}{2} \mathcal{M}_{33} \overline{(n_{R3})^c} n_{R3} \phi_2 + \frac{1}{2} \mathcal{M}_{m3} \overline{(n_{Rm})^c} n_{R3} \phi_3 \\ & + \text{H.c.}, \end{aligned} \tag{5.2.1}$$

and

$$\begin{aligned} V_{B-L} &= -\mu_H^2 H^\dagger H + \lambda_H \left|H^\dagger H\right|^2 - \mu_\Phi^2 \Phi^\dagger \Phi + \lambda_\Phi \left|\Phi^\dagger \Phi\right|^2 - \mu_\alpha^2 \left|\phi_\alpha\right|^2 + \lambda_\alpha \left|\phi_\alpha^* \phi_\alpha\right|^2 \\ &\quad + \kappa_{H\Phi} \left|H\right|^2 \left|\Phi\right|^2 + \kappa'_{H\Phi} (H^\dagger \Phi)(\Phi^\dagger H) + \kappa_{H\alpha} \left|H\right|^2 \left|\phi_\alpha\right|^2 + \kappa_{\Phi\alpha} \left|\Phi\right|^2 \left|\phi_\alpha\right|^2 \\ &\quad + \kappa_{\alpha\beta} (\phi_\alpha^* \phi_\alpha)(\phi_\beta^* \phi_\beta) + \left[\kappa_{123} \phi_1 \phi_2 (\phi_3^*)^2 - i \kappa_{H\Phi X} \Phi^T \tau_2 H \phi_X + \kappa_{123X} (\phi_X^* \phi_1)(\phi_2 \phi_3)\right. \\ &\quad \left. + \kappa'_{3X} (\phi_X^* \phi_3^3) + \text{H.c.}\right], \end{aligned} \tag{5.2.2}$$

where $i, j = 1, 2, 3$ are lepton/quark family numbers; $m, n = 1, 2$; $\widetilde{H} = i\tau_2 H^*$ (τ_2 is the Pauli matrix), and $\alpha, \beta = 1, 2, 3, X$ with $\alpha \neq \beta$ for the $\kappa_{\alpha\beta}(\phi_\alpha^* \phi_\alpha)(\phi_\beta^* \phi_\beta)$ terms. Also, we have omitted summation symbols over repeated indices.

Before we go further, two important remarks are in order. Firstly, from eqs. (5.2.1) and (5.2.2) we see that apart from the $\frac{1}{2}\mathcal{M}_{m3}\overline{(n_{Rm})^c} n_{R3} \phi_3 + \text{H.c.}$ terms, the Lagrangian is invariant under a $\mathbb{Z}_2$ symmetry acting in a non-trivial way on the n_{R3} field, i.e. $\mathbb{Z}_2(n_{R3}) = -n_{R3}$ (the rest of fields being invariant under this symmetry). We will consider the case of this $\mathbb{Z}_2$ symmetry throughout this work. Hence, the n_{R3} fermionic field will be the DM candidate. Secondly, from eq. (5.2.1) we see that quarks and charged leptons obtain masses just from the H vacuum expectation value, $\langle H^0 \rangle \equiv v_H$. Therefore, the H interactions with quarks and charged leptons are diagonalized by the same matrices as the corresponding mass matrices. In this case the neutral interactions are diagonal in flavor and there is no flavor-changing neutral current in the quark and charged lepton sector. This feature remains after the symmetry basis is changed to mass basis [127, 128].

However, lepton flavor violation (LFV) processes coming from the terms proportional to $\mathcal{D}_{im}$ can occur at one loop. We find [86] that for both normal and inverted neutrino mass hierarchies, numerical values for all six $\mathcal{D}_{im}$ can be found, which are consistent with the bounds on the LFV processes: $\text{Br}(\mu \to e + \gamma) < 5.7 \times 10^{-13}$ and $\text{Br}(\tau \to \mu + \gamma) < 4.4 \times 10^{-8}$ [97]. We do not discuss this topic in detail here, since we are interested in dark matter production.

5.2.2 Scalar sector

Within the general case, this model has a rich scalar spectrum and its vacuum structure can take several configurations. However, we are going to make some simplifying and reasonable assumptions that allow us in most cases to obtain analytical formulas in both the neutrino and the dark matter sectors. We will discuss systematically our assumptions throughout this paper.

Firstly, as result of the absence of one of the extra doublets and of writing only the renormalizable terms in the scalar potential, the model here considered has a physical Nambu-Goldstone (NG) boson J in its scalar spectrum. This is a general conclusion and does not depend on any particular choice of the parameter set. Once the neutral scalars develop non-vanishing vacuum expectation values (VEVs), we find that J can be written

as

$$
\begin{aligned}
J \;=\; & \frac{1}{N_J}\Big[-9\sqrt{2}v_H v_\phi^3\epsilon^2\,\mathrm{Im}\,H^0 - 9\sqrt{2}v_H^2 v_\phi^2\epsilon\,\mathrm{Im}\,\Phi^0 \\
& + \frac{1}{\sqrt{2}}v_\phi^2\left(10v_H^2 + \left(3v_H^2 + 10v_\phi^2\right)\epsilon^2\right)\,\mathrm{Im}\,\phi_1 + \frac{v_\phi^2\left(2v_H^2 - \left(3v_H^2 - 2v_\phi^2\right)\epsilon^2\right)}{\sqrt{2}}\,\mathrm{Im}\,\phi_2 \\
& + 3\sqrt{2}v_\phi^2\left(v_H^2 + v_\phi^2\epsilon^2\right)\,\mathrm{Im}\,\phi_3 + 9\sqrt{2}v_\phi^2\left(v_H^2 + v_\phi^2\epsilon^2\right)\,\mathrm{Im}\,\phi_X\Big], \qquad (5.2.3)
\end{aligned}
$$

where $N_J \equiv v_\phi^2\sqrt{\left(4v_H^2 + \left(3v_H^2 + 4v_\phi^2\right)\epsilon^2\right)\left(58v_H^2 + \left(3v_H^2 + 58v_\phi^2\right)\epsilon^2\right)}$ and $\epsilon \equiv v_\Phi/v_\phi$. We also have defined the VEVs as $\langle\phi_i\rangle \equiv v_{\phi_i}$ with $i = H,\, \Phi,\, \phi_1,\, \phi_2,\, \phi_3,\, \phi_X$ and set $v_{\phi_1} = v_{\phi_2} = v_{\phi_3} = v_{\phi_X} \equiv v_\phi$ for simplicity. The parameter ϵ is chosen $\ll 1$ as we will show below. We have also used the usual shifting $\varphi^0 = \frac{1}{\sqrt{2}}\left(v_\varphi + \mathrm{Re}\,\varphi + i\,\mathrm{Im}\,\varphi\right)$ for the scalar fields (the superscript "0" means we are taking the neutral part of the field).

The presence of J in the physical spectrum is due to an extra symmetry in the scalar potential in eq. (5.2.2). In other words, the scalar potential actually has a larger global $\mathrm{SU}(2)_L \otimes \mathrm{U}(1)_{Y'} \otimes \mathrm{U}(1)_{B-L} \otimes \mathrm{U}(1)_J$ symmetry. The symmetry group $\mathrm{U}(1)_J$ acts on the scalar fields H, Φ, ϕ_1, ϕ_2, ϕ_3, ϕ_X with charges $-\frac{18}{23}$, $-\frac{18}{23}$, 1, $\frac{1}{23}$, $\frac{12}{23}$, $\frac{36}{23}$, respectively. We have normalized the charges in order to set the ϕ_1 charge equal to 1. Also, note $\mathrm{U}(1)_J$ is independent on the $\mathrm{U}(1)_{Y'}$ and $\mathrm{U}(1)_{B-L}$ symmetry groups, a necessary condition to consider it as an actual extra symmetry. Furthermore, $\mathrm{U}(1)_J$ can be extended nontrivially to the total Lagrangian acting on the fermions Q_L, u_R, d_R, L_L, e_R, n_{Rm}, n_{R3} with charges $0, -\frac{18}{23}$, $\frac{18}{23}$, $-\frac{59}{23}$, $-\frac{1}{2}$, $-\frac{1}{2}$, $-\frac{1}{46}$, respectively. Therefore, J is a true NG boson with mass equal to zero at all orders in perturbation theory. Gravitational effects can break this symmetry, and thus give mass to the NG boson [129–133]. However, we are not going to comment in detail on the latter case.

The major challenge to models with a NG boson comes from the energy loss in stars through the process $\gamma + e^- \to e^- + J$. This process is used to put limits on the $\bar{e}eJ$ coupling, $g_{\bar{e}eJ}$, and it is found that it must be $g_{\bar{e}eJ} \leq 10^{-10}$ for the Sun, and $g_{\bar{e}eJ} \leq 10^{-12}$ for the red-giant stars [134, 135]. In our case, $g_{\bar{e}eJ} = \frac{Y_e^{(l)}}{\sqrt{2}}\frac{9\sqrt{2}v_H v_\phi^3}{N_J}\epsilon^2 = \frac{m_e}{v_H}\frac{9\sqrt{2}v_H v_\phi^3}{N_J}\epsilon^2$ where $Y_e^{(l)}$ and m_e are the electron Yukawa coupling to the H scalar and electron mass, respectively. Since $\epsilon = v_\Phi/v_\phi$, $v_{\mathrm{SM}} = \sqrt{v_H^2 + v_\Phi^2}$ and $v_H \simeq v_{\mathrm{SM}}$ (the $\mathrm{Re}\,H^0$ is the only field giving mass to the top quark at tree level), we have that $\epsilon \ll 1$. Thus, expanding $g_{\bar{e}eJ}$ in powers of ϵ, it is straightforward to see that $g_{\bar{e}eJ} \simeq \frac{9m_e v_\phi}{2\sqrt{29}v_H^2}\epsilon^2 + \mathcal{O}(\epsilon^4)$. Choosing $v_\phi = 1$ TeV and $v_H \simeq v_{\mathrm{SM}} = 246$ GeV we can notice that $\epsilon \lesssim 3.8 \times 10^{-4}$satisfies the limit coming from red-giant stars analysis.

The charged sector can also be found analytically. Besides the charged Nambu-Goldstone eaten by the $W^\pm$ gauge boson, the model has one charged scalar $C^\pm$, which can be written as $C^\pm = \frac{1}{\sqrt{v_H^2 + v_\phi^2\epsilon^2}}\left(v_\phi\epsilon\,H^\pm + v_H\,\Phi^\pm\right)$, with squared mass given by $m_{C^\pm}^2 = \frac{\kappa_{H\Phi X}v_H}{\sqrt{2}}\frac{1}{\epsilon} + \frac{\kappa'_{H\Phi}v_H^2}{2} + \frac{\kappa_{H\Phi X}v_\phi^2}{\sqrt{2}v_H}\epsilon + \frac{1}{2}\kappa'_{H\Phi}v_\phi^2\epsilon^2$. Note that when $\epsilon \to 0$, it yields $m_{C^\pm} \to \infty$. However, when this happens, the minimization conditions in Appendix A require that $\kappa_{H\Phi X} \propto \epsilon$. Hence, as one can see from $C^\pm$ mass expression, $m_{C^\pm}$ remains finite in the end.order to find

the rest of the mass eigenvalues and eigenstates of the scalar potential (the $CP-$even, $CP-$odd scalars), in general we numerically proceed choosing the set of the parameters to satisfy simultaneously the minimization conditions given in eqs. (A.1-A.6), the positivity of the squared masses, and the lower boundedness of the scalar potential. All these constraints are always checked numerically. Furthermore, we wish to restrict ourselves to a relevant set of parameters that allows us to study the dark matter properties in some interesting cases. For that, we establish initial assumptions and results:

(i) For the sake of simplicity: $v_{\phi_1} = v_{\phi_2} = v_{\phi_3} = v_{\phi_X} \equiv v_\phi$ (we have already used this in eqs. (5.2.3) and in the $C^\pm$ charged scalar), $\kappa_{H\Phi} = \kappa'_{H\Phi} = \kappa_{H1} = \kappa_{H3} = \kappa_{HX} = \kappa_{\Phi 1} = \kappa_{\Phi 2} = \kappa_{\Phi 3} = \kappa_{\Phi X} = \kappa_{12} = \kappa_{13} = \kappa_{1X} = \kappa_{23} = \kappa_{2X} = \kappa_{3X} = 0$ and $\kappa_{123X} = \kappa'_{3X} = \kappa_{123}$.

(ii) In order to have the heaviest $CP-$even scalars with similar masses, we choose: $\lambda_1 = \lambda_2 = \lambda_3 = \lambda_X \equiv \lambda_\phi$.

(iii) Due to the stability of the minima, we obtain: $\kappa_{H\Phi X} = v_\phi \epsilon$ (see eq. (A.2)) and $\mu_H^2 = \lambda_H v_H + \frac{\kappa_{H2} v_\phi^2}{2} - \frac{v_\phi^3}{\sqrt{2} v_H}\epsilon^2$, $\mu_\Phi^2 = -\frac{v_H v_\phi}{\sqrt{2}} + \lambda_\Phi v_\phi^2 \epsilon^2$, $\mu_1^2 = (\kappa_{123} + \lambda_\phi) v_\phi^2$, $\mu_2^2 = \frac{\kappa_{H2} v_H^2}{2} + (\kappa_{123} + \lambda_\phi) v_\phi^2$, $\mu_3^2 = (3\kappa_{123} + \lambda_\phi) v_\phi^2$, and $\mu_X^2 = (\kappa_{123} + \lambda_\phi) v_\phi^2 - \frac{v_H v_\phi}{\sqrt{2}}\epsilon^2$. The rest of parameters will be chosen when required.

In general, the squared mass matrices of the $CP-$odd scalars ($M^2_{CP-\text{odd}}$) and the $CP-$even scalars ($M^2_{CP-\text{even}}$) can be written in powers of ϵ up to ϵ^2, i.e. $M_i^2 = M_{0,i}^2 + \epsilon M_{1,i}^2 + \epsilon^2 M_{2,i}^2$ with $i = CP-\text{odd}, CP-\text{even}$. Despite the smallness of ϵ and the assumptions made above, it is a hard task to obtain exact analytical expressions for the mass eigenvalues and mass eigenstates of these matrices. These can be found perturbatively in powers of ϵ. In this section we just provide the leading-order expression of the scalar masses because these yield a good picture of their exact behavior.

In the $CP-$odd sector the model has three scalars, I_1, I_2, I_3, besides the NG boson J and the two NG bosons eaten by the Z_1 (it is assumed that Z_1 is the gauge boson with mass equal to the Z boson in the SM) and Z_2 boson. Their masses are given by $m_{I_1} = \frac{\sqrt{v_H v_\phi}}{\sqrt[4]{2}}$, $m_{I_2} = \sqrt{5 - \sqrt{7}}\sqrt{-\kappa_{123}} v_\phi$, $m_{I_3} = \sqrt{5 + \sqrt{7}}\sqrt{-\kappa_{123}} v_\phi$. From the previous expressions we see that we have to assume $\kappa_{123} < 0$ in order to have all masses belonging to reals. It is also straightforward to see that $I_1 = \text{Im}\,\Phi^0 + \mathcal{O}(\epsilon)$. Additionally, we find that I_2 and I_3 are, at ϵ order, a linear combination of the $\text{Im}\,\phi_i$'s with $i = 1, 2, 3, X$. The $CP-$even sector is more complicated even in the leading order. In this sector the model has six different eigenstates, R_i's, with masses given by: $m_{R_1} = \sqrt{2\lambda_H} v_H$, $m_{R_2} = \frac{\sqrt{v_H v_\phi}}{\sqrt[4]{2}}$, $m_{R_3} = \sqrt{2\lambda_\phi - 3.58\,|\kappa_{123}|} v_\phi$, $m_{R_4} = \sqrt{2\lambda_\phi + 1.15\,|\kappa_{123}|} v_\phi$, $m_{R_5} = \sqrt{2\,(\lambda_\phi + |\kappa_{123}|)} v_\phi$, $m_{R_6} = \sqrt{2\lambda_\phi + 2.42\,|\kappa_{123}|} v_\phi$. R_1 (which is $\text{Re}\,H^0 + \mathcal{O}(\epsilon)$) is the scalar that plays the role of the Higgs scalar boson in this model, since it couples at tree level to all fermions, giving mass to them when it gains a VEV, v_H. Thus, we set its mass equal to 125 GeV. We find that $\lambda_H \simeq 0.13 - 0.14$ gives the correct value for the Higgs mass; R_2 is $\text{Re}\,\Phi^0 + \mathcal{O}(\epsilon)$; and the remaining fields are combinations of the $\text{Re}\,\phi_i$'s with $i = 1, 2, 3, X$. Note that the latter five $CP-$even scalars do not yield precise mass values as R_1. However, we have to

choose the parameters in the scalar potential such that all m_{R_i} masses are larger than the Z_1 boson mass ($m_{Z_1}^2 \approx \frac{g^2\left(v_H^2+v_\Phi^2\right)}{4\cos^2\theta_W} = \frac{m_W^2}{\cos^2\theta_W}$) due to the Z_1 invisible decay width. In other words, if some of m_{R_i} were $< M_{Z_1}$ then the Z_1 boson could decay through the process $Z_1 \to R_i + J \to J + J + J$, which would contribute to the Z_1 boson decay width as half of the decay $Z_1 \to \bar{\nu}\nu$ [136]. According to the experimental data there is no room for such an extra contribution [97].

All expressions above for masses and eigenstates are very useful to have a general undertanding of the scalar spectrum. However, it is necessary to work with more precision when calculations of the DM sector are involved. Thus, from here on, we always work numerically to diagonalize the squared-mass matrices for both the $CP-$odd and the $CP-$even scalars.

Finally, a further comment regarding the J presence is necessary. Since J is massless, it contributes to the Universe radiation energy density of today which is usually parameterized by the effective neutrino number N_{eff}. This parameter specifies the energy density of relativistic species in terms of the neutrino temperature. PLANCK together with WMAP9 polarization data, high-l experiments and the BAO data (Planck + WP + highL + BAO) gives $N_{\text{eff}} = 3.30^{+0.54}_{-0.51}$ [45]. J in our model decouples at $T_f \simeq 14$ GeV, which is far above the neutrino decoupling temperature, therefore its contribution to N_{eff} is given by $\Delta N_{\text{eff}} = \frac{4}{7}\left(\frac{h_\gamma^{\text{BBN}}}{h_\gamma^{\text{dec}}}\right)^{4/3} \simeq \frac{4}{7}\left(\frac{10.75}{86}\right)^{4/3} \simeq 0.036$, where h_γ^{BBN} and h_γ^{dec} are the entropy degrees of freedom of the plasma at the time of big bang nucleosynthesis (BBN) and of the J decoupling. Notice that this result is in agreement with the current bound on N_{eff}. For a similar treatment, see ref. [137].

5.2.3 Dark matter

As previously mentioned, this model has an almost automatic $\mathbb{Z}_2$ symmetry acting on n_{R3}, i.e. $\mathbb{Z}_2\left(n_{R3}\right) = -n_{R3}$. We have imposed it to be exact in the total Lagrangian by removing just one term. Thus, n_{R3} is stable and it can in principle be a DM candidate. From here on, we consider N_{DM} (which is equal to n_{R3}, the difference being that N_{DM} is a mass basis field and the former a symmetry basis one) as a DM candidate and verify whether it satisfies the current experimental data. These data come essentially from investigations of Planck collaboration [45] which constrain the scaled DM relic density to be $\Omega_{\text{DM}}h^2 = 0.1193 \pm 0.0014$; and from direct detection (DD) limits of LUX [**?**], XENON100 [67] and SuperCDMS [138], which on the other hand constrain the cross section for scattering off nucleons to be smaller than 7.6×10^{-10} pb for a WIMP mass of 33 GeV. We will consider these constraints below.

Relic Abundance

In order to find the present scaled DM relic density $\Omega_{\text{DM}}h^2$ coming from the N_{DM} Majorana fermion, we must solve the Boltzmann differential equation. This standard procedure is well described in refs. [59, 61]. Here we are not going to divert into its details since we

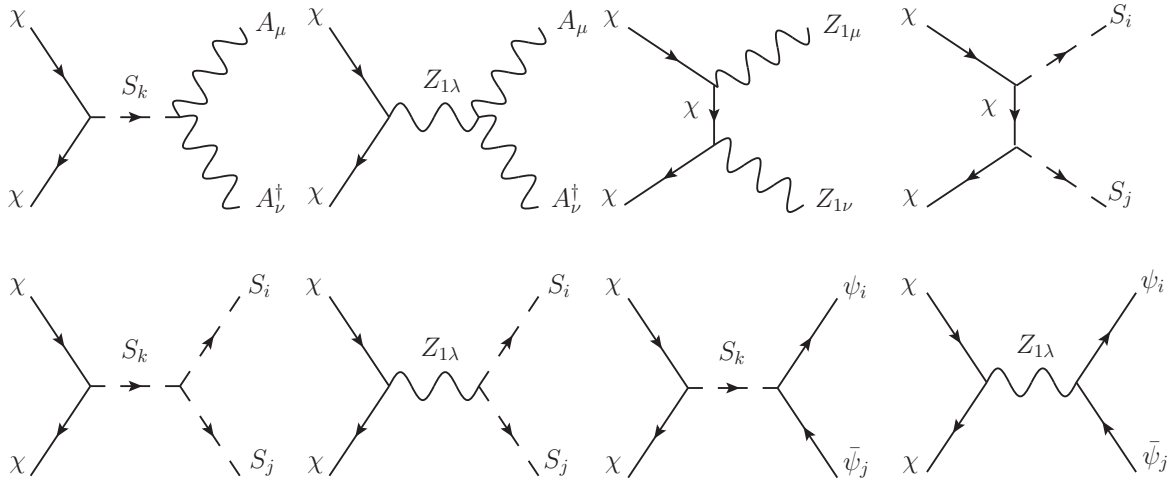

Figure 5.1: Feynman diagrams which represent the main annihilation processes that contribute to the calculation of $\Omega_{\rm DM}h^2$. We have defined: $\chi \equiv N_{\rm DM}$; $S_i \equiv R_i, I_i$; $A_\mu \equiv Z_{1\mu}, W_\mu^\pm$; and $A_\mu^0 \equiv Z_{1\mu}$.

have used the packages `Feynrules` [139], `Calchep` [140] and `MicrOMEGAs` [141]. The first two being auxiliary to the third that calculates $\Omega_{\rm DM}h^2$ for a given model which contains WIMPs.

In fig. 5.1 we show the processes which mainly contribute to the DM annihilation cross section, consequently leading to the present relic density. All of them depend on the parameters in the Lagrangians given in eqs. (5.2.1), (5.2.2) and on the kinetic terms involving the covariant derivatives. We have already fixed most of those parameters in sec. 5.2.2, however g, $g_{Y'}$, g_{B-L}, λ_H, λ_ϕ, λ_Φ, κ_{H2}, κ_{123} and $M_{\rm DM}$ still remain free[6]. The first three parameters g, $g_{Y'}$, g_{B-L} are the gauge coupling constants of the $\mathrm{SU}(2)_L$, $\mathrm{U}(1)_{Y'}$ and $\mathrm{U}(1)_{B-L}$ groups, respectively. Roughly speaking, these couplings and the VEVs together determine the masses of the gauge bosons; the VEVs have already been set in the previous section, i.e. $v_{\phi_1} = v_{\phi_2} = v_{\phi_3} = v_{\phi_X} = 1$ TeV and $v_H \simeq v_{\rm SM} = 246$ GeV, while $v_\Phi = \sqrt{v_{SM}^2 - v_H^2}$.

In addition, g can be set equal to 0.652 due to the $W^\pm$ mass. $g_{Y'}$ and g_{B-L} mainly determine the mass of the Z_2 gauge boson and its mixing with Z_1 in the neutral current (besides the Z_1 mass itself). From precision electroweak studies [142–144], its mixing — given by $\tan\beta$ — has to be $\lesssim 10^{-3}$ (see ref. [145] for an analytical expression of $\tan\beta$); also its mass should respect $M_{Z_2}/g_{B-L} \gtrsim 6\,\mathrm{TeV}$ [146,147]. In the end we find that working with $g_{Y'} = 0.506$ and $g_{B-L} = 0.505$, we obtain $\tan\beta \simeq 2 \times 10^{-4}$ and $M_{Z_2} \simeq 4.7\,\mathrm{TeV}$, as well as the known SM gauge bosons masses.

Now, the λ_H parameter is chosen to be $0.13 \leq \lambda_H \leq 0.14$ because it is the main responsible for the Higgs mass, $M_{\rm Higgs} = 125\,\mathrm{GeV}$, when $\kappa_{H2} \leq 0.1$. Whereas the λ_Φ and λ_ϕ parameters can take a wide range of values. We set $\lambda_\Phi = 0.5$ and $\lambda_\phi = 0.8$, and as a consequence we have the non-SM scalar masses larger than the SM particle masses.

[6] $M_{\rm DM} = \mathcal{M}_{33}v_\phi/\sqrt{2}$ is the mass of n_{R3}, obtained if one diagonalizes the neutrino mass matrix. For more details, see ref. [86].

The κ_{H2}, κ_{123} and $M_{\rm DM}$ parameters have been scanned in a broad region of values. Specifically, we have iterated the `MicrOMEGAs` package for the DM mass within the range 10 GeV $\leq M_{\rm DM} \leq$ 1000 GeV, taking into account different values of κ_{H2} and κ_{123}, and leaving the remaining parameters constant. In general, we have worked with $\kappa_{H2} =$ 0.1, 10^{-2}, 10^{-4} and $-0.56 \times \lambda_\phi \lesssim \kappa_{123} \leqslant 0$ ($0.56 \times 0.8 = 0.448$). The last choice because we must assure that all the scalar masses are real (we obtain a slightly more constraining condition on κ_{123} if we impose that all $CP-$even scalar must have masses larger than the Higgs boson, i.e. $\frac{1}{3.58 v_\phi^2}\left(m^2_{\rm Higgs} - 2\lambda_\phi v_\phi^2\right) \approx -0.442 < \kappa_{123} \leqslant 0$). Also, it is important to note that κ_{123} controls the scalar trilinear vertices between scalars.

Regarding the κ_{H2} parameter, we find that in our scenario it largely governs the invisible Higgs width $\Gamma^{\rm Inv}_{\rm Higgs}$ to non-SM particles. It is because κ_{H2} induces mixing between $\mathrm{Re}\, H^0$ and $\mathrm{Re}\,\phi_2$, consequently it mostly determines the Higgs $- J - J$ coupling (C_{hJJ}) since J has a component in $\mathrm{Im}\,\phi_2$. This C_{hJJ} coupling induces a tree-level contribution to the $\Gamma^{\rm Inv}_{\rm Higgs}$ given by $C^2_{hJJ}/32\pi m_{\rm Higgs}$. Under the assumption that the Higgs decays are correctly described by the SM aside perhaps from decay into new unobserved particles, the branching ratio for the Higgs decay into new invisible particles $\mathrm{Br}^{\rm Inv}_{\rm Higgs}$ is known to be $\lesssim 0.1 - 0.15$ [148–151]. For $\kappa_{H2} < 0.2$, we find that the $\mathrm{Br}^{\rm Inv}_{\rm Higgs}$ remains under 0.1 for $-0.442 \lesssim \kappa_{123} \leqslant 0$. We have been conservative choosing $\kappa_{H2} \leq 0.1$ for all results.

Taking into account all aforementioned considerations on the parameters, we plot in fig. 5.2 $\Omega_{\rm DM}h^2$ versus $M_{\rm DM}$ for $\kappa_{H2} = 10^{-1}$, 10^{-4}, with $\kappa_{123} = -0.4$ (the figure on the left) and $\kappa_{123} = -0.1$ (the figure on the right). The gray region has an overabundant $\Omega_{\rm DM}h^2$ and is ruled out. The dot-dashed line stands for $\Omega_{\rm DM}h^2 = 0.1193$ [45]. In general we find that depending on the $M_{\rm DM}$, various annihilation channels are important and clearly some resonances are visible; resonances are found at $M_{\rm DM} = m_{\rm mediator}/2$. Thus for convenience we give the scalar masses for both figures in fig. (5.2): for the case with $\kappa_{123} = -0.4$ (both values of κ_{H2}) we have approximately $m_{R_i} \simeq$ 125.0, 417.0, 411.3, 1435.8, 1549.2, 1603.0 GeV, $M_{I_i} \simeq$ 417.0, 970.4, 1748.8 GeV, and $M_{C^\pm} \simeq 417.0\,$GeV. On the other hand, for the case with $\kappa_{123} = -0.1$ (both values of κ_{H2}), we have approximately $m_{R_i} \simeq$ 125.0, 417.0, 1114.6, 1309.7, 1341.6, 1357.3 GeV, $M_{I_i} \simeq$ 417.0, 485.2, 874.4 GeV, $M_{\Phi^\pm} \simeq$ 417.0 GeV. In all cases we have the NG boson J.

In order to better comprehend the annihilation processes and their contributions contained in the curves in fig. 5.2, we plot fig. 5.3 which shows the relative contributions to $\Omega_{\rm DM}h^2$ of the main DM annihilation channels. Let us consider some relevant regions: for $M_{\rm DM}$ less than 80 GeV we have in general two resonances, the first one is due to the interchange of the Z_1 gauge boson in the $s-$channel, it is located at $M_{\rm DM} = M_{Z_1}/2 \approx 45.6$ GeV and remains there even when $\kappa_{H2} = 10^{-4}$. It is so because it depends on the $N_{\rm DM} - N_{\rm DM} - Z_1$ coupling via neutral currents. Since this coupling arises from the covariant derivatives, it is independent on the κ_{H2} parameter. In contrast, the second resonance which arises by the $s-$channel interchange of the Higgs boson (located in $m_{\rm Higgs}/2 \approx 62.5$ GeV), disappears when $\kappa_{H2} = 10^{-4}$. This on the other hand is understood by realizing that $N_{\rm DM}$ couples to the Higgs boson via the term $\frac{1}{2}\frac{\sqrt{2}M_{\rm DM}}{V_\phi}\overline{(n_{R3})^c} n_{R3}\phi_2$ and since the Higgs component in ϕ_2 depends on κ_{H2}, it is clear that the smaller κ_{H2} is, the smaller the

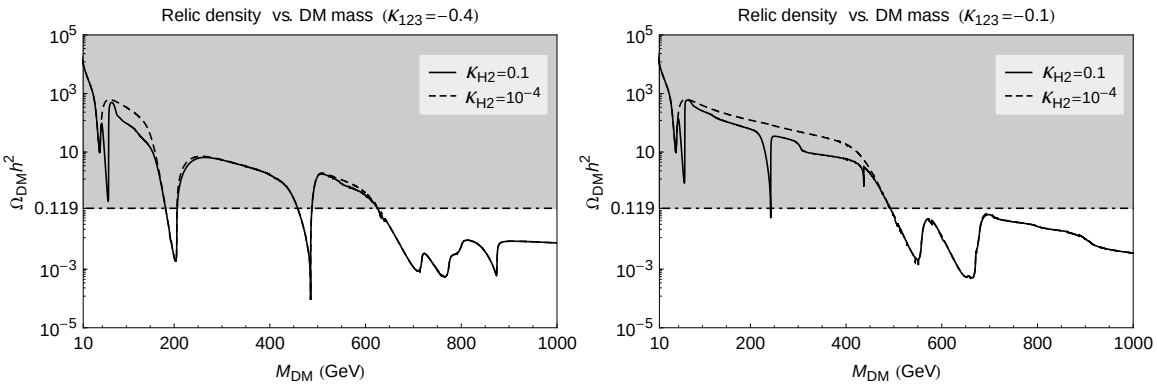

Figure 5.2: Figures displaying the dependence of $\Omega_{\rm DM}h^2$ on $M_{\rm DM}$, for $\kappa_{123} = -0.4$ (the figure on the left) and $\kappa_{123} = -0.1$ (the figure on the right). Each figure shows two cases corresponding to $\kappa_{H2} = 10^{-1}, 10^{-4}$. The dot-dashed line is the Planck $\Omega_{\rm DM}h^2$. The gray region means the DM candidate would be excluded, and the white one means that the DM candidate can still make some part of the DM content of the Universe.

$N_{\rm DM} - N_{\rm DM} -$ Higgs coupling gets. In this region of masses we also notice that $N_{\rm DM}$ annihilation processes into quark-antiquark pair (specially into $b\bar{b}$ quarks for $\kappa_{H2} = 10^{-1}$) are the dominant for both figures; these occur via Higgs mediation. Annihilation processes into neutrinos via the Z_1 interchange are also important ($\sim 25\%$). This is also true for both values of κ_{H2} and for both $\kappa_{123} = -0.4$ and -0.1.

As $M_{\rm DM}$ increases from 80 GeV to 120 GeV, and as long as $\kappa_{123} = -0.4$ and $\kappa_{H2} = 10^{-1}$, the annihilation into gauge bosons ($W^{\pm}/Z_1$) are dominant (in particular into W^+W^-) with some considerable ($\sim 20\%$) contribution of annihilation into quark-antiquark pair. In contrast, for $\kappa_{123} = -0.4$ and $\kappa_{H2} = 10^{-4}$, the $N_{\rm DM}$ annihilation processes into quark-antiquark pairs continue being the most important. Moreover, $N_{\rm DM}$ annihilation processes into JJ start to be considerable ($\sim 15\%$). For the lower frame, Similar conclusions are true for the case of $\kappa_{123} = -0.1$ and $\kappa_{H2} = 10^{-1}$ when compared with the case of $\kappa_{123} = -0.4$ and $\kappa_{H2} = 10^{-1}$, however the former has annihilations into gauge bosons ($W^{\pm}/Z_1$) a little less important than the latter. For the case of $\kappa_{123} = -0.1$ and $\kappa_{H2} = 10^{-4}$, the annihilations into antiquarks-quarks are the most relevant.

In the region $120\,{\rm GeV} \leq M_{\rm DM} \leq 180\,{\rm GeV}$ and with $\kappa_{123} = -0.4$ and $\kappa_{H2} = 10^{-1}$, roughly speaking three $N_{\rm DM}$ annihilation processes are similarly predominant. These are annihilations into W^+W^-/Z_1Z_1, R_1R_1 and JJ. Recall that R_1 is the Higgs-like scalar. For this region of mass and with $\kappa_{123} = -0.1$ and $\kappa_{H2} = 10^{-1}$, analogous conclusions can be reached. This is not the case for $\kappa_{H2} = 10^{-4}$ (with $\kappa_{123} = -0.4$) in the same $M_{\rm DM}$ region, since $N_{\rm DM}$ annihilations into JJ are almost completely dominant with an additional contribution ($\sim 12\%$) from the annihilations into quark-antiquark pairs. For $\kappa_{123} = -0.1$ and $\kappa_{H2} = 10^{-4}$, annihilations into quark-antiquark pairs are still dominant.

When $M_{\rm DM}$ is around $m_{R_3}/2 \approx 205$ GeV, we see a resonance in the left panel of fig. 5.2, due to the R_3 $s-$channel interchange for both κ_{H2} values. The predominant annihilation process is $N_{\rm DM}N_{\rm DM} \to JJ$ with more than 50% contribution. It is also important to note that for a $M_{\rm DM}$ in this region we have the mean $\Omega_{\rm DM}h^2$ PLANCK value. This resonance

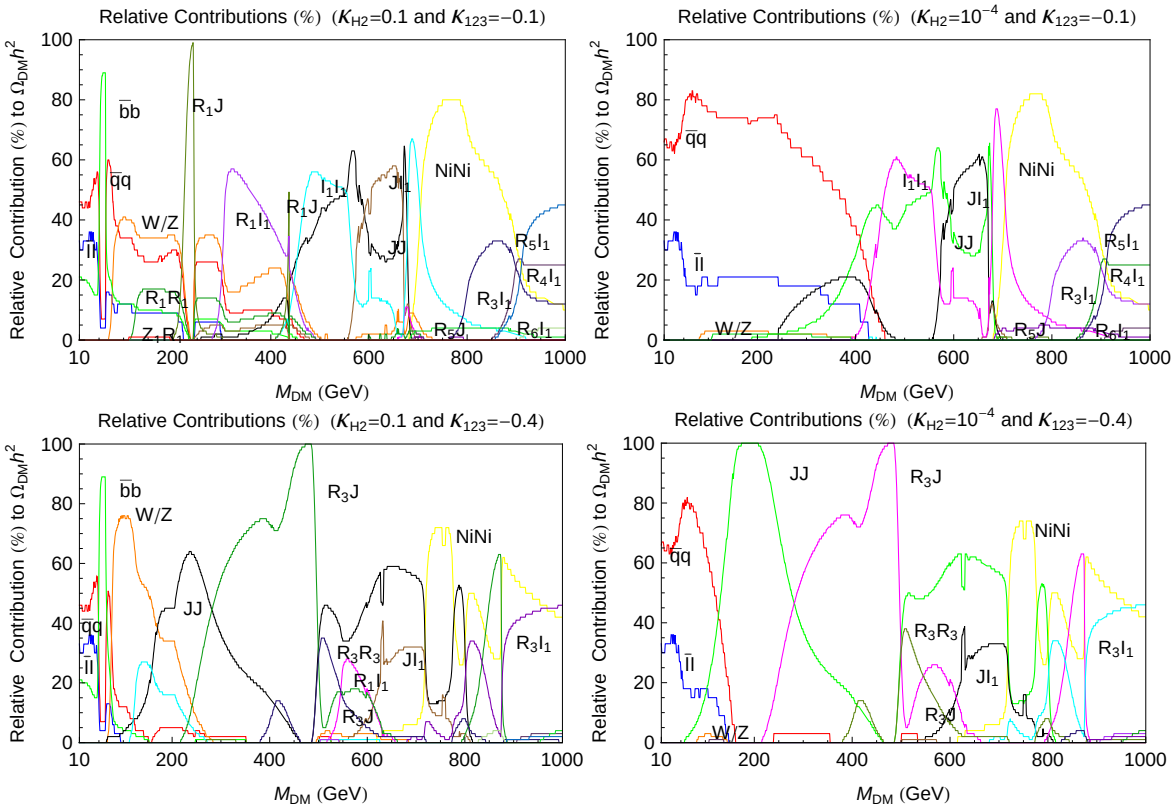

Figure 5.3: Figures displaying the relative contributions (%) of the main annihilation channels to the DM relic abundance. The cases with $\kappa_{H2} = 10^{-1}$, 10^{-4} and $\kappa_{123} = -0.1$, -0.4 are shown.

does not occur in the $\kappa_{123} = -0.1$ cases because then $m_{R_3} \approx 1114.61$ GeV. However, in these cases we have one resonance at $m_{I_2}/2 \approx 242.6$ GeV, with $N_{\rm DM}N_{\rm DM} \to R_1 J$ as the dominant process for $\kappa_{H2} = 10^{-1}$, and with $N_{\rm DM}N_{\rm DM} \to \bar{q}q$ as the dominant process for $\kappa_{H2} = 10^{-4}$.

In the region $220\,\text{GeV} \leq M_{\rm DM} \leq 500\,\text{GeV}$ and with $\kappa_{123} = -0.4$ and $\kappa_{H2} = 10^{-1}$, we can say that two annihilations processes, $N_{\rm DM}N_{\rm DM} \to JJ$ and $N_{\rm DM}N_{\rm DM} \to R_3 J$, strongly control $\Omega_{\rm DM}h^2$. Except when $M_{\rm DM} \approx m_{I_2}/2 \approx 485.1\,\text{GeV}$ where $N_{\rm DM}N_{\rm DM} \to R_3 J$ annihilation completely governs $\Omega_{\rm DM}h^2$. As $500\,\text{GeV} < M_{\rm DM} \leq 700\,\text{GeV}$, annihilations into JJ, R_1I_1, R_3R_3, R_3J and JI_1 are predominant and their contributions depend on the proximity to the three different resonances. Finally, when $700\,\text{GeV} < M_{\rm DM} \leq 1000\,\text{GeV}$, annihilations into JJ, R_3I_1, R_3J, N_1N_1 and N_2N_2 are the most contributing processes to determine $\Omega_{\rm DM}h^2$. Similar behavior is found for the case $\kappa_{123} = -0.4$ and $\kappa_{H2} = 10^{-4}$. It is so because in these regions of masses, the annihilation processes depend mostly on the trilinear vertices between scalars.

For $\kappa_{123} = -0.1$ and $\kappa_{H2} = 10^{-1}$, the scalar spectrum changes and thus the location of the resonances changes as well. As it was commented, the resonance at $m_{R_3}/2 \approx 205\,\text{GeV}$ does not exist anymore. Instead, we have a resonance at $m_{I_2}/2 \approx 242.6$ GeV. In the region $220\,\text{GeV} \leq M_{\rm DM} \leq 470\,\text{GeV}$, the most important difference, in contrast with the case $\kappa_{123} = -0.4$, is that we hardly have regions with $\Omega_{\rm DM}h^2 \leq 0.119$ (a little tiny region

can be seen in the $m_{I_2}/2 \approx 242.6\,\text{GeV}$). Another difference is that annihilation into W^+W^-/Z_1Z_1becomes important in this region ($\sim 15\% - 35\%$). In addition, annihilation into R_1I_1 contributes $> 35\%$ in most of this mass region. Other annihilation channels such as R_1J, I_1I_1, JJ and R_1R_1 also contribute, but are subdominant. For $470\,\text{GeV} \leq M_{\text{DM}} \leq 700\,\text{GeV}$, $\Omega_{\text{DM}}h^2$ is completely determined by annihilation into I_1I_1, I_1J, JJ. When $700\,\text{GeV} \leq M_{\text{DM}} \leq 1000\,\text{GeV}$, annihilation processes into N_1N_1 and N_2N_2 share importance with I_1I_1, R_3I_1, R_4I_1 and R_5I_1 to determine $\Omega_{\text{DM}}h^2$. For $M_{\text{DM}} > 470\,\text{GeV}$, the scaled relic density yields $\Omega_{\text{DM}}h^2 \leq 0.119$.

Finally, when $\kappa_{123} = -0.1$ and $\kappa_{H2} = 10^{-4}$, we have some relevant differences. The most prominent is that for $M_{\text{DM}} < 470\,\text{GeV}$ we just have the Z_1 resonance, which depends only on the VEVs and the covariant derivative g_i couplings. This is because of the smallness of κ_{123} and κ_{H2} (specially $\kappa_{H2} = 10^{-4}$), which makes the couplings with the $CP-$odd scalar mediators be tiny. Some other features are worth mentioning, though. Up to $M_{\text{DM}} \simeq 350\,\text{GeV}$, annihilation into quarks is predominant. After that, until $M_{\text{DM}} \simeq 700\,\text{GeV}$, the final products I_1I_1, I_1J, JJ (summing $\sim 35\% - 100\%$) enter as the major contributors to the relic density and the quarks enter as subdominant processes fading out at $M_{\text{DM}} \simeq 450\,\text{GeV}$. Next, up to $M_{\text{DM}} \simeq 900\,\text{GeV}$, the main annihilation products are N_1N_1 and N_2N_2 ($\sim 30\% - 40\%$ each), with R_3I_1 taking place at the end of this interval. Finally, for $850\,\text{GeV} \leq M_{\text{DM}} \leq 1000\,\text{GeV}$, the main contributions come from R_3I_1, R_4I_1 and R_5I_1, summing more than 70% of the DM annihilation energy.

Now, in order to grasp the behavior of the relic density when one continually varies κ_{123}, we show a two-dimensional figure, fig. 5.4, which was obtained with `MicrOMEGAs`, from a 10^5 points iteration. We see from it that as one varies κ_{123}, the regions for correct relic density (cyan points) change place, getting to the minimal value of $M_{\text{DM}} \sim 200$ GeV for $\kappa_{123} = -0.4$; and also for a straight band of points which increases in κ_{123} as M_{DM} decreases, having at $\kappa_{123} \sim -0.05$ its last point. We can also notice green regions (together with cyan lines) that extend from left to right as M_{DM} increases, and the reason behind these is the resonances of I_2, I_3 (which decrease as κ_{123} increases) and R_3 (which increases). Therefore, one can conclude that the correct relic density, before $M_{\text{DM}} \sim 500 - 600\,\text{GeV}$, may only be reached through resonances of the lightest singlet particles of our spectrum.

Direct Detection

Other important constraints on DM candidates come from the current experiments [67, 138, 152] which aim to directly detect WIMP dark matter by measuring the kinetic energy transferred to a nucleus after it scatters off a DM particle. All of these experiments have imposed limits on the WIMP scattering cross section off the nuclei. In general, the WIMP-nucleus interactions can be either spin-independent (SI) or spin-dependent (SD). Currently, the most constraining limits come from the Large Underground Xenon (LUX) experiment [**?**] which has set bounds on the SI WIMP-nucleon elastic scattering with a minimum upper limit on the cross section of 7.6×10^{-10} pb at a WIMP mass of 33 GeV/c^2.

We have verified that, for N_{DM} considered here, the dominant interactions are SI. Thus,

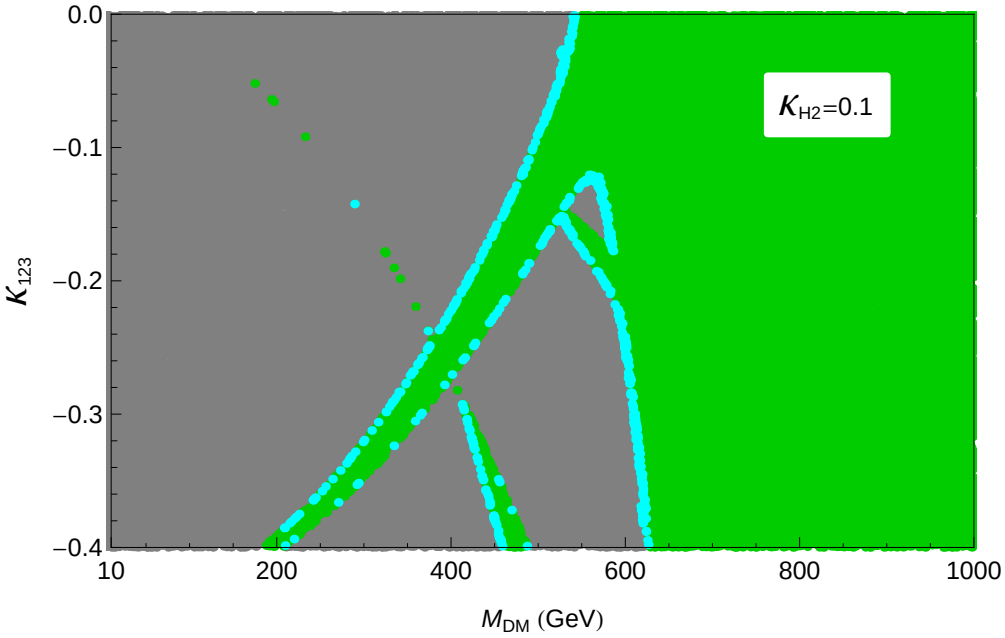

Figure 5.4: 2-D figure displaying the behavior of $\Omega_{\rm DM}h^2$ as one continuously varies both κ_{123} in the range $[-0.4, 0]$, with $\kappa_{H2} = 0.1$, and $M_{\rm DM}$ in the range $[10, 1000]$ GeV. The cyan points represent correct relic density $\Omega_{\rm DM}h^2$, within experimental errors; the green ones indicate $\Omega_{\rm DM}h^2$ below the Planck result; and the gray ones mean $\Omega_{\rm DM}h^2$ above Planck constraint and thus ruled out.

we calculate (using the `MicrOMEGAs` package) the SI elastic scattering cross section per nucleon, $\sigma_{\text{SI-nucleon}}$, and the results are shown in fig. 5.5. Actually, we scale the $\sigma_{\text{SI-nucleon}}$ cross sections with the calculated relic density relative to that measured by PLANCK in order to properly compare the predicted cross sections with those given by direct detection experiments, which present their results assuming the observed density at the time of the experiment. The experimental limits on SI cross sections are also shown in fig. 5.5. We have not shown results for SD cross sections because we found that those are generally several orders of magntiude below the SI current limits, see refs. [153, 154] which state a minimum upper bound of $\sim 5 \times 10^{-3}$ pb at a WIMP mass of $24\,\text{GeV}/c^2$.

From fig. 5.5, it can be seen that the smaller the value of κ_{H2}, the smaller the value of $\sigma_{\text{SI-nucleon}}$. For $\kappa_{H2} = 10^{-2}$, the $\sigma_{\text{SI-nucleon}}$ is below the LUX upper bound for all values of $M_{\rm DM}$. For $\kappa_{H2} = 10^{-1}$ and $M_{\rm DM} \lesssim 500$ GeV, $\sigma_{\text{SI-nucleon}}$ is below the LUX limit only around the resonances. In contrast, for $M_{\rm DM} \gtrsim 500$ GeV, the LUX limits are satisfied for all cases shown in fig. 5.5. This implies that $\sigma_{\text{SI-nucleon}}$ mainly depends on κ_{H2}. This fact is easily understood by realizing that, in our case, the relevant interactions for direct detection are mostly mediated via Higgs in the t-channel . Thus, these interactions depend on the mixings between the Higgs scalar (R_1) and rest of R_i scalars. These mixings strongly depend on the κ_{H2} value, as was already discussed. In addition, we can see from fig. 5.5 that although $\sigma_{\text{SI-nucleon}}$ (actually $\sigma_{\text{SI-nucleon}} \times \Omega_{\rm DM}h^2/0.1193$) does not depend directly on other scalars, there is clearly indirect dependence on them because these scalars affect the relic abundance through the annihilation cross section.

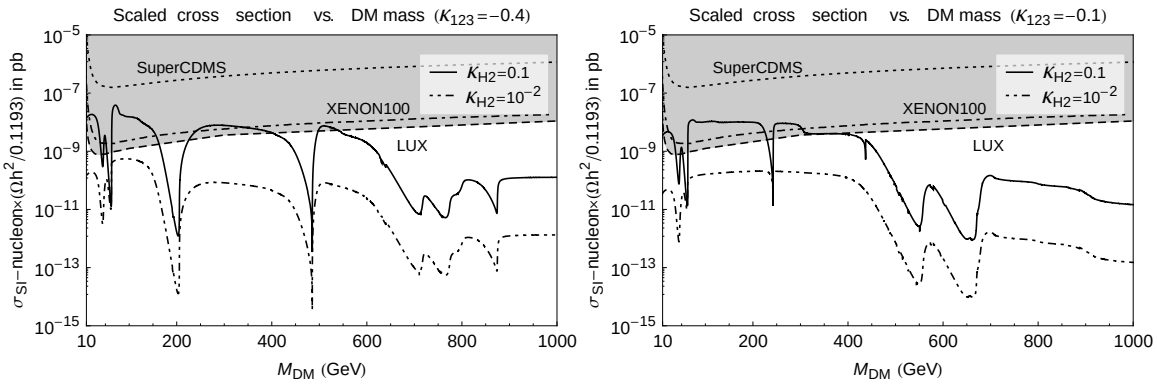

Figure 5.5: Figures displaying the curves representing the SI cross section per nucleon, $\sigma_{\text{SI-nucleon}}$, asa function of M_{DM}, for the N_{DM} elastic scattering off nucleon. Cases for $\kappa_{123} = -0.4$; -0.1 and $\kappa_{H2} = 10^{-1}, 10^{-2}$ are shown. In these figures, we also display the SI upper limits coming from LUX (dashed), XENON100 (dot-dashed) and SuperCDMS (dotted). All $\sigma_{\text{SI-nucleon}}$ curves in the gray region are ruled out by the LUX upper limit.

Finally, from figs. 5.2 and 5.5 we can conclude that, provided $\kappa_{H2} \lesssim 10^{-2}$, the constraints coming from only $\Omega_{\text{DM}}h^2$ determine whether a set of parameters leads to a viable dark matter candidate or not.

6 Outside the standard relic freezout scenario

Up to now, we worked in a context where the considered particle species χ is in thermal equilibrium with the relativistic plasma up to the point $\sim x_f$, after which its comoving number density becomes constant. In the present chapter, after giving a theoretical introduction to the subject in the first section, we provide an example study in which non-thermal dark matter has been considered, alongside entropy dilution issues. and the important problem of uplifting within Supergravity background.

6.1 Framework

The idea behind non-thermal relics production is that a feebly interacting particle be introduced into the standard scheme of freezout. In other words, additionally to the SM content (radiation) and the dark matter candidate species χ, the extra field ϕ is introduced. The latter can possibly decay into radiation and dark matter, increasing the radiation energy density ρ_R and the dark matter number density n_χ. Differently from the standard treatment where only one Boltzmann equation is considered (3.4.1), here we have to keep track of the radiation energy density, theχ number density and the ϕ energy density ρ_ϕ. Thus, neglecting significant thermal interactions between ϕ and SM or χ, it yields [155, 156]

$$\frac{d\rho_\phi}{dt} = -3H\rho_\phi - \Gamma_\phi \rho_\phi \quad , \tag{6.1.1}$$

$$\frac{d\rho_R}{dt} = -4H\rho_R + (1-B_\chi)\,\Gamma_\phi\rho_\phi + \langle\sigma v\rangle\, 2\,\langle E_\chi\rangle \left[n_\chi^2 - \left(n_\chi^{\rm eq}\right)^2\right] \quad , \tag{6.1.2}$$

$$\frac{dn_\chi}{dt} = -3Hn_\chi + B_\chi\Gamma_\phi\rho_\phi - \langle\sigma v\rangle \left[n_\chi^2 - \left(n_\chi^{\rm eq}\right)^2\right] \quad . \tag{6.1.3}$$

The symbol $\langle E_\chi\rangle \simeq \sqrt{m_\chi^2 + 3T^2}$ stands for the average energy per χ particle when in kinetic equilibrium with the radiation at temperature T; $B_\chi \left(= \Gamma_\phi^\chi/\Gamma_\phi\right)$ is the braching ratio of ϕ decays into χ; $\langle\sigma v\rangle$ is the thermally averaged cross section of the species χ. The Hubble parameter is given by

$$H^2 = \frac{8\pi}{3M_{\rm Pl}^2}\left(\rho_\phi + \rho_R + \rho_\chi\right) \quad , \tag{6.1.4}$$

where $M_{\rm Pl} \simeq 1.22 \cdot 10^{19}$ GeV is the Planck mass. The equilibrium number density for particles obeying Maxwell-Boltzmann statistics can be expressed in terms of the bessel function of the second kind K_2,

$$n_\chi^{\rm eq} = \frac{\boldsymbol{g}_\chi T^3}{2\pi^2} \left(\frac{m_\chi}{T}\right)^2 K_2\left(m_\chi/T\right) \quad . \tag{6.1.5}$$

The quantities Γ_ϕ, ρ_ϕ, B_χ, $\langle\sigma v\rangle$ and $\langle E_\chi\rangle$ are model-dependent. $\langle E_\chi\rangle$ (or basically m_χ) is a free parameter in most models of particle physics; ρ_ϕ (which is the oscillation energy density of the field ϕ) depends on the ϕ mass M_ϕ and on the epoch at which the oscillation started, i.e. $H \sim M_\phi$. Since ϕ interacts very feebly and has a very high mass, it is usually supposed to stem from UV-complete theories, and therefore its decay rate is Planck suppressed:

$$\Gamma_\phi = \alpha \frac{M_\phi^3}{M_{\rm Pl}^2} \quad , \tag{6.1.6}$$

where α is a coefficient which depends on the high energy theory. A natural consequence of a high energy ϕ is that one can safely assume $m_\chi \ll M_\phi$. As well as α, the ratio B_χ and $\langle\sigma v\rangle$ depend on the model and parametrization one uses. Notice again that a term with $\langle\sigma v\rangle_\phi$ does not exist since we assume ϕ never thermalizes.

This is the most basic scenario where an extra field ϕ can be introduced to increase ρ_R and n_χ, and modify the standard thermal framework wherein n_χ interacts solely with the SM plasma. Next, we present an example study within a specific model.

6.2 Dark matter and entropy production in the ISS model

Now we describe an example [157] of a model in which the additional fields are introduced into the picture of standard thermal freezout of relics. In the next subsection, we first introduce the general features of the model, including fields and the achievement of uplifting, leaving oscillations and decays of the ISS fields as well as dark matter production for the next subsections.

6.2.1 Fields and uplifting

The field content of the model is given by the KL modulus, the ISS fields, the inflaton and the MSSM field content. For this study, we work within the Supergravity framework, thus both Kähler potential K and Superpotential W must be provided for the full theory description. As a consequence of working with Supergravity, all considered fields have superpartners.

KL modulus

The KL modulus arises as a consequence of compactification in string theory and corresponds to the volume modulus[1], which is massless at this stage. More specifically, it stems from the type II String Theory compactified on an orientifolded Calabi-Yau threefold M with the presence of fluxes [158, 159], which yields the following Kähler potential and superpotential for the KL modulus:

$$W_{\rm KL} = W_0 + Ae^{-a\rho} - Be^{-b\rho} \quad , \tag{6.2.1}$$

$$K_{\rm KL} = -3\ln\left(\rho+\bar{\rho}\right) \quad . \tag{6.2.2}$$

W_0 is a tree level contribution from the fluxes. The exponential terms $Ae^{-a\rho}$ and $Be^{-b\rho}$ arise either from euclidean D3 branes or from gaugino condensation on D7 branes [158]; also A, B, a, $b > 0$. In order to discuss the KL modulus further, we need to introduce here the scalar potential of the $\mathcal{N}=1$ Supergravity:

$$V = e^K\left(K^{a\bar{b}}D_aW\overline{D}_{\bar{b}}\overline{W} - 3\overline{W}W\right) \quad , \tag{6.2.3}$$

where $D_aW = \partial_aW + (\partial_aK)\,W$ and $K^{a\bar{b}} = \partial_a\partial_{\bar{b}}K$, with a and $\bar{b}$ being field and conjugate field indices, respectively. This equation will be used later on when we discuss the uplifting and interactions among scalars. If one would consider the KL modulus alone within eq. (6.2.3), the largest supersymmetric minimum of the potential is the Minkowski vacuum[2] $V_{\rm KL} = 0$, which demands $W_{\rm KL} = 0$. For a dS vacuum, $V > 0$, additional terms must be introduced, for example non-perturbative terms from the addition of several anti-D3-branes that do not add further moduli to the discussion. Also as solutions, one might add F-terms from the O'KKLT model [160] or the ISS dynamical sector [161]; this is called *uplifting*.

It is worthwhile to comment that the first version of the KL model, the KKLT model [158], had a quite serious inconvenience. When one breaks supersymmetry covariance, thus $D_aW \neq 0$, the gravitino mass achieved in the KKLT model is $\sim m_\rho/60$ [162], where m_ρ is the modulus mass. This means that for gravitino masses of $\mathcal{O}\,(\text{TeV})$, the volume stabilization in the KKLT is very soft (i.e. small m_ρ), which demands low scale inflation $H \lesssim m_{3/2}$ in order for the volume stabilization and compactification of extra dimensions to apply. Of course, one could opt for gravitino masses of $\mathcal{O}\,(M_{\rm Pl})$, thus opening the possibility of a high scale inflation also with $H \lesssim m_{3/2}$, however supersymmetry breaking at the Planck scale is not desired. On the other hand, in the KL model the ρ mass is not linked to the $\psi_{3/2}$ mass any longer, which provides high scale inflation with low scale supersymmetry breaking. Further details will be provided when discussing uplifting of the AdS vacuum.

[1] All the complex structure moduli and the dilaton are fixed at the very large mass scale $m \sim T^{-1}/R^3$, where T is the string tension and R is the radius of the orientifolded Calabi-Yau threefold M.

[2] For a supersymmetric vacuum, one must ensure $D_\rho W_{\rm KL} = 0$.

ISS sector

In the scenario we consider in this work, the fields which will accomplish the uplifting, via spontaneous symmetry braking, will be the fields contained in the ISS model [161].

The use of strong gauge dynamics in dynamical SUSY breaking that can explain the hierarchy between the Planck scale and the weak scale is known [163]. A variety of models discussing dynamical SUSY breaking in a stable ground state exist, but nonetheless create complicated issues for model building and phenomenology [164]. One of the theoretical issues is the non-zero Witten index of $\mathcal{N} = 1$ Yang-Mills theory: it implies that any $\mathcal{N} = 1$ supersymmetric gauge theory with massive, vector-like matter has supersymmetric vacua, therefore theories with no supersymmetric vacua must be either chiral or massless non-chiral. The satisfaction of these requirements and dynamical SUSY breaking turn theories rather complicated. In the original work of the ISS model, much simpler and phenomenologically viable models were constructed by allowing dynamical SUSY breaking to take place in metastable long-lived vacua.

The ISS sector we deal with here consists of a theory which arises in the so-called free magnetic dual range $N_c + 1 \leq N_f < 3N_c/2$ of $SU(N_c)$ $\mathcal{N} = 1$ SUSY QCD with confinement scale Λ coupled to N_f chiral multiplets (flavours) Q^i in the N_c representation and $\bar{N}_f$ $(= N_f)$ chiral multiplets $\tilde{Q}_i$ in the $\bar{N}_c$ representation, where $i, \tilde{i} = 1, \ldots, N_f$. The anomaly free global symmetry of SUSY QCD is

$$SU(N_f)_L \times SU(N_f)_R \times U(1)_B \times U(1)_R \quad . \tag{6.2.4}$$

The transformations for the quarks Q and $\tilde{Q}$ are given by

$$Q \qquad (N_f, 1, 1, 1) \quad , \tag{6.2.5}$$

$$\tilde{Q} \qquad \left(1, \bar{N}_f, -1, 1\right) \quad . \tag{6.2.6}$$

The original description of SUSY QCD is the free non-Abelian *electric* phase in terms of *electric* variables, which is an $SU(N_c)$ gauge theory with N_f chiral multiplets. The dual description is the free non-Abelian *magnetic* phase in terms of *magnetic* variables, which is an $SU(N)$ theory, where $N = N_f - N_c$, with N_f flavours and N_f^2 extra gauge invariant massless fields. As expected, when one theory is weakly coupled, the other theory is strongly coupled in the sense of Seiberg duality [165]. For $N_f \geq 3N_c$, the original electric theory is free in the IR and the magnetic one is infinitely strongly coupled, whereas for $N_c + 1 \leq N_f < 3N_c/2$ the behaviour is reversed, with the magnetic theory being free in the IR and the electric one infinitely coupled.

Therefore, when the ISS model is mentioned, it is meant as the IR free, low energy effetive theory of the magnetic dual of $SU(N_c)$ $\mathcal{N} = 1$ SUSY QCD in the range $N_c + 1 \leq N_f < 3N_c/2$, $N = N_f - N_c$.

More precisely, the ISS model consists of ISS fields ϕ_{ISS}, which collectively denote the

chiral superfields[3] q_i^a, $\tilde{q}_b^j$ and S_j^i, where $i,\ j = 1, \ldots, N_f$ are flavour indices; $a,\ b = 1, \ldots, N$, and $N_f > N = N_f - N_c$. The global symmetry group is given by

$$SU(N) \times SU(N_f)_L \times SU(N_f)_R \times U(1)_B \times U(1)' \times U(1)_R \quad . \tag{6.2.7}$$

The fields transformations for q, $\tilde{q}$ and S are given by

$$q \quad \left(N, \bar{N}_f, 1, 1, 1, 0\right) \quad , \tag{6.2.8}$$
$$\tilde{q} \quad \left(\bar{N}, 1, N_f, -1, 1, 0\right) \quad , \tag{6.2.9}$$
$$S \quad \left(1, N_f, \bar{N}_f, 0, -2, 2\right) \quad . \tag{6.2.10}$$

The Kähler potential and the tree-level superpotential - without gauging $SU(N)$ - for the magnetic dual theory of SUSY QCD can be written as

$$K_{\text{ISS}} = |q|^2 + |\tilde{q}|^2 + |S|^2 = q_i^a \bar{q}_a^i + \tilde{q}_a^i \bar{\tilde{q}}_i^a + S_j^i \bar{S}_i^j \quad , \tag{6.2.11}$$
$$W_{\text{ISS}} = h\left(\text{Tr}\tilde{q}Sq - M^2\text{Tr}S\right) = h\left(\tilde{q}_a^i S_i^j q_j^a - M^2 S_i^j \delta_j^i\right) \quad , \tag{6.2.12}$$

where h is a dimensionless coupling and $M \ll M_P$ is the energy scale of the ISS model[4].

Inflaton and MSSM

In this work, we use the canonical Kähler potential for the MSSM fields

$$K_{\text{MSSM}} = \phi\bar{\phi} \quad , \tag{6.2.13}$$

where we collectively denote the MSSM fields by ϕ. Also, whenever the MSSM superpotential is mentioned later in the text, its symbol will be written as W_{MSSM}. Additionally, we introduce a Giudice-Masiero term [166]

$$K_{\text{GM}} = c_H H_1 H_2 + \text{h.c.} \quad , \tag{6.2.14}$$

where H_1 and H_2 are the MSSM Higgs superfields and c_H is a constant with no mass dimension. This term is often phenomenologically required for the solutions of tanβ and μ to lie in an acceptable range of values (for example, μ being real and tanβ real and positive), within the four-dimensional effective low-energy theory context [162, 167, 168]. Also, in the original paper of Giudice and Masiero's, the μ-term problem was tackled.

For the inflaton, we need a field which accomplishes inflation and does not decay into gravitinos. The latter requirement makes for simplicity and is dealt with in sec. 6.2.4. Therefore, despite not explicitly using its Kähler potential and superpotential throughout this work, two expressions that accomplish what we require of the inflaton can be found

[3] The S_j^i is the extra gauge invariant massless field mentioned earlier.
[4] M_{P} is the reduced Planck mass, related to the Planck mass M_{Pl} by $M_{\text{P}} = M_{\text{Pl}}/\sqrt{8\pi}$.

in [169], given by

$$W_\eta = Sf(\eta) \quad , \tag{6.2.15}$$
$$K_\eta = K\left((\eta-\bar{\eta})^2, S\bar{S}\right) \quad , \tag{6.2.16}$$

where the scalar S is called a stabilizer field.

Vacuum uplifting

As we have seen above, the most positive vacuum achieved with the KL model only is a Minkowski one, i.e. $\Lambda = 0$, where Λ is the cosmological constant. As we know, our universe has a positive cosmological constant, $\Lambda_{\text{our}}/M_{\text{P}}^2 \sim 10^{-120}$. Therefore the KL sector needs uplifting, which in our work comes from the ISS model. This means we consider the following combinations

$$K_{\text{KL-ISS}} = -3\ln(\rho+\bar{\rho}) + |q|^2 + |\tilde{q}|^2 + |S|^2 \quad , \tag{6.2.17}$$
$$W_{\text{KL-ISS}} = W_0 + Ae^{-a\rho} - Be^{-b\rho} + h\left(\text{Tr}\tilde{q}Sq - M^2\text{Tr}S\right) \quad , \tag{6.2.18}$$

for the Kähler potential and superpotential, where A, B, a, $b > 0$.

For the vacuum structure of KL alone, let $\text{Im}\rho = 0$ and $\text{Re}\rho = \sigma$, which means we search for a vacuum in the real part of ρ. Furthermore, let σ_0 be the value of ρ at its minimum. The supersymmetric Minkowski vacuum $V_{\text{KL}}(\sigma_0) = 0$ must satisfy

$$D_\rho W_{\text{KL}}|_{\sigma=\sigma_0} = \partial_\rho W_{\text{KL}}|_{\sigma=\sigma_0} + (\partial_\rho K_{\text{KL}})\, W_{\text{KL}}|_{\sigma=\sigma_0} = 0 \quad , \tag{6.2.19}$$
$$W_{\text{KL}}(\sigma_0) = 0 \quad . \tag{6.2.20}$$

Allowing $W_{\text{KL}}(\sigma_0) \neq 0$, namely $W_{\text{KL}}(\sigma_0) \equiv \Delta$, shifts the minimum to the supersymmetric AdS minimum

$$V_{\text{KL}}(\sigma_0) \simeq -3m_{3/2}^2 \simeq -\frac{3\Delta^2}{8\sigma_0^3} \quad . \tag{6.2.21}$$

Note that for the supersymmetric vacuum to apply, one must ensure $D_\rho W_{\text{KL}}|_{\sigma_{\text{new}}} = 0$, which can be done for $\sigma_{\text{new}} = \sigma_0 + \delta\sigma$, where $\delta\sigma \ll \sigma_0$ [170].

Now to the uplifting of the KL vacuum. As said before, it is accomplished by the ISS model. By working out the first derivative of the effective four-dimensional $\mathcal{N} = 1$ supergravity scalar potential with no D-terms (6.2.3), namely $\partial_{\phi_{\text{ISS}}} V_{\text{KL-ISS}} = 0$, the ISS vacuum $(S_0, q_0, \tilde{q}_0)$ is given by

$$(S_0)^i_j = 0 \quad , \tag{6.2.22}$$
$$(q_0)^a_i = M\delta^a_i \quad , \tag{6.2.23}$$
$$(\tilde{q}_0)^j_b = M\delta^j_b \quad . \tag{6.2.24}$$

From a matrix viewpoint, q_0 and $\tilde{q}_0$ can be written as

$$q_0 = \begin{pmatrix} M\mathbb{I}_{N\times N} \\ 0_{(N_f-N)\times N} \end{pmatrix} \quad , \tag{6.2.25}$$

$$\tilde{q}_0 = \begin{pmatrix} M\mathbb{I}_{N\times N} & 0_{N\times(N_f-N)} \end{pmatrix} \quad . \tag{6.2.26}$$

These are the VEVs responsible for spontaneous symmetry breaking in the ISS model that allow for a possible uplifting of the AdS vacuum from the KL sector (6.2.21). As a matter of fact, from terms $e^{K_{\text{KL-ISS}}}\partial_{\{q,\tilde{q},S\}}W_{\text{KL-ISS}}\partial_{\{\bar{q},\bar{\tilde{q}},\bar{S}\}}\overline{W}_{\text{KL-ISS}}$ in eq. (6.2.3), these VEVs imply that the minimum of the KL-ISS scalar potential yields (with $M_{\text{P}}=1$)

$$V_{\text{min}} = \frac{e^{2NM^2}}{(2\sigma_0)^3}\left[\Delta^2\left(-3+2NM^2\right)+h^2M^4\left(N_f-N\right)\right] \quad . \tag{6.2.27}$$

Since $M \ll M_{\text{P}}$, we neglect the term $2NM^2$ compared with -3 in the first brackets of eq. (6.2.27) unless a huge $N = N_f - N_c$ of $\mathcal{O}\left(10^{10}\right)$ is considered. The scalar potential minimum must equal the small but positive cosmological constant. From that equality we obtain a constraint for the parameter Δ, namely

$$|\Delta| \simeq \sqrt{\frac{N_f-N}{3}}hM^2 \quad . \tag{6.2.28}$$

The expected gravitino mass due to the supersymmetry breaking sector (the ISS sector with parameters h and M) and the value $\sigma_0 = \text{Re}\rho|_{\text{min}}$ is given by

$$m_{3/2} = \left\langle e^{K/2}W\right\rangle \simeq \frac{|\Delta|}{(2\sigma_0)^{3/2}}e^{NM^2} \simeq \frac{e^{NM^2}}{(2\sigma_0)^{3/2}}\sqrt{\frac{N_f-N}{3}}hM^2 \quad . \tag{6.2.29}$$

Restoring the reduced Planck mass M_{P}, it yields

$$m_{3/2} \simeq \frac{e^{NM^2/M_{\text{P}}^2}}{(2\sigma_0/M_{\text{P}})^{3/2}}\sqrt{\frac{N_f-N}{3}}h\left(\frac{M}{M_{\text{P}}}\right)^2 M_{\text{P}} \quad . \tag{6.2.30}$$

Since M is assumed to be well below M_{P} — recall the smallness of M due to the dynamical nature of the ISS sector — we set $e^{NM^2/M_{\text{P}}^2} = 1$ throughout the work. Also, unless otherwise stated, we work with a set of units where $M_{\text{P}} = 1$. We will see later that σ_0 depends on the parameters a, b , A and B from W_{KL}, therefore the gravitino mass ends up as a function of a, b , A, B, h and M.

As a final note, the kind of uplifting we do here is the so-called F-term uplifting, where the uplifting contributions stem only from the F-term (6.2.3) in the scalar potential. If the ISS model was gauged, D-term uplifting would be possible.

6.2.2 Masses, symmetry breaking and decay rates

In the previous section, we focused on the fields motivations, their Kähler potential and superpotential, as well as the F-term uplifitng of the KL vacuum by the ISS sector. Now we discuss the properties of the modulus ρ and the ISS fields $\phi_{\rm ISS}$, which will be relevant to the cosmological analysis of the primordial universe. From this subsection on, we write the ISS fields only with lowered indices for an easy display.

Masses and symmetry breaking

To obtain the masses for the ISS and modulus fields, we first compute the 8×8 non-diagonal mass matrix for ρ, $\bar{\rho}$, S, $\bar{S}$, q, $\bar{q}$, $\tilde{q}$, $\bar{\tilde{q}}$ from the scalar potential (6.2.3) in our scenario and then diagonalize it, yielding the following masses:

- The modulus scalar field ρ

It is possible to obtain the following mass (with $M_{\rm P} = 1$) for the real and imaginary components of the modulus scalar field ρ:

$$m_\rho^2 = \frac{2}{9} AaBb\,(a-b) \left[\frac{Aa}{Bb}\right]^{\frac{-a-b}{a-b}} \ln\left(\frac{aA}{bB}\right) + \mathcal{O}\left(M^2\right) \quad . \tag{6.2.31}$$

If we set for example $a = 0.1$, $b = 0.05$, $A = 1$, $B = 1$, we obtain $m_\rho \simeq 2.19 \cdot 10^{-3}$ (in $M_{\rm P}$ units). This value is much heavier than the inflaton reference mass we will use in this work, namely $m_\eta = 10^{-5}$.[5] As shown in [169], one of the conditions to ignore the dynamics of the modulus field during inflation is that its mass must be much heavier than the inflaton mass. Following this procedure, ρ and η decouple and can be studied separately. This implies that the modulus field does not receive contributions from the inflaton potential during and after inflation, which in turn leads to a vanishing oscillation amplitude of ρ. This point will be developed further in sec. 6.2.3.

For completeness, the ρ value at the minimum of the potential is given by the VEV of its real part Reρ, namely σ_0, which we compute to be $\sigma_0 = \frac{1}{a-b} \ln\left(\frac{aA}{bB}\right) + \mathcal{O}\left(M^2\right)$; also the parameter W_0 from the KL superpotential can be expressed as $W_0 = -A\left(\frac{aA}{bB}\right)^{\frac{a}{b-a}} + B\left(\frac{aA}{bB}\right)^{\frac{b}{b-a}} + \mathcal{O}\left(M^2\right)$. Using the same parameters we used to obtain m_ρ, it yields $\sigma_0 \simeq 13.86$ and $W_0 \simeq 0.25$.

- The ISS scalar fields $\phi_{\rm ISS}$

We continue the analysis for the ISS fields. We write the following combinations Q_1, Q_2, Q_3, Q_4 for q, $\bar{q}$, $\tilde{q}$, $\bar{\tilde{q}}$ firstly with $i = 1, \ldots, N$ and $a = 1, \ldots, N$,

[5] In the simplest chaotic inflation models, $m_\eta \sim 6 \cdot 10^{-6}$.

$$\text{Re, Im}\left[Q_1\right] = \frac{1}{2}\left(q_{ai} \pm \bar{q}_{ai} + \tilde{q}_{ia} \pm \bar{\tilde{q}}_{ia}\right) \quad , \tag{6.2.32}$$

$$\text{Re, Im}\left[Q_2\right] = \frac{1}{2}\left[q_{ai} \pm \bar{q}_{ai} - \left(\tilde{q}_{ia} \pm \bar{\tilde{q}}_{ia}\right)\right] \quad , \tag{6.2.33}$$

and secondly with $i = N+1, \ldots, N_f$ and $a = 1, \ldots, N$,

$$\text{Re, Im}\left[Q_3\right] = \frac{1}{2}\left(q_{ai} \pm \bar{q}_{ai} \pm \tilde{q}_{ia} + \bar{\tilde{q}}_{ia}\right) \quad , \tag{6.2.34}$$

$$\text{Re, Im}\left[Q_4\right] = \frac{1}{2}\left[q_{ai} \pm \bar{q}_{ai} - \left(\pm\tilde{q}_{ia} + \bar{\tilde{q}}_{ia}\right)\right] \quad . \tag{6.2.35}$$

We show in table 6.1 the number of real or imaginary components as well as the mass eigenvalues for each of the 6 kinds of mass eigenstates constructed from the ISS fields S, $\bar{S}$, q, $\bar{q}$, $\tilde{q}$, $\bar{\tilde{q}}$ after diagonalization of the mass matrix.

ISS scalar mass eigenstate	$\text{Number}_{\text{Re/Im}}$	Mass
$S_1 \equiv S_{ij}\,(i \otimes j \in N^2)$	N^2	$\sqrt{\frac{6}{N_f - N}}\left(\frac{M_P}{M}\right) m_{3/2}$
$S_2 \equiv S_{ij}\left(i \otimes j \in N_f^2 - N^2\right)$	$(N_f + N)(N_f - N)$	$\mathcal{O}\left(m_{3/2}\right)$
$Q_1 \equiv \text{Lc}\left[q_{ia}, \tilde{q}_{ai}\right](i \otimes a \in N^2)$	N^2	$\sqrt{\frac{6}{N_f - N}}\left(\frac{M_P}{M}\right) m_{3/2}$
$Q_2 \equiv \text{Lc}\left[q_{ia}, \tilde{q}_{ai}\right](i \otimes a \in N^2)$	N^2	0
$Q_3 \equiv \text{Lc}\left[q_{ia}, \tilde{q}_{ai}\right](i \otimes a \in N_f N - N^2)$	$(N_f - N)\,N$	$\sqrt{\frac{6}{N_f - N}}\left(\frac{M_P}{M}\right) m_{3/2}$
$Q_4 \equiv \text{Lc}\left[q_{ia}, \tilde{q}_{ai}\right](i \otimes a \in N_f N - N^2)$	$(N_f - N)\,N$	0

Table 6.1: Tree level largest contributions to the masses of the ISS scalar mass eigenstates. For the first column, the notation is such that N^2 is the cartesian product $N \otimes N$ with $N = \{1, \ldots, N\}$; N_f^2 is the cartesian product $N_f \otimes N_f$, with $N_f = \{1, \ldots, N_f\}$; and $N_f N$ with $N = \{1, \ldots, N\}$ and $N_f = \{1, \ldots, N_f\}$. Furthermore, Lc stands for the linear combinations given in eqs. (6.2.32) to (6.2.35), and the second column gives the number of real or imaginary components for each type of ISS scalar mass eigenstates.

In [161] massless Goldstone modes were predicted to exist. In our analysis this would correspond to both $\text{Re}Q_4$ and $\text{Im}Q_4$ as well as to $\text{Im}Q_2$. At tree level, one is unable to notice that $\text{Re}Q_2$ is actually a pseudo-Goldstone whose mass is given by higher order corrections, as we comment next. The reason why the scalar mass spectrum yields $N^2 + 2\left(N_f - N\right) = 2N_f N - N^2$ massless bosons is that the VEVs of q, $\tilde{q}$ break the original symmetry $SU\left(N\right) \times SU\left(N_f\right)_V \times U\left(1\right)_B$ with $N^2 + N_f^2 + 1$ generators into $SU\left(N\right)_V \times SU\left(N_f - N\right)_V \times U\left(1\right)_{B'}$ with $N^2 + \left(N_f - N\right)^2 - 1$ generators, where $SU\left(N_f\right)_V$ breaks into $SU\left(N\right)_V \times SU\left(N_f - N\right)_V \times U\left(1\right)_{B'}$, whereas the original $SU\left(N\right) \times U\left(1\right)_B$ is completely broken since, in the region $i \otimes a = N^2$, there exists Q_2 with null VEV. Furthermore, the S field transforming as a singlet under $SU\left(N_f\right)_V$ gives no contribution to the massless Goldstone mode analysis.

As to quantum corrections to the masses, we recall that one-loop calculations in [161] generate an additional $\mathcal{O}\left(m_{3/2}\frac{M_P}{M}\right)$ mass to the real and imaginary parts of S_2' (a subset

of S_2, namely S_{ij} with indices $i,\, j > N$) as well as to the real part of Q_2. More precisely,

$$\begin{aligned} e^{K/2} m_{S_2'}^{\text{1-loop}} &= e^{K/2} \left(\frac{\ln(4) - 1}{8\pi^2} \right)^{1/2} \sqrt{N} h^2 M \\ &= \left(\frac{3\,(\ln(4) - 1)}{8\pi^2} \right)^{1/2} \sqrt{\frac{N}{N_f - N}} h \left(\frac{M_{\text{p}}}{M} \right) m_{3/2} \quad , \end{aligned} \tag{6.2.36}$$

$$\begin{aligned} e^{K/2} m_{Q_2}^{\text{1-loop}} &= e^{K/2} \left(\frac{\ln(4) - 1}{8\pi^2} \right)^{1/2} \sqrt{N_f - N} h^2 M \\ &= \left(\frac{3\,(\ln(4) - 1)}{8\pi^2} \right)^{1/2} h \left(\frac{M_{\text{p}}}{M} \right) m_{3/2} \quad . \end{aligned} \tag{6.2.37}$$

Since $M \ll M_{\text{P}}$, we can safely consider the one-loop contribution to yield the mass of the real and imaginary components of S_2', as well as of the real component of Q_2.

For a better understanding of the mass matrices for the ISS fields S and Q after diagonalization, we display them below in a diagramatic form.

$$S = \left(\begin{array}{c|c} (S_1)_{N\times N} & \left(S_2^{\text{nd}}\right)_{N\times(N_f-N)} \\ \hline \left(S_2^{\text{nd}}\right)_{(N_f-N)\times N} & \left(S_2'\right)_{(N_f-N)\times(N_f-N)} \end{array} \right) \quad , \tag{6.2.38}$$

$$Q = \left(\begin{array}{c|c} (Q_1 \,\&\, Q_2)_{N\times N} & (Q_3 \,\&\, Q_4)_{N\times(N_f-N)} \end{array} \right) \quad . \tag{6.2.39}$$

Here we see the splitting of S_2 into non-diagonal pieces $\left(S_2^{\text{nd}}\right)_{N\times(N_f-N)}$, $\left(S_2^{\text{nd}}\right)_{(N_f-N)\times N}$ and the subset S_2' which receives mass through one-loop calculations beyond its tree-level mass of $\mathcal{O}\left(m_{3/2}\right)$ as presented above. Additionally, we see that Q_1 and Q_2 as well as Q_3 and Q_4 mix in the block forms sketched above. The indices here refer to the size of the cartesian product set.

A further comment is in order. When one considers the ISS model alone, the VEVs (6.2.22), (6.2.23) and (6.2.24). However, when the modulus field ρ contribution is included, i.e. $W_{\text{KL}} = \Delta$, the first derivatives of the ISS fields change according to

$$\frac{\partial V_{\text{KL-ISS}}}{\partial\,(q, \tilde{q})_{ia}} = \mathcal{O}\left(m_{3/2}^2 M_{\text{P}} \langle q, \tilde{q} \rangle_{ia}\right) \quad , \tag{6.2.40}$$

$$\frac{\partial V_{\text{KL-ISS}}}{\partial S_{ij}} = \mathcal{O}\left(m_{3/2}^2 M_{\text{P}}\right) \quad . \tag{6.2.41}$$

To cancel these effects, the VEVs of q_{ia}, $\tilde{q}_{ai}$ and S_{ij} (assuming the VEVs to be diagonal)

should obtain corrections. This is translated as

$$\begin{aligned}
\langle q_{ia}, \tilde{q}_{ai} \rangle &= \left(M - \mathcal{O}\left(M^3 M_{\rm P}^{-2}\right)\right) \delta_{ia} \quad , && (6.2.42)\\
\langle S_{ij} \rangle &= \left(\left(\frac{M}{M_{\rm P}}\right)^2 M_{\rm P} + \mathcal{O}\left(M^4 M_{\rm P}^{-3}\right) \right) \delta_{ij} \quad \text{for} \quad i,j \leq N \quad , && (6.2.43)\\
\langle S_{ij} \rangle &= \left(\frac{16\pi^2 \left(N_f - N\right)}{3\left(\ln\left(4\right) - 1\right) N h^2} \left(\frac{M}{M_{\rm P}}\right)^2 M_{\rm P} + \mathcal{O}\left(M^4 M_{\rm P}^{-3}\right) \right) \delta_{ij} && (6.2.44)\\
&\simeq \left(\frac{\left(N_f - N\right)}{3N} \frac{408.79}{h^2} \left(\frac{M}{M_{\rm P}}\right)^2 M_{\rm P} + \mathcal{O}\left(M^4 M_{\rm P}^{-3}\right) \right) \delta_{ij} \quad \text{for} \quad i,j > N \quad .
\end{aligned}$$

The last correction is dominated by one-loop contributions. Notice that these corrections cancel the term $2NM^2$ in eq. (6.2.27).

An observation about the sign of Δ must be made. When we calculate the modified VEVs, written in the last set of eqs., one must assume either that $h < 0$ or $\Delta < 0$ for the equation $\partial V_{\text{KL-ISS}}/\partial \phi_{\rm ISS}$ to vanish. We decide to restrain the sign freedom of Δ and take it to be negative, while opting for $h > 0$.

- The ISS fermion fields $\chi_{\phi_{\rm ISS}}$

We now present the masses and eigenstates of the fermionic parts of the ISS superfields.

For $i \otimes a \in N^2$ and $i \otimes j \in N^2$, for $i = a$ and $i = j$, the eigenstates are

$$\begin{aligned}
\chi_{B1} &= \frac{1}{\sqrt{5}} \left(2^{1/2} \chi_{ai} + 2^{1/2} \tilde{\chi}_{ia} + \chi_{ij}\right) + \mathcal{O}\left(M\right) && (6.2.45)\\
\chi_{B2} &= \frac{1}{\sqrt{5}} \left(2^{1/2} \chi_{ai} + 2^{1/2} \tilde{\chi}_{ia} - \chi_{ij}\right) + \mathcal{O}\left(M\right) && (6.2.46)\\
\chi_{S1} &= 2^{-1/2} \left(\chi_{ai} - \tilde{\chi}_{ia}\right) && (6.2.47)
\end{aligned}$$

For $i \neq a$ and $i \neq j$, one finds

$$\begin{aligned}
\chi_{S3} &= \frac{1}{2} \left(\chi_{i>a} + \tilde{\chi}_{a<i} - \chi_{i<a} - \tilde{\chi}_{a>i}\right) && (6.2.48)\\
\chi_{S4} &= \frac{1}{2} \left(\chi_{i>a} - \tilde{\chi}_{a<i} + \chi_{i<a} - \tilde{\chi}_{a>i}\right) && (6.2.49)\\
\chi_{B3} &= \frac{1}{2\sqrt{2}} \left(\chi_{i>a} - \tilde{\chi}_{a<i} - \chi_{i<a} + \tilde{\chi}_{a>i} - \sqrt{2}\chi_{i<j} + \sqrt{2}\chi_{i>j}\right) + \mathcal{O}\left(M\right) && (6.2.50)\\
\chi_{B4} &= \frac{1}{2\sqrt{2}} \left(\chi_{i>a} + \tilde{\chi}_{a<i} + \chi_{i<a} + \tilde{\chi}_{a>i} - \sqrt{2}\chi_{i<j} - \sqrt{2}\chi_{i>j}\right) + \mathcal{O}\left(M\right) && (6.2.51)\\
\chi_{B5} &= \frac{1}{2\sqrt{2}} \left(\chi_{i>a} - \tilde{\chi}_{a<i} - \chi_{i<a} + \tilde{\chi}_{a>i} + \sqrt{2}\chi_{i<j} - \sqrt{2}\chi_{i>j}\right) + \mathcal{O}\left(M\right) && (6.2.52)\\
\chi_{B6} &= \frac{1}{2\sqrt{2}} \left(\chi_{i>a} + \tilde{\chi}_{a<i} + \chi_{i<a} + \tilde{\chi}_{a>i} + \sqrt{2}\chi_{i<j} + \sqrt{2}\chi_{i>j}\right) + \mathcal{O}\left(M\right) && (6.2.53)
\end{aligned}$$

For example, if $N = 2$, we have $\left(\chi_{S3}\right)_{N=2} = \frac{1}{2}\left(\chi_{21} + \tilde{\chi}_{12} - \chi_{12} - \tilde{\chi}_{21}\right)$, and similarly for

the other states. For $i \otimes a \in N_f N - N^2$ and $i \otimes j \in N_f^2 - N^2$, the mass eigenstates are

$$\begin{aligned} \chi_{M1} &= 2^{-1/2}\left(\chi_{ia} - \tilde{\chi}_{ai}\right) && (6.2.54)\\ \chi_{M2} &= 2^{-1/2}\left(\chi_{ia} + \tilde{\chi}_{ai}\right) && (6.2.55)\\ \chi_{S2} &= \chi_{ij} \quad , \text{ for } i \neq j && (6.2.56)\\ &= 2^{-1/2}\left(\chi_{qq} - \chi_{ij}\right) \quad , \text{ for } i = j && (6.2.57) \end{aligned}$$

where $q \equiv N+1$. As an example, for $N=2$ and $N_f=5$ and $i=j$, we obtain the possibilities $\chi_{S2} = \left\{\frac{1}{\sqrt{2}}\left(\chi_{33}-\chi_{44}\right), \frac{1}{\sqrt{2}}\left(\chi_{33}-\chi_{55}\right)\right\}$. The Goldstino has already been subtracted out and is given by

$$\chi_{\text{Goldstino}} = \frac{1}{\sqrt{N_f - N}} \sum_{i=1}^{N_f - N} \chi_{ii} + \mathcal{O}\left(M^2\right) \qquad (6.2.58)$$

Regarding the masses of the above eigenstates, the main contribution stems from the term $\left(e^{G/2}\frac{W_{ij}}{W}\right)\bar{\chi}_R\chi_L + \text{h.c.}$. Their mass values are written in tables 6.2 and 6.3.

ISS fermion mass eigenstate	Number	Mass
$\chi_{B1} \equiv \text{Lc}\left[q_{ai}, \tilde{q}_{ia}\right]\left(i \otimes a \in N^2\right)$	N	$\sqrt{\frac{6}{N_f - N}}\left(\frac{M_P}{M}\right) m_{3/2}$
$\chi_{B2} \equiv \text{Lc}\left[S_{ij}, q_{ai}, \tilde{q}_{ia}\right]\left(i \otimes a \in N^2, i \otimes j \in N^2\right)$	N	$\sqrt{\frac{6}{N_f - N}}\left(\frac{M_P}{M}\right) m_{3/2}$
$\chi_{S1} \equiv \text{Lc}\left[S_{ij}, q_{ai}, \tilde{q}_{ia}\right]\left(i \otimes a \in N^2, i \otimes j \in N^2\right)$	N	$m_{3/2}$
$\chi_{S3} \equiv \text{Lc}\left[q_{ai}, \tilde{q}_{ia}\right]\left(i \otimes a \in N^2\right)$	$N\left(N-1\right)/2$	$m_{3/2}$
$\chi_{S4} \equiv \text{Lc}\left[q_{ai}, \tilde{q}_{ia}\right]\left(i \otimes a \in N^2\right)$	$N\left(N-1\right)/2$	$m_{3/2}$
$\chi_{B3} \equiv \text{Lc}\left[S_{ij}, q_{ai}, \tilde{q}_{ia}\right]\left(i \otimes a \in N^2, i \otimes j \in N^2\right)$	$N\left(N-1\right)/2$	$\sqrt{\frac{6}{N_f - N}}\left(\frac{M_P}{M}\right) m_{3/2}$
$\chi_{B4} \equiv \text{Lc}\left[S_{ij}, q_{ai}, \tilde{q}_{ia}\right]\left(i \otimes a \in N^2, i \otimes j \in N^2\right)$	$N\left(N-1\right)/2$	$\sqrt{\frac{6}{N_f - N}}\left(\frac{M_P}{M}\right) m_{3/2}$
$\chi_{B5} \equiv \text{Lc}\left[S_{ij}, q_{ai}, \tilde{q}_{ia}\right]\left(i \otimes a \in N^2, i \otimes j \in N^2\right)$	$N\left(N-1\right)/2$	$\sqrt{\frac{6}{N_f - N}}\left(\frac{M_P}{M}\right) m_{3/2}$
$\chi_{B6} \equiv \text{Lc}\left[S_{ij}, q_{ai}, \tilde{q}_{ia}\right]\left(i \otimes a \in N^2, i \otimes j \in N^2\right)$	$N\left(N-1\right)/2$	$\sqrt{\frac{6}{N_f - N}}\left(\frac{M_P}{M}\right) m_{3/2}$

Table 6.2: Tree-level largest contributions to the masses of the ISS fermion eigenstates within the index space $i \otimes a \in N^2$ and $i \otimes j \in N^2$. The notations $i \otimes a$ and $i \otimes j$ are of the same kind as the ones for the ISS scalar masses table 6.1. Furthermore, Lc stands for the linear combinations given from eqs. (6.2.45) to (6.2.53), and the second column gives the number of each type of ISS fermion mass eigenstate in the considered index space.

We should write some words in respect to the generation of soft terms via F-term SUSY breaking from the ISS sector and the resulting particle spectrum. This has been analyzed extensively in [162]. In general, for models with strong moduli stabilization, the generated A-terms and the gaugino masses are very small at tree level. This happens because, for example $\bar{S}\overline{D}_{\bar{S}}\overline{W}_{\text{KL-ISS}} \propto M^2 W_{\text{ISS}} \ll W_{\text{ISS}}$ (and similar terms with respect to q and $\tilde{q}$), and the strong condition $D_\rho W_{\text{KL-ISS}} \ll W_{\text{KL-ISS}}$ after SUSY breaking.

Indeed the tree-level value for A is $A \propto \frac{m_{3/2}}{m_\rho} m_{3/2} \ll m_{3/2}$ since $m_\rho \gg m_{3/2}$. Furthermore, the condition $D_\rho W_{\text{KL-ISS}} \ll W_{\text{KL-ISS}}$ and $m_\rho \gg m_{3/2}$ also imply that the gaugino

ISS fermion mass eigenstate	Number	Mass
$\chi_{M1} \equiv \mathrm{Lc}\left[q_{ai}, \tilde{q}_{ia}\right]\left(i \otimes a \in N_f^2 - N^2\right)$	$N\left(N_f - N\right)$	$\frac{16\pi^2}{(\ln[4]-1)h^2} m_{3/2}$
$\chi_{M2} \equiv \mathrm{Lc}\left[q_{ai}, \tilde{q}_{ia}\right]\left(i \otimes a \in N_f^2 - N^2\right)$	$N\left(N_f - N\right)$	$\frac{16\pi^2}{(\ln[4]-1)h^2} m_{3/2}$
$\chi_{S2} \equiv \mathrm{Lc}\left[S_{ij}\right]\left(i \otimes a \in N_f^2 - N^2\right)$	$N_f^2 - N^2 - 1$	0

Table 6.3: Tree-level largest contributions to the masses of the ISS fermion eigenstates within the index space $i \otimes a \in N_f N - N^2$ and $i \otimes j \in N_f^2 - N^2$. The notations $i \otimes a$ and $i \otimes j$ are of the same kind as the ones for the ISS scalar masses table 6.1. Furthermore, Lc stands for the linear combinations given from eqs. (6.2.54) to (6.2.57), and the second column gives the number of each type of ISS fermion mass eigenstate in the considered index space.

masses are undesirably small, namely $m_{1/2} \propto \frac{m_{3/2}}{m_\rho} m_{3/2} \partial_\rho \ln h_A \ll m_{3/2}$, where h_A denotes the gauge kinetic functions. Therefore, one should apply a one-loop level calculation to generate both A-terms and gaugino masses, resembling anomaly mediated models. For acceptable gaugino masses, $m_{3/2}$ is forced to assume high values $\mathcal{O}\left(10 - 1000 \text{ TeV}\right)$ in order to compensate for suppressed loop pre-factors. The resulting spectrum then resembles split supersymmetry, with light gaugino masses and soft scalar masses of $\mathcal{O}\left(m_{3/2}\right)$.

Decay rates

Here we discuss the interaction terms of the ISS fields to the MSSM fields, as well as to the ISS fields themselves. More specifically, we provide the largest decay rates of the ISS scalars real parts, since the ISS scalar imaginary parts do not oscillate after inflation and therefore do not contribute significantly at that stage. The decay rates $\Gamma^i_{\mathrm{Re}\phi_{\mathrm{ISS}}}$ of each $\mathrm{Re}\phi_{\mathrm{ISS}}$ play a very important role in the following sections 6.2.3 and 6.2.4.

If $\Gamma_{\phi^i_{\mathrm{ISS}}}$ is sufficiently small, the ISS fields decay quite late, well after inflaton decays reheat the universe. The ISS fields must decay before the onset of BBN in order not to jeopardize the successful BBN predictions of the Standard Model. Note that not only the ISS fields themselves but also their decay products should decay before the onset of BBN.

ISS fields decaying well before BBN may release a large amount of entropy. In fact, some versions of Affleck-Dine baryogenesis [171, 172] require a lot of late entropy production in order to yield a baryon asymmetry that matches the asymmetry observed today, $n_B - n_{\bar{B}}/s_0 \sim 10^{-10}$. However, baryogenesis can also be accomplished for a small ISS entropy production through the mechanisms given in e.g. [173, 174]. In this work, we will consider the latter option. We thus require that the decay of the ISS fields release less entropy than inflaton decays do; this minimizes the difference between our scenario and standard cosmology.

To compute the decay rates, we considered both two-body decays ($\phi_{\mathrm{ISS}} \to 1 + 2$) and

three-body decays ($\phi_{\rm ISS} \to 1+2+3$),[6] and used the following expressions

$$\frac{d\overline{\Gamma}^{12}_{\phi_{\rm ISS}}}{d\Omega_{\rm CM}} = \frac{\left|\overline{\mathcal{M}}^{12}_{\phi_{\rm ISS}}\right|^2}{64\pi^2}\frac{S_{12}}{m^3_{\phi_{\rm ISS}}}S \quad , \tag{6.2.59}$$

$$\overline{\Gamma}^{123}_{\phi_{\rm ISS}} = \frac{1}{m_{\phi_{\rm ISS}}64\pi^3}\int_0^{\frac{m_{\phi_{\rm ISS}}}{2}} dE_2 \int_{\frac{m_{\phi_{\rm ISS}}}{2}-E_2}^{\frac{m_{\phi_{\rm ISS}}}{2}} dE_1 \left|\overline{\mathcal{M}}^{123}_{\phi_{\rm ISS}}\right|^2 \quad , \tag{6.2.60}$$

where $\mathrm{d}\Omega_{\rm CM}$ is the phase space differential element, $\overline{\mathcal{M}}^{12}_{\phi_{\rm ISS}}$ $\left(\overline{\mathcal{M}}^{123}_{\phi_{\rm ISS}}\right)$ is the amplitude (summed over helicity states, thus the 'overline') of the two(three)-body decay. $S_{12} = \left[m^2_{\phi_{\rm ISS}} - (m_1-m_2)^2\right]^{1/2}\left[m^2_{\phi_{\rm ISS}} - (m_1+m_2)^2\right]^{1/2}$, $m_{\phi_{\rm ISS}}$ is the mass of the decaying ISS scalar, s is the symmetry factor for indistinguishable final states. Since the ISS fields are much heavier[7] than their decay products, we consider all final particles to be massless for simplicity.

Before writing the results for the decay rates, we must comment on an important detail. Within the set $(q, \tilde{q})$, we will write the decay rates for $\mathrm{Re}Q_1$ and $\mathrm{Re}Q_2$. Despite the oscillation amplitude of the latter being zero, its decay rate is important since it is a decay product of $\mathrm{Re}Q_1$ itself. For the set S, we write the decay rates for $\mathrm{Re}S_1$ and $\mathrm{Re}S_2$, which have non-vanishing oscillation amplitudes after inflation.

For a complete list of possible decay rates, we refer the reader to the ref. [157], where we calculated the decay rates of the ISS fields into different channels. For final MSSM and/or ISS particles, we studied: two or three scalars; two fermions; two fermions plus one scalar; two gauginos or two gauge bosons. Also decay rates for two final gravitinos were evaluated.

Assuming $N = 1$ and $N_f = 4$, we observe the largest contributions to the total decay rates of the ISS fields originate from their decays to

- gravitinos via $(S_2, Q_1, Q_2) \to \psi_{3/2} + \psi_{3/2}$;
- two ISS fermions via $S_1 \to \bar{\chi}_{S1} + \chi_{S1}$;
- and two ISS fermions plus one ISS scalar via both $Q_1 \to \bar{\chi}_{S1} + \chi_{S1} + \{\mathrm{Re}Q_2, \mathrm{Im}Q_2\}$ and $Q_2 \to \bar{\chi}_{S1} + \chi_{S1} + \mathrm{Im}Q_2$.

[6] To write the decay rates of $\mathrm{Re}\phi_{\rm ISS}$, we use for convenience the symbol $\phi_{\rm ISS}$ rather than $\mathrm{Re}\phi_{\rm ISS}$ for the real ISS scalars parts.

[7] Exceptions are the fields $\mathrm{Im}Q_2$ and Q_4. However we will see later that these fields do not oscillate after inflation, thus they do not yield important contributions to the energy content of the universe, at least before the ISS oscillating fields decay, after which $\mathrm{Im}Q_2$ and Q_4 might emerge and carry a fraction of energy from the before-oscillating fields.

Put in another way, we have

$$\Gamma_{S_1}^{\text{total}} \simeq \overline{\Gamma}_{S_1}^{\chi\chi} \quad , \tag{6.2.61}$$

$$\Gamma_{S_2}^{\text{total}} \simeq \overline{\Gamma}_{S_2}^{2\psi_{3/2}} \quad , \tag{6.2.62}$$

$$\Gamma_{Q_1}^{\text{total}} \simeq \overline{\Gamma}_{Q_1}^{2\psi_{3/2}} + \overline{\Gamma}_{Q_1}^{\chi\chi\text{Re}Q_2} + \overline{\Gamma}_{Q_1}^{\chi\chi\text{Im}Q_2} \quad , \tag{6.2.63}$$

$$\Gamma_{Q_2}^{\text{total}} \simeq \overline{\Gamma}_{Q_2}^{2\psi_{3/2}} + \overline{\Gamma}_{Q_2}^{\chi\chi\text{Im}Q_2} \quad . \tag{6.2.64}$$

Notice the notation Q_1, Q_2, S_1, S_2 instead of $\text{Re}Q_1$, $\text{Re}Q_2$, $\text{Re}S_1$, $\text{Re}S_2$ for the initial states. χ stands for χ_{S1} or $\bar{\chi}_{S1}$, appearing in pairs. The partial decay rates are given by

$$\overline{\Gamma}_{S_1}^{\chi\chi} \simeq 5.63 \cdot 10^{-2} \frac{m_{3/2}^3}{M_{\text{P}}^2} \left(\frac{M_{\text{P}}}{M}\right)^5 \quad , \tag{6.2.65}$$

$$\overline{\Gamma}_{S_2}^{2\psi_{3/2}} \simeq 2.31 \cdot 10^{-9} \frac{m_{3/2}^3 h^5}{M_{\text{P}}^2} \left(\frac{M_{\text{P}}}{M}\right)^5 \quad , \tag{6.2.66}$$

$$\overline{\Gamma}_{Q_1}^{2\psi_{3/2}} \simeq 3.13 \cdot 10^{-3} \frac{m_{3/2}^3}{M_{\text{P}}^2} \left(\frac{M_{\text{P}}}{M}\right)^3 \quad , \tag{6.2.67}$$

$$\overline{\Gamma}_{Q_1}^{\chi\chi\text{Re}Q_2}, \overline{\Gamma}_{Q_1}^{\chi\chi\text{Im}Q_2} \simeq 4.90 \cdot 10^{-11} \frac{m_{3/2}^3 h^2}{M_{\text{P}}^2} \left(\frac{M_{\text{P}}}{M}\right)^5 \quad , \tag{6.2.68}$$

$$\overline{\Gamma}_{Q_2}^{2\psi_{3/2}} \simeq 1.44 \cdot 10^{-8} \frac{m_{3/2}^3 h^5}{M_{\text{P}}^2} \left(\frac{M_{\text{P}}}{M}\right)^3 \quad , \tag{6.2.69}$$

$$\overline{\Gamma}_{Q_2}^{\chi\chi\text{Im}Q_2} \simeq 2.57 \cdot 10^{-14} \frac{m_{3/2}^3 h^5}{M_{\text{P}}^2} \left(\frac{M_{\text{P}}}{M}\right)^5 \quad . \tag{6.2.70}$$

The decay rates of the remaining products, $\psi_{3/2}$ and χ_{S1}, are discussed now. The gravitino decay rate is given by [175]

$$\overline{\Gamma}_{3/2}\left(\psi_{3/2} \to \text{MSSM}\right) = \frac{193}{384\pi} \frac{m_{3/2}^3}{M_{\text{P}}^2} \quad . \tag{6.2.71}$$

The gravitino decays predominantly into R-parity even MSSM particle and its supersymmetric partner[8], since its R-parity is $R = -1$ [176]. We assumed that $m_{3/2} \gg m_{\text{MSSM}}$ with m_{MSSM} being the mass of any MSSM particle. The factor $\frac{193}{384\pi}$ counts the number of MSSM gaueg bosons, fermions (leptons and quarks) and Higgs scalars. More specifically, we have the following relation $\frac{193}{384\pi} = \frac{1}{384\pi}\left(12_{\text{prefactor}}^{\text{gauge}} \cdot 12_{\text{gauge}} + 3_{\text{families}} \cdot 15_{\text{fermions}} + 4_{\text{Higgs}}\right)$. The χ_{S1} decay rate,

$$\overline{\Gamma}_{\chi_{S1}}\left(\chi_{S1} \to \text{Im}Q_2 + \chi_{\text{MSSM}} + \phi_{\text{MSSM}}\right) = 2.38 \cdot 10^{-4} \frac{m_{3/2}^5}{M_{\text{P}}^4} \tag{6.2.72}$$

$$\simeq 1.12 \cdot 10^{-8} \frac{m_{3/2}^3}{M_{\text{P}}^2} h^2 \left(\frac{M}{M_{\text{P}}}\right)^4 \quad , \tag{6.2.73}$$

[8] The decay channels are given by $\psi_{3/2} \to \lambda + A_m$, $\psi_{3/2} \to \phi_m + \bar{\chi}_m$, $\psi_{3/2} \to \phi_m^* + \chi_m$, where λ are gauginos, A_m are gauge bosons, ϕ_m are scalars, and χ_m are left-handed fermions.

is obtained from the term $e^{G/2}\left(1/3\left(K_{q_{ia}}+K_{\bar{q}_{ia}}\right)K_{\mathrm{MSSM}}\right)\bar{\chi}_R^{ia}\chi_L^{\mathrm{MSSM}}$within the scalar potential. Again $m_{3/2}\gg m_{\mathrm{MSSM}}$ was assumed, and the counting over the scalars and fermions has been done, i.e. $49=3\cdot 15+4$, and over the contribution from the GM term, which yields $2c_H\equiv 2$.

The latter decay rate is smaller than the gravitino's and can pose problems to BBN if the lifetime of χ_{S1} exceeds ~ 1 second, or temperature $T\sim 1$ MeV. This will be dealt with in secs. 6.2.3 and 6.2.4, where we obtain constraints on h and M imposed by entropy dilution and dark matter production.

6.2.3 Post inflation dynamics and entropy production

So far we have shown the masses for the relevant fields considered in this work (the modulus, the gravitino and the ISS fields), as well as the largest ISS decay rates. In this section, we set these masses and decay rates against the constraints of small entropy dilution.

Oscillations

We start with a detailed study os oscillations from the inflaton η and the ISS fields $\mathrm{Re}\phi_{\mathrm{ISS}}$. We determine which of the ISS fields are relevant for the subsequent analysis and discuss the decay epochs of η and the relevant $\mathrm{Re}\phi_{\mathrm{ISS}}$, together with entropy constraints.

The procedure is to study possible modifications to the ISS model due to the inflaton field (which has been neglected in our analysis so far), in comparison with the situtation of the ISS fields after inflation has already occurred.

Recall the VEVs of the ISS fields without contributions from the inflaton η (eqs. (6.2.42), (6.2.43) and (6.2.44))

$$\begin{aligned}\langle q_{ia},\tilde{q}_{ai}\rangle &\simeq M\delta_{ia} \quad ,\\ \langle S_{ij}\rangle &\simeq \left(\frac{M}{M_{\mathrm{P}}}\right)^2 M_{\mathrm{P}}\delta_{ij} \quad \text{for} \quad i,j\leq N \quad ,\\ \langle S_{ij}\rangle &\simeq \frac{(N_f-N)}{3N}\frac{408.79}{h^2}\left(\frac{M}{M_{\mathrm{P}}}\right)^2 M_{\mathrm{P}}\delta_{ij} \quad \text{for} \quad i,j>N \quad .\end{aligned} \tag{6.2.74}$$

We now add contributions from the inflaton, which means that we introduce the following term to the ISS scalar potential [172, 177, 178]

$$\Delta V\left(\phi_{\mathrm{ISS}},\bar{\phi}_{\mathrm{ISS}}\right)\sim e^{K\left(\phi_{\mathrm{ISS}},\bar{\phi}_{\mathrm{ISS}}\right)}V\left(\eta\right)=cH^2\phi_{\mathrm{ISS}}\bar{\phi}_{\mathrm{ISS}}+\cdots \quad , \tag{6.2.75}$$

where H is the Hubble parameter, and generically $c=3$ for $K_{\mathrm{ISS}}=\phi_{\mathrm{ISS}}\bar{\phi}_{\mathrm{ISS}}$ [178], which is the case for the fields $\{S_{ij},\, q_{ia},\tilde{q}_{ai}\}$, eq. (6.2.11). The effect of $\Delta V\left(\phi_{\mathrm{ISS}},\bar{\phi}_{\mathrm{ISS}}\right)$ is to make the VEVs during inflation, which we define as $\langle S_{ij}\rangle_{\mathrm{ins}}$, $\langle q_{ia}\rangle_{\mathrm{ins}}$ and $\langle\tilde{q}_{ai}\rangle_{\mathrm{ins}}$, to assume smaller values compared with their true minimum given in eq. (6.2.74), which we call

from now on $\langle S_{ij}\rangle_{\rm min}$, $\langle q_{ia}\rangle_{\rm min}$ and $\langle \tilde{q}_{ai}\rangle_{\rm min}$. In fact, one obtains for S

$$\langle S_{ij}\rangle_{\rm ins} \simeq \langle S_{ij}\rangle_{\rm min}\left(1+\frac{cH^2}{2h^2M^2}\right)^{-1} \simeq \frac{2h^2M^4}{cH^2M_{\rm P}} \ll \langle S_{ij}\rangle_{\rm min} \quad \text{for} \quad i,j \leq N \quad , \tag{6.2.76}$$

$$\langle S_{ij}\rangle_{\rm ins} \simeq \langle S_{ij}\rangle_{\rm min}\left(1+\frac{8\pi^2cH^2}{(\ln(4)-1)\,h^4M^2}\right)^{-1} \simeq \frac{2h^2M^4}{cH^2M_{\rm P}} \ll \langle S_{ij}\rangle_{\rm min} \quad \text{for} \quad i,j > N \quad . \tag{6.2.77}$$

We have assumed high-scale inflation in these equations, i.e. $H \gg M$. And for q and $\tilde{q}$, it yields

$$\langle q_{ia}, \tilde{q}_{ai}\rangle_{\rm ins} \simeq \begin{cases} \frac{1}{h}\sqrt{h^2M^2-cH^2} & \text{for} \quad cH^2 \leq h^2M^2\,, \\ 0 & \text{for} \quad cH^2 > h^2M^2\,. \end{cases} \tag{6.2.78}$$

The $\langle S_{ij}\rangle_{\rm ins}$ and $\langle q_{ia}, \tilde{q}_{ai}\rangle_{\rm ins}$ now evolve into the direction of the minima $\langle S_{ij}\rangle_{\rm min}$ and $\langle q_{ia}, \tilde{q}_{ai}\rangle_{\rm min}$.

A comment can be done. The inflaton potential introduces the mass contribution $cH^2\phi_{\rm ISS}\bar{\phi}_{\rm ISS}$ to the ISS fields, which yields a mass $\sim \sqrt{c}H$ for all the ISS fields during inflation ($H \gg M$), including the mass of the Goldstone modes ImQ_2, ReQ_4 and ImQ_4. Although the S_{ij} retain a small VEV, it cannot keep the Goldstone particles from being massive.

Now take some generic field φ. The fields φ that start oscillating after inflation are the ones which possess a non-vanishing difference between the VEV during inflation $\langle\varphi\rangle_{\rm ins}$ and the VEV well after inflation $\langle\varphi\rangle_{\rm min}$, i.e.

$$\langle\varphi\rangle_{\rm amp} = |\langle\varphi\rangle_{\rm ins} - \langle\varphi\rangle_{\rm min}| \neq 0 \quad . \tag{6.2.79}$$

From this observation, we notice there are N_f oscillating fields in the S_{ij} sector, N for $i\,j \leq N$ and $(N_f - N)$ for $i, j > N$. The linear combinations responsible for their oscillations are ReS_1 and ReS_2. Furthermore, assuming that q and $\tilde{q}$ have the same VEV due to their symmetric placement within the superpotential, there are no oscillations for ReQ_2 due to its definition given by eq. (6.2.33). Since Q_3 and Q_4 are defined in the region $i \leq N$ and $N < a \leq N_f$, they do not contribute with oscillations due to (6.2.74), (6.2.34) and (6.2.35). Thus, there are only N oscillating fields from q and $\tilde{q}$, corresponding to the mass eigenstate ReQ_1.

After the end of inflation, η starts to osccillate about its true minimum [178–180] and, since it dominate the energy density of the univrse, this constitutes a matter-dominated period. The energy density of the inflaton η and the Hubble parameter after inflation are given by

$$\rho_\eta = \frac{1}{2}m_\eta^2\eta^2 = \frac{1}{2}m_\eta^2\langle\eta\rangle_{\rm amp}^2\left(\frac{R_\eta}{R}\right)^3 = \frac{4}{3}m_\eta^2M_P^2\left(\frac{R_\eta}{R}\right)^3 \quad , \tag{6.2.80}$$

$$H = \sqrt{\frac{1}{M_P^2}\frac{\rho}{3}} = \frac{2}{3}m_\eta\left(\frac{R_\eta}{R}\right)^{3/2} \quad . \tag{6.2.81}$$

Here we take the inflaton amplitude to $\langle\eta\rangle_{\rm amp} = \langle\eta\rangle_{\rm ins} = \sqrt{8/3}M_{\rm P}$ after inflation because $\langle\eta\rangle_{\rm min} = 0$ now. Furthermore, R denotes the cosmological scale factor of the FLRW metric, and R_η denotes the cosmological scale factor at the onset of the η oscillations.

The post-inflationary oscillation amplitude of the modulus ρ yields $\langle\rho\rangle_{\rm amp} = 0$ since $\langle\rho\rangle_{\rm ins} = \langle\rho\rangle_{\rm min}$. As a matter of fact, the inflaton and the modulus (following discussion after eq. (6.2.31)) decouple, which means that the ρ VEV during and after inflation are the same. The evolution of ρ will thus be neglected.

Within the matter-dominated period after inflation with oscillations from η, the Hubble parameter decreases to the point where $\langle q_{ia}, \tilde{q}_{ai}\rangle_{\rm ins} > 0$. When this happens, the ISS fields q and $\tilde{q}$ adiabatically track their instantaneous minimum[9] (6.2.78) [178–180] until they reach the point where $H \sim m_\varphi$ where they start damped oscillations about their true minimum (6.2.74).

To understand the relation of the Hubble parameter with the mass of φ and the beginning of oscillations, we recall the equation for the time evolution of the generic field φ:

$$\ddot{\varphi} + 3H\dot{\varphi} + m_\varphi^2\left(\varphi - \varphi_{\rm min}\right) = 0 \quad , \tag{6.2.82}$$

where m_φ is the φ mass (the third term stems solely from the φ mass term, i.e. no interactions are assumed). Solving the differential equation, it yields

$$\varphi(t) = \varphi_{\rm min} - e^{-\frac{3}{2}Ht}\left(C_1\, e^{-\sqrt{f}\,t} + C_2\, e^{\sqrt{f}\,t}\right) \quad , \tag{6.2.83}$$

where $f = f(H, m_\chi) = 9H^2 - 4m_\chi^2$; $C_1 = \varphi_i \cdot \left(-3H + \sqrt{f}\right)\left(2\sqrt{f}\right)^{-1}$ and $C_2 = \varphi_i \cdot \left(3H + \sqrt{f}\right)\left(2\sqrt{f}\right)^{-1}$ are determined by the initial conditions $\varphi(0) = \varphi_{\rm min} - \varphi_i$ and $\dot{\varphi}(0) \simeq 0$, where $t = 0$ is defined at the beginning of φ oscillations. If $f > 0$, the field behaves as $\varphi - \varphi_{\rm min} \sim -e^{-\alpha t}$ where $\alpha > 0$. If $f < 0$, we have $\varphi = \varphi_{\rm min} - \varphi_i \cdot e^{-\frac{3}{2}Ht}\left(\cos\left(\left|\sqrt{f}\right|t\right) + i\frac{3H}{\sqrt{f}}\sin\left(\left|\sqrt{f}\right|t\right)\right)$, where its behaviour is oscillatory with an effective amplitude $\varphi_i \cdot e^{-\frac{3}{2}Ht}$ that decreases with time. As it is clear, at $f \simeq 0$ the field turns quite high since the 'sine' term explodes. Also we note that right at $f = 0 \therefore H = \frac{2}{3}m_\varphi$ the term φ_i (roughly at the end of inflation) is approximately zero, thus the sine term is not a physical problem.

From the last paragraph, at $t = 0$ (or $f = 0$) we have $H = \frac{2}{3}m_\varphi$, which is the relation we use from now on to determine the start of oscillations.

The cosmological factor at the onset of ${\rm Re}\phi_{\rm ISS}$ oscillations is then given by

$$R_{\phi_{\rm ISS}} = \left(\frac{m_\eta}{m_{\phi_{\rm ISS}}}\right)^{2/3} R_\eta \quad . \tag{6.2.84}$$

[9] The condition $h^2M^2 \gtrsim cH^2\big|_{H=2m_{\phi_{\rm ISS}}/3}$ implies that $\langle\phi_{\rm ISS}\rangle_{\rm ins} > 0$ and consequently ${\rm Re}\phi_{\rm ISS}$ can indeed start oscillations. This condition is satisfied for any h and M, with $c = 3$.

For the cases of ReQ_1, ReS_1 and ReS_2, we have

$$R_{Q_1} = \left(\frac{N_f - N}{6}\right)^{1/3} \left(\frac{M}{M_P}\frac{m_\eta}{m_{3/2}}\right)^{2/3} R_\eta \quad , \tag{6.2.85}$$

$$R_{S_1} = \left(\frac{N_f - N}{6}\right)^{1/3} \left(\frac{M}{M_P}\frac{m_\eta}{m_{3/2}}\right)^{2/3} R_\eta \quad , \tag{6.2.86}$$

$$R_{S_2} = \left(\frac{N_f - N}{3N}\right)^{1/3} \left(\frac{8\pi^2}{(\ln(4) - 1)\, h^2}\right)^{1/3} \left(\frac{M}{M_P}\frac{m_\eta}{m_{3/2}}\right)^{2/3} R_\eta \quad . \tag{6.2.87}$$

From this time on, the ISS fields start to oscillate about their true minimum. This may happen before or after the inflaton oscillations have decayed.

The energy densities for the N oscillating fields ReQ_1 and the N_f oscillating ReS_1 and ReS_2 are given by

$$\rho_{Q_1} = N \cdot \frac{1}{2} m_{Q_1}^2 \langle Q_1 \rangle_{\text{amp}}^2 \left(\frac{R_{Q_1}}{R}\right)^3 \quad , \tag{6.2.88}$$

$$\rho_{S_1} = N \cdot \frac{1}{2} m_{S_1}^2 \langle S_1 \rangle_{\text{amp}}^2 \left(\frac{R_{S_1}}{R}\right)^3 \quad , \tag{6.2.89}$$

$$\rho_{S_2} = (N_f - N) \cdot \frac{1}{2} m_{S_2}^2 \langle S_2 \rangle_{\text{amp}}^2 \left(\frac{R_{S_2}}{R}\right)^3 \quad . \tag{6.2.90}$$

Inserting the relevant quantities, the last equations translate to

$$\rho_{Q_1} = \frac{12N}{N_f - N} \left(\frac{m_{3/2}}{M_{\text{P}}}\right)^2 M_{\text{P}}^4 \left(\frac{R_{Q_1}}{R}\right)^3 \quad , \tag{6.2.91}$$

$$\rho_{S_1} = N \left(\frac{m_{3/2}}{M_{\text{P}}}\right)^2 \left(\frac{M}{M_{\text{P}}}\right)^2 M_{\text{P}}^4 \left(\frac{R_{S_1}}{R}\right)^3 \quad , \tag{6.2.92}$$

$$\rho_{S_2} = \frac{(N_f - N)^2}{N} \left(\frac{16\pi^2}{3(\ln(4) - 1)\, h^2}\right) \left(\frac{m_{3/2}}{M_{\text{P}}}\right)^2 \left(\frac{M}{M_{\text{P}}}\right)^2 M_{\text{P}}^4 \left(\frac{R_{S_2}}{R}\right)^3 \quad . \tag{6.2.93}$$

We write below the decay rate of the inflaton and recall the relevant decay rates of the ISS fields (along with ReQ_2 which will be needed later):

$$\Gamma_\eta \simeq a_\eta^2 \frac{m_\eta^3}{M_{\text{P}}^2} \quad , \tag{6.2.94}$$

$$\Gamma_{S_1}^{\text{total}} \simeq 5.63 \cdot 10^{-2} \frac{m_{3/2}^3}{M_{\text{P}}^2} \left(\frac{M_{\text{P}}}{M}\right)^5 \quad , \tag{6.2.95}$$

$$\Gamma_{S_2}^{\text{total}} \simeq 2.31 \cdot 10^{-9} \frac{m_{3/2}^3 h^5}{M_{\text{P}}^2} \left(\frac{M_{\text{P}}}{M}\right)^5 \quad , \tag{6.2.96}$$

$$\Gamma_{Q_1}^{\text{total}} \simeq 3.13 \cdot 10^{-3} \frac{m_{3/2}^3}{M_{\text{P}}^2} \left(\frac{M_{\text{P}}}{M}\right)^3 + 9.80 \cdot 10^{-11} \frac{m_{3/2}^3 h^2}{M_{\text{P}}^2} \left(\frac{M_{\text{P}}}{M}\right)^5 \quad , \tag{6.2.97}$$

$$\Gamma_{Q_2}^{\text{total}} \simeq 1.44 \cdot 10^{-8} \frac{m_{3/2}^3 h^5}{M_{\text{P}}^2} \left(\frac{M_{\text{P}}}{M}\right)^3 + 2.57 \cdot 10^{-14} \frac{m_{3/2}^3 h^5}{M_{\text{P}}^2} \left(\frac{M_{\text{P}}}{M}\right)^5 \quad . \tag{6.2.98}$$

We assumed that η decays thorugh gravitational interactions. The quantity a_η in the first equation quantifies the couplings of η to matter. For example, this quantity can be very small under the conditions assumed in [169], namely that the gauge kinetic function depends linearly on the inflaton, which thus decays into two MSSM gauge bosons with coupling d_η, yielding the decay rate $\Gamma = \frac{3}{64\pi} d_\eta^2 \frac{m_\eta^3}{M_{\rm P}^2} \sim 10^{-2} d_\eta^2 \frac{m_\eta^3}{M_{\rm P}^2} \equiv a_\eta^2 \frac{m_\eta^3}{M_{\rm P}^2}$. The coupling a_η is given by

$$a_\eta = 10^{-1} d_\eta \quad . \tag{6.2.99}$$

Next we study the evolution of the oscillations along with the decays of the ISS oscillating fields.

Evolution of the universe

Now we discuss how the oscillations and decays referred to in the previous item account for the evolution of the universe. In order to study the evolution of the fields $\mathrm{Re}Q_1$, $\mathrm{Re}S_1$, $\mathrm{Re}S_2$ and η, a some issues must be taken care of.

- We assume, as we already mentioned, that the energy of the universe after the end of inflation is dominated by η oscillations — and by η decay products after it decays;
- we must know whether the ISS fields decay in the η oscillation era or in the η decay products era, since this has an important impact on the energy densities of their products;
- the relativistic decay products may turn non-relativistic as the universe cools down, which means their energy evolves differently than radiation, i.e. $\rho_{\rm rad}/\rho_{\rm non} \sim R^{-1}$;
- decay products which are massless ISS particles should be carefully studied since they contribute to the present relativistic degrees of freedom $N_{\rm eff}$, which is $N_{\rm eff} = 3.15 \pm 0.23$ [45];
- decay products with small decay rates should be also carefully studied, since they should not decay after the BBN epoch, i.e. $T \sim 1$ MeV.

We start with the first point. The combined $\phi_{\rm ISS}$ oscillation energy is given by

$$\begin{aligned} \rho_{\phi_{\rm ISS}} &= \rho_{Q_1} + \rho_{S_1} + \rho_{S_2} \\ &= \left(\frac{m_{3/2}}{M_{\rm P}}\right)^2 M_{\rm P}^4 \left\{ \frac{12N}{N_f - N} \left(\frac{R_{Q_1}}{R}\right)^3 + N \left(\frac{M}{M_{\rm P}}\right)^2 \left(\frac{R_{S_1}}{R}\right)^3 \right. \\ &\quad \left. + \frac{(N_f - N)^2}{N} \left(\frac{16\pi^2}{3\left(\ln(4) - 1\right) h^2}\right) \left(\frac{M}{M_{\rm P}}\right)^2 \left(\frac{R_{S_2}}{R}\right)^3 \right\} \quad . \end{aligned} \tag{6.2.100}$$

In order to compare $\rho_{\phi_{\rm ISS}}$ and ρ_η, we need to rearrange the energy expression of the former.

We rewrite it as

$$\rho_{\phi_{\rm ISS}} = m_\eta^2 M_{\rm P}^2 \left\{ 2\left(\frac{M}{M_{\rm P}}\right)^2 + \frac{1}{2}\left(\frac{M}{M_{\rm P}}\right)^4 + \frac{2.51\cdot 10^5}{h^4}\left(\frac{M}{M_{\rm P}}\right)^4 \right\} \left(\frac{R_\eta}{R}\right)^3 \quad , \tag{6.2.101}$$

where we have used the eqs. (6.2.85), (6.2.86) and (6.2.87) with $N = 1$ and $N_f = 4$. When compared to the energy density of η, namely

$$\rho_\eta = \frac{4}{3} m_\eta^2 M_{\rm P}^2 \left(\frac{R_\eta}{R}\right)^3 \quad \text{for} \quad R_\eta < R < R_{{\rm d}\eta} \quad , \tag{6.2.102}$$

we obtain $\rho_\eta > \rho_{\phi_{\rm ISS}}$ at the end of inflation only if

$$\frac{M}{M_{\rm P}} < 4.80\cdot 10^{-2} h \quad . \tag{6.2.103}$$

This requirement will be further discussed in figs. 6.3 and 6.4 with entropy production constraints.

Now we turn to the question of the decay epoch of $\phi_{\rm ISS}$, which depends on whether they decay before or after η reheating, i.e. when η decays itself. For the former and the latter, we obtain respectively

$$\begin{aligned} \frac{R_{{\rm d}\phi_{\rm ISS}}}{R_{{\rm d}\eta}} &= a_\eta^{4/3} \left(\frac{M_{\rm P}}{\Gamma_{\phi_{\rm ISS}}}\right)^{2/3} \left(\frac{m_\eta}{M_{\rm P}}\right)^2 \quad , \\ \frac{R_{{\rm d}\phi_{\rm ISS}}}{R_{{\rm d}\eta}} &= \frac{2}{\sqrt{3}} a_\eta \left(\frac{M_{\rm P}}{\Gamma_{\phi_{\rm ISS}}}\right)^{1/2} \left(\frac{m_\eta}{M_{\rm P}}\right)^{3/2} \quad , \end{aligned}$$

where $R_{{\rm d}\phi_{\rm ISS}}$ is the scale factor at $\phi_{\rm ISS}$ decay and similarly for η. Here we have used $H = a\Gamma$ to obtain the decay epochs — $a = 2/3$ for matter domination and $a = 1/2$ for radiation domination — as well as $R_\eta/R_{{\rm d}\eta} = a_\eta^{4/3}\left(\frac{m_\eta}{M_{\rm P}}\right)^{4/3}$. If $\frac{R_{{\rm d}\phi_{\rm ISS}}}{R_{{\rm d}\eta}} < 1\,(>1)$, $\phi_{\rm ISS}$ decays before (after) the inflaton does. We show in fig. 6.1 how the parameters M and h determine the time of their decays. Since we want the η oscillation energy to be greater than the one of $\phi_{\rm ISS}$, production of entropy from the latter fields will only be problematic if one or more of them decays after η has already decayed. The energy density of the decay products of η is given by

$$\rho_\eta^r = \rho_{{\rm d}\eta}\left(\frac{R_{{\rm d}\eta}}{R}\right)^4 = \frac{4}{3} a_\eta^4 M_{\rm P}^4 \left(\frac{m_\eta}{M_{\rm P}}\right)^6 \left(\frac{R_{{\rm d}\eta}}{R}\right)^4 \quad \text{for} \quad R_\eta < R < R_{{\rm d}\eta} \quad , \tag{6.2.104}$$

where $\rho_{{\rm d}\eta}$ is the energy density ρ_η at the moment of η decay.

Now, assuming $\rho_{\phi_{\rm ISS}}^r$ is the energy density of radiation from Q_1, S_1 and S_2, we can define a scale factor R_1 where $\rho_\eta^r(R_1) = \rho_{\phi_{\rm ISS}}^r(R_1)$. Finding R_1 means there exists a limit on the entropy produced by these ISS fields such that $s_\eta > s_{\phi_{\rm ISS}}$ is satisfied, where for any field i the following relation holds, $s_i/s_j \sim \left(\rho_i^r/\rho_j^r\right)^{3/4}$. The energy density $\rho_{\phi_{\rm ISS}}^r(R)$

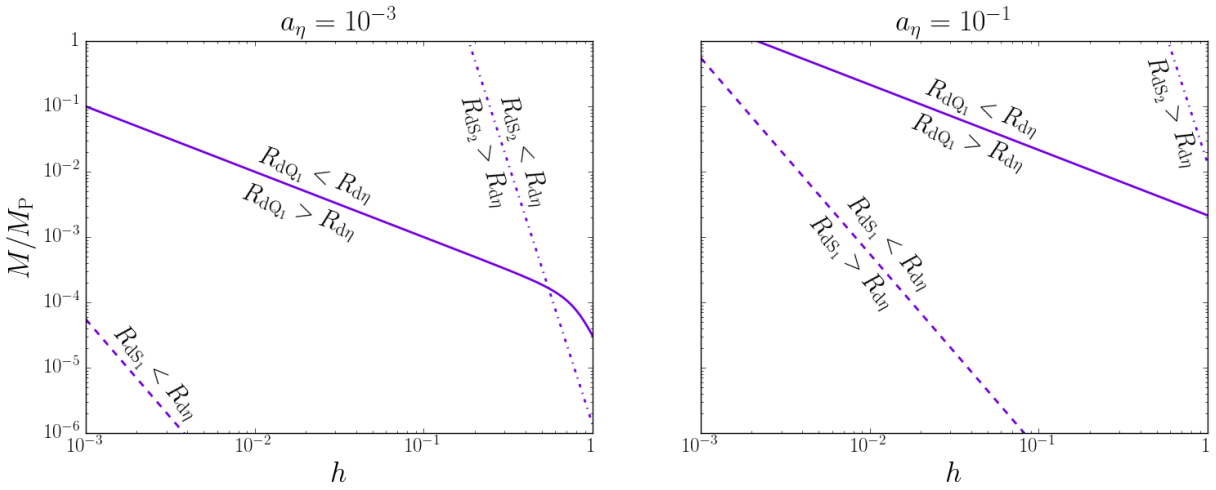

Figure 6.1: The curves of $\Gamma^i_{\phi_{\rm ISS}} = \Gamma_\eta$, where $i = Q_1, S_1, S_2$ for small (large) coupling $a_\eta = 10^{-3}$ ($a_\eta = 10^{-1}$). Above the curves, the decay rates $\Gamma^i_{\phi_{\rm ISS}}$ become larger, implying a smaller scale factor at the time of $\phi_{\rm ISS}$ decay.

is given by

$$\rho^r_{\phi_{\rm ISS}}(R) = \rho_{{\rm d}Q_1}\left(\frac{R_{{\rm d}Q_1}}{R}\right)^4 + \rho_{{\rm d}S_1}\left(\frac{R_{{\rm d}S_1}}{R}\right)^4 + \rho_{{\rm d}S_2}\left(\frac{R_{{\rm d}S_2}}{R}\right)^4 \quad . \tag{6.2.105}$$

If $\rho^r_\eta(R_1) > \rho^r_{\phi_{\rm ISS}}(R_1)$, then most entropy comes from η decays; otherwise, the ISS decays would provide the most entropy. When $\rho^r_{\phi_{\rm ISS}}$ is evaluated at R_1, the latter is necessary equal to the scale factor of the last decaying field, since otherwise the ISS energy density (if considering matter and radiation together) would overcome ρ^r_η again, since $\rho_{\rm rad}/\rho_{\rm matter} \sim R^{-1}$.

For example, assuming $R_{{\rm d}Q_1} < R_{{\rm d}S_1} < R_{{\rm d}S_2}$, one would obtain

$$\rho^r_{\phi_{\rm ISS}}(R_1) = \rho_{{\rm d}Q_1}\left(\frac{R_{{\rm d}Q_1}}{R_1}\right)^4 + \rho_{{\rm d}S_1}\left(\frac{R_{{\rm d}S_1}}{R_1}\right)^4 + \rho_{{\rm d}S_2} \quad , \tag{6.2.106}$$

where $R_1 = R_{{\rm d}S_2}$ for S_2 as the latest decaying particle. Taking these details into account, in the fig. 6.2 we plot numerically the bound $s_\eta > s_{\phi_{\rm ISS}}$. A comment is in order. For the region at which the curve is drawn, S_2 dominates the energy density compared with the ones from either Q_1 or S_1 because it has the longest lifetime and a sizable VEV. Both Q_1 and S_1 become important only for smaller M and larger h, i.e. in the lower right corner of both figures. In addition, there is a noticeable step at the right upper corner for both cases $a_\eta = 10^{-3}$ and $a_\eta = 10^{-1}$. They form at the point at which S_2 turns from decaying after η to decaying before η. This introduces a dip in the S_2 energy density function. The step is quite steep only because our analysis assumes instantaneous decays.

To this discussion we must add the bahaviour of the decay products of Q_1, S_1 and S_2. These decay products can turn from relativistic to non-relativistic at some point, which could render their energy bigger than ρ^r_η. Below we find onstraints such that their energy density do not surpass ρ^r_η. For this, we start by displaying the decay products of each

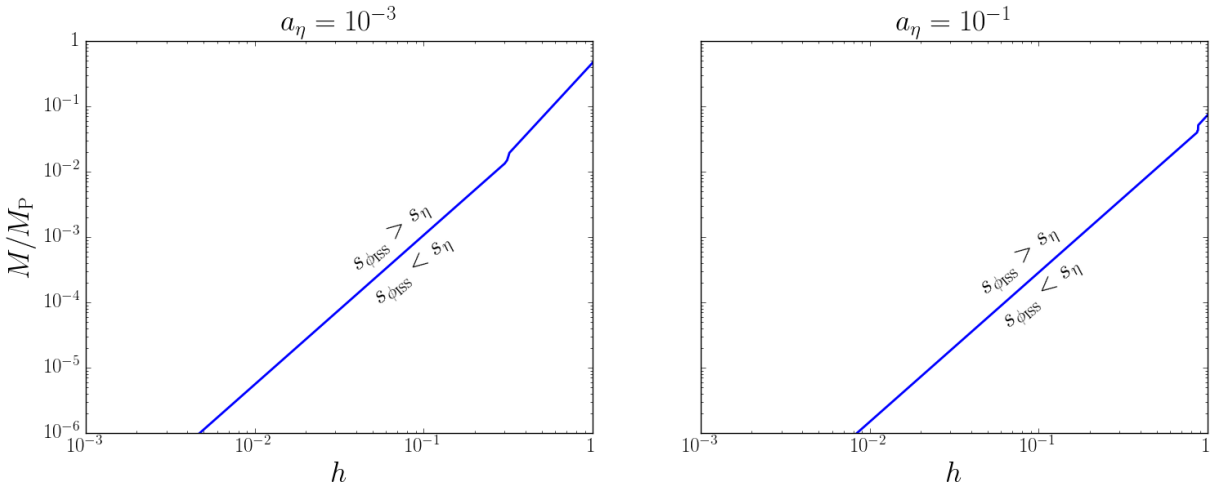

Figure 6.2: The curve of $s_{\phi_{\rm ISS}} = s_\eta$ numerically obtained from eq. (6.2.106) at the decay epoch of S_2, the last decaying particle, for small (large) coupling $a_\eta = 10^{-3}$ ($a_\eta = 10^{-1}$). Above the curve, the energy density $\rho^r_{\phi_{\rm ISS}}$ becomes larger, implying also a larger total entropy density at the decay time of S_2.

field,

$$\begin{aligned}
{\rm Re}S_1 &: (\chi_{S1} + \bar{\chi}_{S1}) \quad , && (6.2.107)\\
{\rm Re}S_2 &: \left(\psi_{3/2} + \psi_{3/2}\right) \quad , && (6.2.108)\\
{\rm Re}Q_1 &: \left(\psi_{3/2} + \psi_{3/2},\, \chi_{S1} + \bar{\chi}_{S1} + {\rm Im}Q_2,\, \chi_{S1} + \bar{\chi}_{S1} + {\rm Re}Q_2\right) \quad , && (6.2.109)\\
{\rm Re}Q_2 &: \left(\psi_{3/2} + \psi_{3/2},\, \chi_{S1} + \bar{\chi}_{S1} + {\rm Im}Q_2\right) \quad . && (6.2.110)
\end{aligned}$$

Additionally, we recall the masses of the final particles,

$$\begin{aligned}
m_{\chi_{S1}} &= m_{3/2} \quad ,\\
m_{{\rm Re}Q_2} &= \sqrt{\frac{3\left(\ln\left(4\right) - 1\right)}{8\pi^2}} h \left(\frac{M_{\rm P}}{M}\right) m_{3/2} \quad , && (6.2.111)\\
m_{{\rm Im}Q_2} &= 0 \quad .
\end{aligned}$$

Since $m_{{\rm Im}Q_2} = 0$, ${\rm Im}Q_2$ can never become non-relativistic. For massive particles, the scale factor at which they turn non-relativistic $R_{\rm non}$ is related to the scale factor at the decay

of the initial particle. We have the following relations:

$$
\begin{aligned}
\mathrm{Re}S_1 \quad &: \quad \frac{R_{\mathrm{d}S_1}}{R_{\mathrm{non}}^{\chi_{S1}}} = \frac{2m_{\chi_{S1}}}{m_{\mathrm{Re}S_1}}\,, \\
\mathrm{Re}S_2 \quad &: \quad \frac{R_{\mathrm{d}S_2}}{R_{\mathrm{non}}^{\psi_{3/2}}} = \frac{2m_{\psi_{3/2}}}{m_{\mathrm{Re}S_2}}\,, \\
\mathrm{Re}Q_1 \quad &: \quad \frac{R_{\mathrm{d}Q_1}}{R_{\mathrm{non}}^{\psi_{3/2}}} = \frac{2m_{\psi_{3/2}}}{m_{\mathrm{Re}Q_1}}\,, \quad \frac{R_{\mathrm{d}Q_1}}{R_{\mathrm{non}}^{\chi_{S1}}} = \frac{3m_{\chi_{S1}}}{m_{\mathrm{Re}Q_1}}\,, \quad \frac{R_{\mathrm{d}Q_1}}{R_{\mathrm{non}}^{\mathrm{Im}Q_2}} = \frac{3m_{\mathrm{Im}Q_2}}{m_{\mathrm{Re}Q_1}}\,, \quad \frac{R_{\mathrm{d}Q_1}}{R_{\mathrm{non}}^{\mathrm{Re}Q_2}} = \frac{3m_{\mathrm{Re}Q_2}}{m_{\mathrm{Re}Q_1}}\,, \\
\mathrm{Re}Q_2 \quad &: \quad \frac{R_{\mathrm{d}Q_2}}{R_{\mathrm{non}}^{\psi_{3/2}}} = \frac{2m_{\psi_{3/2}}}{m_{\mathrm{Re}Q_2}}\,, \quad \frac{R_{\mathrm{d}Q_2}}{R_{\mathrm{non}}^{\chi_{S1}}} = \frac{3m_{\chi_{S1}}}{m_{\mathrm{Re}Q_2}}\,, \quad \frac{R_{\mathrm{d}Q_2}}{R_{\mathrm{non}}^{\mathrm{Im}Q_2}} = \frac{3m_{\mathrm{Im}Q_2}}{m_{\mathrm{Re}Q_2}}\,.
\end{aligned}
\tag{6.2.112}
$$

These were computed via $f_\Phi^{\varphi_i} \cdot \rho_{\mathrm{d}\Phi} \cdot (R_{\mathrm{d}\Phi}/R_{\mathrm{non}}^{\varphi_i})^4 = \rho_{\varphi_i}\,(T = m_{\varphi_i})$, where Φ is the mother-particle which decays into $\varphi_i + \varphi_j\,(+\varphi_k)$; and $f_\Phi^{\varphi_i}$ is the share of energy of each Φ particle given to a product-particle φ_i, e.g. $f_\Phi^{\varphi_i} = 1$, for $\Phi = \mathrm{Re}Q_2$ and $\varphi_i = \psi_{3/2}$. We have also considered that the masses of the products are much smaller than the masses of the decaying particles, which leads to the numerical factors in these expressions.

If the decay rate of a particle is sufficiently large, it decays before it can turn non-relativistic. In that case, there would be no change to the curve we obtained in fig. 6.2. On the other hand, if its decay rate is small, we must change the energy density quations accordingly,

$$
\rho_i^{\mathrm{non}} = \sum_j \rho_{\mathrm{d}i} \left(\frac{R_{\mathrm{d}i}}{R_{\mathrm{non}}^j}\right)^4 \left(\frac{R_{\mathrm{non}}^j}{R}\right)^3 = \sum_j \rho_{\mathrm{d}i} \left(\frac{R_{\mathrm{d}i}}{R_{\mathrm{non}}^j}\right) \left(\frac{R_{\mathrm{d}i}}{R}\right)^3 \quad . \tag{6.2.113}
$$

Regarding the decay rates of the products themselves, the one for $\mathrm{Re}Q_2$ is written in eq. (6.2.98) and the ones for $\psi_{3/2}$ and χ_{S1} in eqs. (6.2.71) and (6.2.73), respectively. We calculate again the entropy production upper bound, now taking into account the non-relativistic behaviour of the products χ_{S1}, $\psi_{3/2}$ and $\mathrm{Re}Q_2$. The obtained bound is shown in the red curve in fig. 6.3. It was numerically obtained from eq. (6.2.113).

As one can notice, the deviation from the blue dashed curve becomes more pronounced for lower values of M and h. This is because the products from ISS decays turn non-relativistic earlier as M and h take such values. At $h \gtrsim 0.1$ and for $a_\eta = 10^{-3}$, the ISS products decay when they are still relativistic, thus the agreement on the curves. For $a_\eta = 10^{-1}$, the same happens for $h \gtrsim 0.4$. From now on, we thus consider the constraint on the entropy production from the curve.

We address now the issue of $\mathrm{Im}Q_2$ relativistic degrees of freedom since they are the only massless products in the relevant decays. First we obtain an expression for the energy

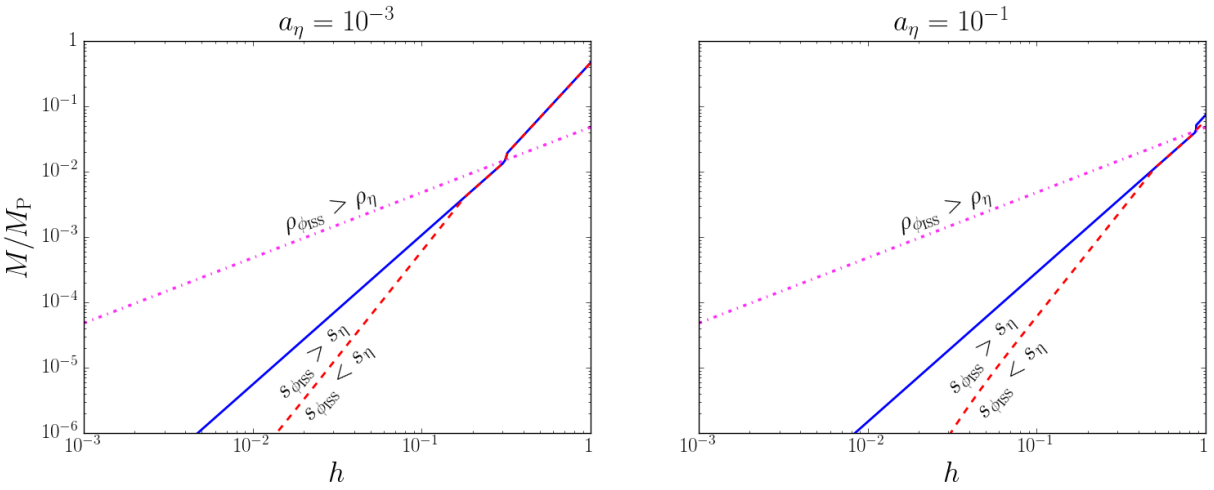

Figure 6.3: The curves of $s_{\phi_{\rm ISS}} = s_\eta$ numerically obtained from eq. (6.2.106) and the magenta dashed curve from eq. (6.2.103) for small (large) coupling $a_\eta = 10^{-3}$ ($a_\eta = 10^{-1}$). The blue curve is evaluated at the S_2 decay epoch , the last ISS deaying particle as already seen in fig. 6.2; and the red dashed curve is evaluated at the decay time of χ_{S1}, which is the last product to decay. We write legends just for the latter because the one for the blue curve has already been given in fig. 6.2.

density from $\mathrm{Im}Q_2$,

$$\begin{aligned}
\rho_{\mathrm{Im}Q_2} &= \frac{\Gamma_{Q_1}^{\chi\chi\mathrm{Re}Q_2}}{\Gamma_{Q_1}^{\rm total}}\left[\frac{1}{3}\left(\frac{R_{\mathrm{d}Q_1}}{R}\right)^4 + \frac{1}{3}\cdot\frac{1}{3}\frac{\Gamma_{Q_2}^{\chi\chi\mathrm{Im}Q_2}}{\Gamma_{Q_2}^{\rm total}}\left(\frac{R_{\mathrm{d}Q_1}}{R_{\rm non}^{\mathrm{Re}Q_2}}\right)^4\left(\frac{R_{\rm non}^{\mathrm{Re}Q_2}}{R_{\mathrm{d}Q_2}}\right)^3\left(\frac{R_{\mathrm{d}Q_2}}{R}\right)^4\right]\rho_{\mathrm{d}Q_1} \\
&= \frac{\Gamma_{Q_1}^{\chi\chi\mathrm{Re}Q_2}}{\Gamma_{Q_1}^{\rm total}}\left[\frac{1}{3} + \frac{1}{9}\frac{\Gamma_{Q_2}^{\chi\chi\mathrm{Im}Q_2}}{\Gamma_{Q_2}^{\rm total}}\left(\frac{R_{\mathrm{d}Q_2}}{R_{\rm non}^{\mathrm{Re}Q_2}}\right)\right]\rho_{\mathrm{d}Q_1}\left(\frac{R_{\mathrm{d}Q_1}}{R}\right)^4 \\
&\simeq \frac{\Gamma_{Q_1}^{\chi\chi\mathrm{Re}Q_2}}{\Gamma_{Q_1}^{\rm total}}\left[\frac{1}{9}\frac{\Gamma_{Q_2}^{\chi\chi\mathrm{Im}Q_2}}{\Gamma_{Q_2}^{\rm total}}\left(\frac{R_{\mathrm{d}Q_2}}{R_{\rm non}^{\mathrm{Re}Q_2}}\right)\right]\rho_{\mathrm{d}Q_1}\left(\frac{R_{\mathrm{d}Q_1}}{R}\right)^4 \\
&\leq \frac{1}{18}\left(\frac{R_{\mathrm{d}Q_2}}{R_{\rm non}^{\mathrm{Re}Q_2}}\right)\rho_{\mathrm{d}Q_1}\left(\frac{R_{\mathrm{d}Q_1}}{R}\right)^4 \quad , \qquad (6.2.114)
\end{aligned}$$

where the ratios $\frac{1}{3}$ and $\frac{1}{3}\cdot\frac{1}{3}$ correspond to the energy share carried by $\mathrm{Im}Q_2$ for the two respective sources, $Q_1 \to \bar{\chi}_{S1} + \chi_{S1} + \mathrm{Im}Q_2$ and $Q_1 \to \bar{\chi}_{S1} + \chi_{S1} + \mathrm{Re}Q_2$ followed by $\mathrm{Re}Q_2 \to \bar{\chi}_{S1} + \chi_{S1} + \mathrm{Im}Q_2$, assuming massless products when compared to $\mathrm{Re}Q_1$. We used $\frac{R_{\mathrm{d}Q_2}}{R_{\rm non}^{\mathrm{Re}Q_2}} > 100$ (which can be proven for the parameter ranges $M \in [10^{-6}, 1]$ and $h \in [10^{-3}, 1]$) from the second to the third line; also from the third to the fourth line, we used the maximum values for the branching ratios, i.e. $\frac{\Gamma_{Q_1}^{\chi\chi\mathrm{Re}Q_2}}{\Gamma_{Q_1}^{\rm total}} = \frac{1}{2}$ and $\frac{\Gamma_{Q_2}^{\chi\chi\mathrm{Im}Q_2}}{\Gamma_{Q_2}^{\rm total}} = 1$, for simplicity. Next, we know dark radiation (neutrinos plus other unknown degrees of freedom) to be parametrized by the effective degrees of freedom $N_{\rm eff}$, which yields the energy density for dark radiation (for $T \ll 1\,\mathrm{MeV}$),

$$\rho_{\rm dark} = N_{\rm eff}\frac{7}{8}\left(\frac{4}{11}\right)^{4/3}\rho_\gamma \quad , \qquad (6.2.115)$$

where ρ_γ is the photon energy density. The observational parameter $N_{\rm eff} = 3.15 \pm 0.23$ [45] allows for a significant additional radiation density, if one takes the contribution from the SM three neutrinos to be $N_\nu \simeq 3.046$ [101]. Comparing the two last equations, one can obtain that for the allowed parameter space shown in fig. 6.4, $\rho_{{\rm Im}Q_2} < \rho_{\rm dark} - \rho_{{\rm SM}\,\nu}$.

To summarize the constraints regarding entropy production obtained in this section which will be important for the next section, we collect them in table 6.4 with their legend in fig. 6.4.

Location	Constraint	Meaning	Legend
Eq. (6.2.103)	$\frac{M}{M_{\rm P}} < 4.80 \cdot 10^{-2} h$	$\rho_\eta > \rho_{\phi_{\rm ISS}}$ at the end of inflation	magenta curve
Eq. (6.2.106)	Numerical	$s_\eta > s_{\phi_{\rm ISS}}$ at decay epoch of last decaying product S_2	blue dashed curve
Eq. (6.2.106)	Numerical	$s_\eta > s_{\phi_{\rm ISS}}$ at decay epoch of last decaying product χ_{S1}	red curve

Table 6.4: The constraints on the ISS parameters M and h obtained in this section in order to have acceptable entropy production; their location in the text; their meaning; and their depiction in the figures.

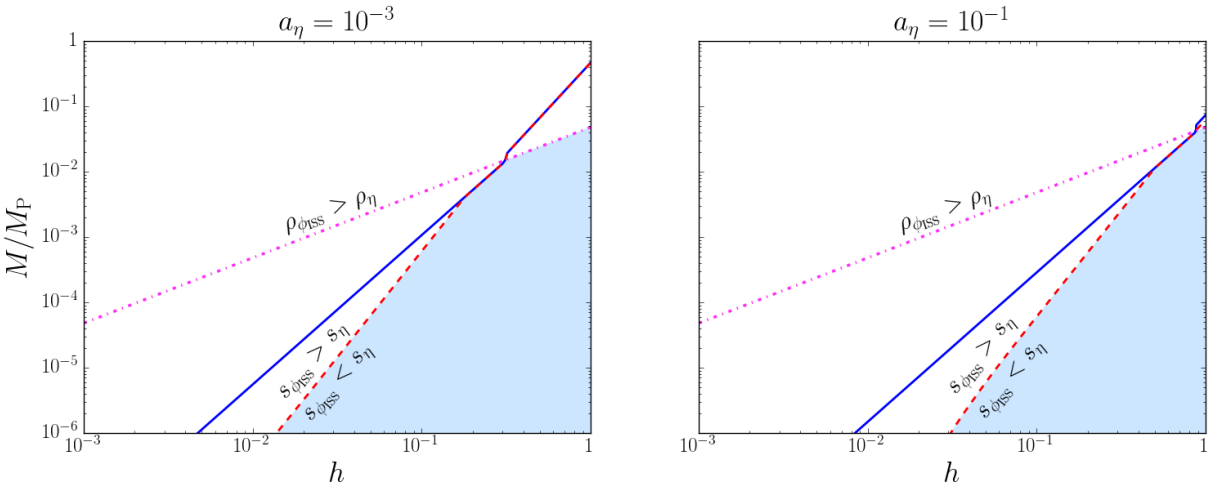

Figure 6.4: The curves $s_{\phi_{\rm ISS}} = s_\eta$ summarizing the constraints obtained in this setion, see table 6.4, for small (large) coupling $a_\eta = 10^{-3}$ ($a_\eta = 10^{-1}$). The allowed region is shaded in blue. It also appears in the next section with the label "sec. 4", where apart from these constraints on entropy production we also consider constraints on dark matter production. Notice that the blue shaded region would be extended to larger values of $M/M_{\rm P}$ and lower values of h if the entropy of the gravitino is not considered (thus just χ_{S1}). More details on how to ignore the gravitino constraint in the next section.

6.2.4 Dark matter production

After finding a protocol for finding solutions to negligible ISS entropy production, we turn now to dark matter production within that scenario. We consider both the production from gravitinos produced thermally within the reheating phase of the inflaton η, and purely non-thermal production from the chain of decays from the ISS fields $\phi_{\rm ISS} = \{{\rm Re}Q_1, {\rm Re}S_1, {\rm Re}S_2\}$ going through gravitinos $\psi_{3/2}$, small mass fermions χ_{S1}, the real scalar ${\rm Re}Q_2$, and then finally into the neutralino dark matter candidate (for this case, the late thermalization of neutralinos will also be studied). The overproduction of non-thermal dark matter is known to be a delicate issue for moduli, of which the Polonyi model [181–183] is an important example.

We can comment a little more specifically on the script and background we have to respect. From decay rate results in sec. 6.2.3, we know that S_1, $S_2$and Q_1 can decay into $\bar{\psi}_{3/2} + \psi_{3/2}$. When this is the case, we have the following relation between the number density of ISS particles $n^i_{\phi_{\rm ISS}}$ and the number density $n_{3/2}$ of the final gravitinos: $n_{3/2} = 2\sum_i n^i_{\phi_{\rm ISS}} \cdot {\rm Br}\left(\phi^i_{\rm ISS} \to \bar{\psi}_{3/2} + \psi_{3/2}\right)$, where ${\rm Br}\left(\Phi_i \to \sum_j \varphi_j\right)$ is the branching ratio of Φ_i into a particular channel $\sum_j \varphi_j$. As another source of gravitinos, one should consider the inflaton either through direct decay or through thermal freezout after η-reheating[10] . After the gravitinos are produced, they decay when $H \sim \Gamma_{3/2}$ into an odd number of lightest supersymmetric particles (LSPs), which we assume to be the neutralino.

On the other hand, the ISS fields can also decay into $\chi_{S1} + \bar{\chi}_{S1}$. In this case, the relation between number densities is a little more diverse. They can be however[11] $n_{\chi_{S1}}/2$ or $n_{\chi_{S1}}/4$ depending on the path one looks in. For example, the path ${\rm Re}Q_1 \to \chi_{S1} + \bar{\chi}_{S1} + {\rm Re}Q_2 \to \chi_{S1} + \bar{\chi}_{S1} + {\rm Im}Q_2$ leads to $n_{\chi_{S1}}/4$, while ${\rm Re}S_1 \to \chi_{S1} + \bar{\chi}_{S1}$ yields $n_{\chi_{S1}}/2$. Every path will be weighed by the respective branching ratio. Each χ_{S1}will in turn contribute to the production of one neutralino at the epoch $H \sim \Gamma_{\chi_{S1}}$.

If the ISS decays into gravitinos or χ_{S1} are too efficient or if η reheating temperature is sufficiently high, the high gravitino or χ_{S1} density may generate an LSP abundance which may overclose the universe. Since we assume that the LSP is a neutralino, its production via direct decays of $\phi_{\rm ISS}$ is negligible compared to its production after the ISS fields have first decayed into gravitinos or χ_{S1}.

Thermal gravitino production

[10] For an exact treatment, one should consider ISS-reheating, since when the ISS fields decay, they could generate a thermal bath with temperature $T_R^{\rm ISS}$, which would produce gravitinos. We assumed up to now that the inflaton η is the field responsible for the current particle content of the universe and the ISS entropy production could never be greater than the one from η decay products. Therefore, constraining entropy production means one does not need to be concerned theoretically about the ISS-reheating gravitino production. Its thermal production comes predominantly from the inflaton decay.

[11] In the case of S_1, ${\rm Re}S_1$ decays directly to $\chi_{S1} + \bar{\chi}_{S1}$. For Q_1, ${\rm Re}Q_1$ decays into $\chi_{S1} + \bar{\chi}_{S1} + \{{\rm Re}Q_2, {\rm Im}Q_2\}$, where ${\rm Re}Q_2$can subsequently decay to $\chi_{S1} + \bar{\chi}_{S1} + {\rm Im}Q_2$. In the case of Q_2, ${\rm Re}Q_2$ decays only into $\chi_{S1} + \bar{\chi}_{S1} + {\rm Im}Q_2$.

We start the analysis of dark matter production via the thermal gravitino source [184], from the thermal plasma created by the decayof the inflaton field η. This production depends on the reheating temperature of the universe dominated by the inflaton after its decay,

$$T_R = \left(\frac{40}{\pi^2 g_\eta}\right)^{1/4} a_\eta \left(\frac{m_\eta}{M_{\rm P}}\right)^{3/2} M_{\rm P} \quad , \tag{6.2.116}$$

where g_η is the number of thermalized relativistic degrees of freedom at temperature T_R.

We assume the inflaton to decay mainly into MSSM particles. If the MSSM and the ISS sector ever had sizeable interactions with each other, that would mean the ISS fields could thermalize with a temperature T_R, and that would pose a problem if $T_R > M_{\rm P}$, since the reheating temperature would then *melt* the condensed ISS sector (recall that the ISS sector considered here is a description of SQCD at low temperatures) and then one would have to deal with the original quarks, squarks, gauge bosons and gauginos. Neither of the two hypothesis are true: the ISS sector and the MSSM do not have as a sizeable interaction as to thermalize the latter with a temperature $T_{\rm R}$; second, we note that $T_R \lesssim 10^{-9} M_{\rm P}$ for $a_\eta \leq 10^{-1}$, $g_\eta = 100$ and $m_\eta = 10^{-5} M_{\rm P}$, therefore T_R is below the energy scale of $M/M_{\rm P}$ considered in the figures of sec. 6.2.3 and further in this section plots.

The ratio of the gravitino number density to the entropy density in the reheating phase is given by, for $m_{1/2} \ll m_{3/2} \ll T_R$ [185] ($m_{1/2}$ stands for the gaugino masses),

$$\left(\frac{n_{3/2}}{s}\right)_{\rm rh} = 2.3 \cdot 10^{-12} \left(\frac{T_R}{10^{10}\ {\rm GeV}}\right) = 2.5 \cdot 10^{-11} a_\eta g_\eta^{-1/4} \left(\frac{m_\eta}{10^{-5} M_P}\right)^{3/2} \quad . \tag{6.2.117}$$

For high values of T_R, this ratio may potentially overclose the universe.

If one assumes the number density of neutralinos is given by[12] $n_\chi \simeq n_{3/2}$, their mass density in units of the critical density ρ_c will be given by

$$\Omega_\chi^{\rm rh} h_{\rm d}^2 \simeq \frac{7 n_\gamma}{s} \frac{m_\chi n_{3/2}}{\rho_c} h_{\rm n}^2 \simeq 2.78 \cdot 10^{10} \left(\frac{m_\chi}{100\ {\rm GeV}}\right) \left(\frac{n_{3/2}}{s}\right)_{\rm rh} \quad , \tag{6.2.118}$$

where today's photon number density is related to today's entropy density by $7 n_\gamma \simeq s_0$, and $h_{\rm d} = H_0 / \left(100\ {\rm km\ s^{-1} MPc^{-1}}\right)$ is the dimensionless Hubble parameter with H_0 being today's dimensionful Hubble parameter. Therefore, for $\Omega_\chi^{\rm rh} h_{\rm d}^2 \lesssim 0.12$, the allowed gravitino to entropy ratio is

$$\left(\frac{n_{3/2}}{s}\right)_{\rm rh} \lesssim 4.32 \cdot 10^{-12} \left(\frac{100\ {\rm GeV}}{m_\chi}\right) \quad . \tag{6.2.119}$$

[12] This assumption is feasible. The R-parity of the gravitino is odd, thus its largest decay rates are the channels $\phi_i^{\rm odd} + \phi_j^{\rm even}$, $\phi_i^{\rm odd} + \phi_j^{\rm even} + \phi_k^{\rm even}$, $\phi_i^{\rm odd} + \phi_j^{\rm odd} + \phi_k^{\rm eodd}$, where ϕ_i represents any possible particle respecting the energy constraint of the initial $m_{3/2}$. However, given a number n of final particles, $(2n-3)$ final particles can be fermions since $\psi_{3/2}$ has mass dimension 3/2. The lowest order process is $\psi_{3/2} \to \phi_i^{\rm odd} + \phi_j^{\rm even}$, which leads to $n_\chi = n_{3/2}$.

By combining eqs. (6.2.117) and (6.2.119), we have the upper bound

$$a_\eta g_\eta^{-1/4} \left(\frac{m_\eta}{10^{-5} M_p}\right)^{3/2} \left(\frac{m_\chi}{100 \text{ GeV}}\right) \lesssim 0.17 \quad . \tag{6.2.120}$$

This bound can be evaded in two distinct situations, namely:

- when th inflaton decays into a gravitino plus an inflatino. However, this channel may be kinematically forbidden if $|m_\eta - m_{\tilde{\eta}}| < m_{3/2}$ (where $\tilde{\eta}$ is the inflatino) or kinematically suppressed if the inflaton(ino) scale is much higher than the gravitino scale, $\mathcal{O}\left(m_{3/2}\right) \ll \mathcal{O}\left(m_\eta,\, m_{\tilde{\eta}}\right)$ [186];

- when the inflaton decays into a pair of gravitinos through the interaction term

$$\begin{aligned} \mathcal{L}_\eta^{3/2} &= -\frac{i}{8}\epsilon^{\mu\nu\rho\sigma}\bar{\psi}_\mu\gamma_\nu\psi_\rho\left(G_\eta\partial_\sigma\eta - G_{\eta^*}\partial_\sigma\eta^*\right) \\ &\quad + \frac{i}{4}\left(1 + K\left(\eta,\bar{\eta}\right)\right) m_{3/2}\left(2 + \frac{W\left(\eta\right)}{W}\right) M_{\rm P}\bar{\psi}_\mu\sigma^{\mu\nu}\psi_\nu \quad , \end{aligned} \tag{6.2.121}$$

  where $W = W_{\text{KL-ISS}} + W_{\text{MSSM}} + W\left(\eta\right)$ is the total superpotenttial, G_η is the derivative of $G = K + \ln\left(W\bar{W}\right)$ with respect to η, and $K = K\left(\eta,\bar{\eta}\right) + K_{\text{KL-ISS}} + K_{\text{MSSM}}$ is the total Kähler potential. As we mentioned before in sec. 6.2.1, we take [169] as an example of how (6.2.121) can yield a null decay rate $\eta \to 2\psi_{3/2}$. There $K\left(\eta,\bar{\eta}\right) \Rightarrow K\left(\left(\eta-\bar{\eta}\right)^2,\, S\bar{S}\right)$, where S is a stabilizer with null expectation value. This implies that the Kähler potential yields null interaction couplings for both terms in (6.2.121). As for $W\left(\eta\right)$, it is defined as $W\left(\eta\right) \Rightarrow Sf\left(\eta\right)$, which implies a zero interaction term between η and $\psi_{3/2}$.

- When gravitinos decay at a temperature which is higher than the freezout temperature of the neutralinos $T_\chi^f \sim m_\chi/20$.

Therefore, the condition (6.2.120) (which has to be satisfied for the neutralino χ not to close the universe) applies if none of the conditions discussed above applies. In this work, we assume the production of gravitinos via direct inflaton/inflatino decays is negligible, and thus from η-reheating we consider only gravitinos which are thermal, i.e. have gone through standard freezout.

Thermal and non-thermal production

We now study the dark matter production via a mixture of thermal and non-thermal processes, from gravitinos produced during the reheating phase of η and from ϕ_{ISS}, decays respectively.

First we study the production of neutralinos from ϕ_{ISS} decays. The number density of neutralinos χ differs whether $R_{\text{d}\phi_{\text{ISS}}} > R_{\text{d}\eta}$ or $R_{\text{d}\phi_{\text{ISS}}} < R_{\text{d}\eta}$. since in the former scenario each ϕ_{ISS} decays are withn the η-reheated universe, and in the latter scenario the universe

is dominated by matter from η oscillations. However, the same ratios of $\psi_{3/2}$ and χ_{S1} number densities, $n_{3/2}$ and $n_{\chi_{S1}}$, to entropy density s are produced in the end. They are given by

$$\begin{aligned}\frac{n_{3/2}}{s} &= a_\eta g_\eta^{-1/4}\left(\frac{m_\eta}{M_P}\right)^{3/2}\left(\frac{M_P}{m_{3/2}}\right)\left(\frac{M}{M_P}\right)^3\times \\ &\quad\left\{2.26\left(\frac{\Gamma_{Q_1}^{2\psi_{3/2}}}{\Gamma_{Q_1}^{\text{total}}}+\frac{\Gamma_{Q_1}^{\chi\chi\text{Re}Q_2}}{\Gamma_{Q_1}^{\text{total}}}\frac{\Gamma_{Q_2}^{2\psi_{3/2}}}{\Gamma_{Q_2}^{\text{total}}}\right)+\frac{5.72\cdot 10^6}{h^5}\left(\frac{M}{M_P}\right)^2\frac{\Gamma_{S_2}^{2\psi_{3/2}}}{\Gamma_{S_2}^{\text{total}}}\right\}\quad , \qquad (6.2.122)\\ \frac{n_{\chi_{S1}}}{s} &= a_\eta g_\eta^{-1/4}\left(\frac{m_\eta}{M_P}\right)^{3/2}\left(\frac{M_P}{m_{3/2}}\right)\left(\frac{M}{M_P}\right)^3\times \\ &\quad\left\{2.26\frac{\Gamma_{Q_1}^{\chi\chi\text{Re}Q_2}}{\Gamma_{Q_1}^{\text{total}}}\left(\frac{\Gamma_{Q_2}^{2\psi_{3/2}}}{\Gamma_{Q_2}^{\text{total}}}+2\frac{\Gamma_{Q_2}^{\chi\chi\text{Im}Q_2}}{\Gamma_{Q_2}^{\text{total}}}+1\right)+0.56\left(\frac{M}{M_P}\right)^2\frac{\Gamma_{S_1}^{\chi\chi}}{\Gamma_{S_1}^{\text{total}}}\right\}\quad , \qquad (6.2.123)\end{aligned}$$

where we used $n_{3/2}\simeq 2\left(\Gamma_{\phi_{\text{ISS}}}^{2\psi_{3/2}}/\Gamma_{\phi_{\text{ISS}}}^{\text{total}}\right)n_{\phi_{\text{ISS}}}$ with $n_{\phi_{\text{ISS}}}=\rho_{\phi_{\text{ISS}}}/m_{\phi_{\text{ISS}}}$ and similarly for χ_{S1}. Furthermore, we use $\Gamma_{Q_1}^{\text{Im}Q_2}\simeq\Gamma_{Q_1}^{\text{Re}Q_2}$. Notice that, for Q_1, there is a possibility of a decay chain generating $n_{\chi_{S1}}$, which we also take into account, translated in the term $\propto\frac{\Gamma_{Q_1}^{\chi\chi\text{Re}Q_2}}{\Gamma_{Q_1}^{\text{total}}}\frac{\Gamma_{Q_2}^{2\psi_{3/2}}}{\Gamma_{Q_2}^{\text{total}}}$. With $n_\chi\simeq n_{3/2}$ and $n_\chi\simeq n_{\chi_{S1}}$ applied in (6.2.122) and (6.2.123) separately, the neutralino relic densities from both sources are then given by

$$\begin{aligned}\Omega_\chi^{3/2}h_{\text{d}}^2 &\simeq \frac{7n_\gamma}{s}\frac{m_\chi n_{3/2}}{\rho_c}h_{\text{d}}^2\\ &\simeq 0.12\cdot\left(\frac{a_\eta}{10^{-2}}\right)\left(\frac{100}{g_\eta}\right)^{1/4}\left(\frac{m_\eta}{10^{-5}M_P}\right)^{3/2}\left(\frac{m_\chi}{100\text{ GeV}}\right)f_{\psi_{3/2}}(h,M)\ , \qquad (6.2.124)\\ \Omega_\chi^{\chi_{S1}}h_{\text{d}}^2 &\simeq \frac{7n_\gamma}{s}\frac{m_\chi n_{\chi_{S1}}}{\rho_c}h_{\text{d}}^2\\ &\simeq 0.12\cdot\left(\frac{a_\eta}{10^{-2}}\right)\left(\frac{100}{g_\eta}\right)^{1/4}\left(\frac{m_\eta}{10^{-5}M_P}\right)^{3/2}\left(\frac{m_\chi}{100\text{ GeV}}\right)f_{\chi_{S1}}(h,M)\ , \qquad (6.2.125)\end{aligned}$$

where we have defined the functions f_i as

$$\begin{aligned}f_{\psi_{3/2}}(h,M) &= 406.56\left(\frac{1}{h}\right)\left(\frac{M}{M_P}\right)\times\\ &\quad\left\{2.26\left(\frac{\Gamma_{Q_1}^{2\psi_{3/2}}}{\Gamma_{Q_1}^{\text{total}}}+\frac{\Gamma_{Q_1}^{\chi\chi\text{Re}Q_2}}{\Gamma_{Q_1}^{\text{total}}}\frac{\Gamma_{Q_2}^{2\psi_{3/2}}}{\Gamma_{Q_2}^{\text{total}}}\right)+\frac{5.72\cdot 10^6}{h^5}\left(\frac{M}{M_P}\right)^2\right\}\ , \qquad (6.2.126)\\ f_{\chi_{S1}}(h,M) &= 406.56\left(\frac{1}{h}\right)\left(\frac{M}{M_P}\right)\times\\ &\quad\left\{2.26\frac{\Gamma_{Q_1}^{\chi\chi\text{Re}Q_2}}{\Gamma_{Q_1}^{\text{total}}}\left(\frac{\Gamma_{Q_2}^{2\psi_{3/2}}}{\Gamma_{Q_2}^{\text{total}}}+2\frac{\Gamma_{Q_2}^{\chi\chi\text{Im}Q_2}}{\Gamma_{Q_2}^{\text{total}}}+1\right)+0.56\left(\frac{M}{M_P}\right)^2\right\}\ . \qquad (6.2.127)\end{aligned}$$

They yield $f_{\psi_{3/2}}(\alpha_h,\alpha_M M_{\text{P}})=1$ and $f_{\chi_{S1}}(\alpha_h,\lambda_M M_{\text{P}})=1$ for α_h, λ_M and α_M. The latter

parameters respect the following relations:

$$
\begin{aligned}
&406.56\,\alpha_h^{-1}\alpha_M\left\{2.26\left[\frac{\Gamma_{Q_1}^{2\psi_{3/2}}}{\Gamma_{Q_1}^{\rm total}}+\frac{\Gamma_{Q_1}^{\chi\chi{\rm Re}Q_2}}{\Gamma_{Q_1}^{\rm total}}\frac{\Gamma_{Q_2}^{2\psi_{3/2}}}{\Gamma_{Q_2}^{\rm total}}\right]_{h=\alpha_h}^{M=\alpha_M M_{\rm P}}+5.72\cdot10^6\frac{\alpha_M^2}{\alpha_h^5}\right\}=1 \quad ,\\
&406.56\,\alpha_h^{-1}\lambda_M\left\{2.26\left[\frac{\Gamma_{Q_1}^{\chi\chi{\rm Re}Q_2}}{\Gamma_{Q_1}^{\rm total}}\left(\frac{\Gamma_{Q_2}^{2\psi_{3/2}}}{\Gamma_{Q_2}^{\rm total}}+2\frac{\Gamma_{Q_2}^{\chi\chi{\rm Im}Q_2}}{\Gamma_{Q_2}^{\rm total}}+1\right)\right]_{h=\alpha_h}^{M=\lambda_M M_{\rm P}}+0.56\,\lambda_M^2\right\}=1 \quad .
\end{aligned}
\tag{6.2.128}
$$

Numerically, we can obtain $\alpha_M = 3.72\cdot10^{-8}$ and $\lambda_M = (1.74\cdot10^{-2},\, 1.48\cdot10^{-6},\, 2.12\cdot10^{-6})$ for $\alpha_h = 10^{-2}$; and $\alpha_M = 1.99\cdot10^{-4}$ and $\lambda_M = (8.05\cdot10^{-2},\, 1.48\cdot10^{-4},\, 2.12\cdot10^{-4})$ for $\alpha_h = 1$. One should use $h=\alpha_h$ and $M=(\alpha_M;\,\lambda_M)\,M_{\rm P}$ to obtain $\Omega_\chi^i h_{\rm d}^2 \simeq 0.12$, where M admits three solutions for χ_{S1}. We replaced $m_{3/2}$ by its function depending on both h and M via eq. (6.2.29). These equations will be later on drawn in fig. 6.5 for comparison with the cosmological constraints obtained so far.

We digress a little about the possibility of dark matter constituted by χ_{S1}. For χ_{S1} to decay before BBN happens ($T\sim 1$ MeV), M has to satisfy

$$
\frac{M}{M_{\rm P}} \gtrsim 1.75\cdot10^{-3}h^{-1/2}M_{\rm P} \quad , \tag{6.2.129}
$$

which implies a quite heavy gravitino mass, since $\psi_{3/2}$ from the constraint of decaying before $T\sim 1$ MeV yields similarly

$$
M \gtrsim 3.82\cdot10^{-6}h^{-1/2}M_{\rm P} \quad . \tag{6.2.130}
$$

If χ_{S1} is allowed to decay after the present time $\sim 10^8$ s, we have to asssume $M \lesssim 2.3\cdot10^{-5}h^{-1/2}M_{\rm P}$. The relic density in that case is written as (rearranging eq. (6.2.125) and using $m_{\chi_{S1}} = m_{3/2}$)

$$
\begin{aligned}
\Omega_{\chi_{S1}}h_{\rm d}^2 &\simeq \frac{7n_\gamma}{s}\frac{m_{3/2}n_{\chi_{S1}}}{\rho_c}h_{\rm d}^2\\
&\simeq 0.12\cdot\left(\frac{a_\eta}{10^{-2}}\right)\left(\frac{100}{g_\eta}\right)^{1/4}\left(\frac{m_\eta}{10^{-5}M_{\rm P}}\right)^{3/2}v_{\chi_{S1}}(h,M) \quad ,
\end{aligned}
\tag{6.2.131}
$$

where we have defined the function $v_{\chi_{S1}}$ as $v_{\chi_{S1}}(h,M) = 1.67\cdot10^{14}h\left(\frac{M}{M_{\rm P}}\right)^2 f_{\chi_{S1}}(h,M)$. It yields $v_{\chi_{S1}}(\alpha_h,\beta_M M_{\rm P}) = 1$ for α_h and β_M, which respect the equation:

$$
6.80\cdot10^{16}\,\beta_M^3\left\{2.26\left[\frac{\Gamma_{Q_1}^{\chi\chi{\rm Re}Q_2}}{\Gamma_{Q_1}^{\rm total}}\left(3-\frac{\Gamma_{Q_2}^{2\psi_{3/2}}}{\Gamma_{Q_2}^{\rm total}}\right)\right]_{h=\alpha_h}^{M=\beta_M M_{\rm P}}+0.56\,\beta_M^2\right\}=1 \quad . \tag{6.2.132}
$$

For instance, we obtain $\beta_M = 8.64\cdot10^{-7}$ for $\alpha_h = 10^{-2}$ and $\beta_M = 8.05\cdot10^{-7}$ for $\alpha_h = 1$. When $a_\eta = 10^{-2}$, $g_\eta = 10^{-2}$ and $m_\eta = 10^{-5}M_{\rm P}$, we have $\Omega_{\chi_{S1}}h_{\rm d}^2 \simeq 0.12$. Here we have replaced $\Gamma_{Q_2}^{\rm total} - \Gamma_{Q_2}^{2\psi_{3/2}} = \Gamma_{Q_2}^{\chi\chi{\rm Im}Q_2}$. From the last equation, it is possible to obtain that χ_{S1}

does not close the universe only for M values (within $a_\eta \in [10^{-3}, 10^{-1}]$ and $h \in [10^{-2}, 1]$) which are below the bound on the gravitino decay rate in eq. (6.2.130). Therefore this scenario is impossible and we then assume the scenario $\Gamma_{\chi_{S1}} > t_{\rm BBN}^{-1}$ (i.e. χ_{S1} decays before BBN).

The eqs. (6.2.124) and (6.2.125) depend on whether the entropy production from $\psi_{3/2}$ and χ_{S1} is negligible. As discussed in sec. 6.2.3, we work within the blue shaded parameter region of fig. 6.4, which implies no significant entropy production from all $\phi_{\rm ISS}$.

We now compare the neutralino comoving number produced by $\phi_{\rm ISS}$ decays and by η reheating. We can obtain

$$\frac{(n_\chi/s)_{\phi_{\rm ISS}\text{ decays}}}{(n_\chi/s)_{\eta\text{ reheating}}} \simeq 1.83\cdot 10^5 \left(\frac{1}{h}\right)\left(\frac{M}{M_P}\right)\left\{2.26\left(1+\frac{\Gamma_{Q_1}^{\chi\chi{\rm Re}Q_2}}{\Gamma_{Q_1}^{\rm total}}\right)+\frac{5.72\cdot 10^6}{h^5}\left(\frac{M}{M_P}\right)^2\right\} \quad , \tag{6.2.133}$$

where the right-hand side yields 1 at $h = \alpha_h$ and $M = \gamma_M M_{\rm P}$, since α_h and γ_M are constrained by

$$1.83\cdot 10^5 \alpha_h^{-1}\gamma_M\left\{2.26\left[1+\frac{\Gamma_{Q_1}^{\chi\chi{\rm Re}Q_2}}{\Gamma_{Q_1}^{\rm total}}\right]_{h=\alpha_h}^{M=\gamma_M M_{\rm P}} + 5.72\cdot 10^6\frac{\gamma_M^2}{\alpha_h^5}\right\} = 1 \quad . \tag{6.2.134}$$

For example, $\gamma_M = 7.87\cdot 10^{-9}$ for $\alpha_h = 10^{-2}$ and $\gamma_M = 1.61\cdot 10^{-6}$ for $\alpha_h = 1$. Here we have replaced $\Gamma_{Q_1}^{2\psi_{3/2}} = \Gamma_{Q_1}^{\rm total} - 2\Gamma_{Q_1}^{\chi\chi{\rm Re}Q_2}$. Furthermore we neglected the last term in eq. (6.2.123) when compared to eq. (6.2.122). Thus unless M assumes very small values, in violation of the bound from eq. (6.2.122), $(n_\chi/s)_{\phi_{\rm ISS}\text{ decays}}$ is dominant over the on from thermal gravitinos. Therefore, we assume the neutralino number density to be given by $\phi_{\rm ISS}$ decay from now on.

An important issue we have to treat now is the annihilation of neutralinos after their production [177]. If the number density of neutralinos produced from $\psi_{3/2}$ or χ_{S1} decays is high enough, they can annihilate each other and in turn decrease their number density. Technically stated, n_χ is governed by the Boltzmann equation

$$\frac{dn_\chi}{dt} + 3Hn_\chi = -\langle\sigma v\rangle n_\chi^2 \quad , \tag{6.2.135}$$

where $\langle\sigma v\rangle$ is the thermally averaged annihilation cross section (as previously explained in sec. 3.4) of the neutralinos. The equilibrium number density $n_{\chi,\,\rm eq}$ was neglected since we look at the epoch soon after they decouple, for which $n_\chi > n_{\chi,\,\rm eq}$ is satisfied.

If $n_\chi \sim H/\langle\sigma v\rangle$, we see that the Hubble term $3Hn_\chi$ and the annihilation term $\langle\sigma v\rangle n_\chi^2$ are of the same order of magnitude. In this case, the neutralino freezes out. If $n_\chi > H/\langle\sigma v\rangle$, the neutralino annihilates after gravitino or χ_{S1} decays, and will freeze out when $n_\chi \sim H/\langle\sigma v\rangle$. On the other hand, if $n_\chi < H/\langle\sigma v\rangle$, the neutralino final density is given at the time of decay of $\psi_{3/2}$ or χ_{S1}. An approximate expression for the final n_χ/s can be

written as

$$\left(\frac{n_\chi}{s}\right)^{-1} \simeq \left(\frac{n_\chi}{s}\right)^{-1}_{\text{decay}} + \left(\frac{H}{s\,\langle\sigma v\rangle}\right)^{-1}_{\text{decay}} \quad , \tag{6.2.136}$$

where the lower index decay means evaluation at the time of $\psi_{3/2}$ or χ_{S1} decay. Therefore, we have an upper limit on n_χ/s, i.e. $n_\chi/s \lesssim H\,\langle\sigma v\rangle^{-1}/s$. The following ratio compares both quantities on the right-hand side of the last equation (both for $\psi_{3/2}$ and χ_{S1}),

$$\left(\frac{H\,\langle\sigma v\rangle^{-1}/s}{n_{3/2}/s}\right)_{\psi_{3/2}} \simeq \left(\frac{10^{-2}}{a_\eta}\right)\left(\frac{10^{-5}M_P}{m_\eta}\right)^{3/2}\left(\frac{10^{-7}\text{GeV}^{-2}}{\langle\sigma v\rangle}\right) w^{-1}_{\psi_{3/2}}(h,M) \ , \tag{6.2.137}$$

$$\left(\frac{H\,\langle\sigma v\rangle^{-1}/s}{n_{\chi_{S1}}/s}\right)_{\chi_{S1}} \simeq \left(\frac{10^{-2}}{a_\eta}\right)\left(\frac{10^{-5}M_P}{m_\eta}\right)^{3/2}\left(\frac{10^{-7}\text{GeV}^{-2}}{\langle\sigma v\rangle}\right) w^{-1}_{\chi_{S1}}(h,M) \ , \tag{6.2.138}$$

with the definitions $w_{\psi_{3/2}}(h,M) = 6.64\cdot 10^{12}h^{3/2}\left(\frac{M}{M_{\rm P}}\right)^3 f_{\psi_{3/2}}(h,M)$ and $w_{\chi_{S1}}(h,M) = 2.49\cdot 10^{16}h^{5/2}\left(\frac{M}{M_{\rm P}}\right)^5 f_{\chi_{S1}}(h,M)$. These functions yield 1 when evaluated at $h=\alpha_h$ and $M=(\kappa_M;\delta_M)\,M_{\rm P}$, which in turn are constrained by

$$\begin{aligned}
&2.70\cdot 10^{15}\alpha_h^{1/2}\kappa_M^4\left\{2.26\left[\frac{\Gamma^{2\psi_{3/2}}_{Q_1}}{\Gamma^{\text{total}}_{Q_1}}+\frac{\Gamma^{\chi\chi\text{Re}Q_2}_{Q_1}}{\Gamma^{\text{total}}_{Q_1}}\frac{\Gamma^{2\psi_{3/2}}_{Q_2}}{\Gamma^{\text{total}}_{Q_2}}\right]^{M=\kappa_M M_{\rm P}}_{h=\alpha_h} + 5.72\cdot 10^6\frac{\kappa_M^2}{\alpha_h^5}\right\} = 1 \ , \\
&1.01\cdot 10^{19}\alpha_h^{3/2}\delta_M^6\left\{2.26\left[\frac{\Gamma^{\chi\chi\text{Re}Q_2}_{Q_1}}{\Gamma^{\text{total}}_{Q_1}}\left(\frac{\Gamma^{2\psi_{3/2}}_{Q_2}}{\Gamma^{\text{total}}_{Q_2}}+2\frac{\Gamma^{\chi\chi\text{Im}Q_2}_{Q_2}}{\Gamma^{\text{total}}_{Q_2}}+1\right)\right]^{M=\delta_M M_{\rm P}}_{h=\alpha_h} + 0.56\,\delta_M^2\right\} = 1 \ .
\end{aligned} \tag{6.2.139}$$

Taking some reference values, we obtain $\delta_M = 3.00\cdot 10^{-2}$ and $\kappa_M = 1.61\cdot 10^{-6}$ for $\alpha_h = 10^{-2}$; and $\delta_M = 8.42\cdot 10^{-3}$ and $\kappa_M = 3.31\cdot 10^{-5}$ for $\alpha_h = 1$. These values yield the lhs ratio equal to 1.

Therefore, if $M \lesssim (\delta_M,\,\kappa_M)\,M_{\rm P}$ and for $\langle\sigma v\rangle = 10^{-7}\text{GeV}^{-2}$, we obtain $n_\chi/s \lesssim H\,\langle\sigma v\rangle^{-1}/s$. In this case, χ do not annihilate themselves and $(n_\chi/s)_{\text{decay}}$ stays constant. Therefore, eqs. (6.2.122) and (6.2.123) are valid for obtaining the neutralino relic density. However, if $M \gtrsim (\delta_M,\,\kappa_M)\,M_{\rm P}$ and for $\langle\sigma v\rangle = 10^{-7}\text{GeV}^{-2}$, it yields $n_\chi/s \gtrsim H\,\langle\sigma v\rangle^{-1}/s$. In this case, the neutralinos annihilate themselves until they reach $n_\chi/s \sim H\,\langle\sigma v\rangle^{-1}/s$. The neutralino relic density would then be written as $\left(\text{for } i=\psi_{3/2},\,\chi_{S1}\right)$

$$\begin{aligned}
\Omega^i_\chi h^2_{\rm d} &= \frac{7n_\gamma}{s}\frac{m_\chi n^i_\chi}{\rho_c}h^2_{\rm d} \qquad\qquad (6.2.140)\\
&\simeq 0.12\left(\frac{100}{g_\eta}\right)^{1/4}\left(\frac{\alpha_h}{h}\right)^{c_i/2}\left(\frac{\varepsilon^i_M M_P}{M}\right)^{c_i}\left(\frac{m_\chi}{100\ \text{GeV}}\right)\left(\frac{10^{-7}\text{GeV}^{-2}}{\langle\sigma v\rangle}\right) \quad .
\end{aligned}$$

c_i stands for the exponents associated with h and M for $\psi_{3/2}$ or χ_{S1} and assume the values

$c_{\psi_{3/2}} = 3$ and $c_{\chi_{S1}} = 5$. The parameters ε^i respect the equations

$$3.33 \cdot 10^{-16} \left(\alpha_h^{1/2} \varepsilon_M^{\psi_{3/2}}\right)^{-3} = 1 \quad , \tag{6.2.141}$$

$$7.25 \cdot 10^{-8} \left(\alpha_h^{1/2} \varepsilon_M^{\chi_{S1}}\right)^{-5} = 1 \quad . \tag{6.2.142}$$

Putting in some numerical values , we have $\varepsilon_M^{\chi_{S1}} = 4.17 \cdot 10^{-2}$ and $\varepsilon_M^{\psi_{3/2}} = 6.93 \cdot 10^{-5}$ for $\alpha_h = 10^{-2}$; and $\varepsilon_M^{\chi_{S1}} = 4.17 \cdot 10^{-3}$ and $\varepsilon_M^{\psi_{3/2}} = 6.93 \cdot 10^{-6}$ for $\alpha_h = 1$. The dependence on h and M stems from $m_{3/2}$ which comes from $R_{\mathrm{d}\chi_{S1}}$ and $R_{\mathrm{d}3/2}$. In other words, replacing $n_\chi^i/s \sim H \langle\sigma v\rangle^{-1}/s$ by $(H_\eta/s_\eta)|_{R_{\mathrm{d}i}} \propto \left(m_{3/2}\right)^{-c_i/2} \propto h^{-c_i/2} M^{-c_i}$.

There are four kinds of neutralinos, namely Wino, Bino and two neutral Higgsinos, which possess the following thermally averaged annihilation cross sections[13]

$$\langle\sigma v\rangle_{\text{Wino}} \simeq \frac{g_2^4}{2\pi} \frac{1}{m_\chi^2} \frac{\left(1 - x_W^2\right)^{3/2}}{\left(2 - x_W^2\right)^2} \overset{m_\chi = 100\ \text{GeV}}{\longrightarrow} 3.33 \cdot 10^{-7}\ \text{GeV}^{-2} \quad , \tag{6.2.143}$$

$$\langle\sigma v\rangle_{\text{Bino}} \simeq \frac{g_1^4}{16\pi} \frac{1}{m_\chi^2} \left(\frac{6T_\chi}{m_\chi}\right) \overset{m_\chi = 100\ \text{GeV}}{\longrightarrow} 1.79 \cdot 10^{-9}\, T_\chi\ \text{GeV}^{-3} \quad , \tag{6.2.144}$$

$$\langle\sigma v\rangle_{\text{Higgsino}} \simeq \frac{g_2^4}{32\pi} \frac{1}{m_\chi^2} \frac{\left(1 - x_W^2\right)^{3/2}}{\left(2 - x_W^2\right)^2} \overset{m_\chi = 100\ \text{GeV}}{\longrightarrow} 2.08 \cdot 10^{-8}\ \text{GeV}^{-2} \quad , \tag{6.2.145}$$

where $x_W = m_W/m_\chi$, and g_1 and g_2 are the couplings of the $U(1)_Y$ and $SU(2)_L$ gauge groups, respectively. The Wino and Higgsino mainly annihilate from an s-wave initial state, while the Bino does through the p-wave, thus the thermally averaged square velocity $\langle v^2\rangle = \frac{6T}{m}$ is important in this last case. Wino pairs annihilate into $W^\pm$ pairs through the mediation of charged Winos[14]. Bino pairs annihilate into lepton pairs via right-handed slepton mediation[15]. Finally, Higgsino pairs annihilate mainly into $W^\pm$ and Z pairs.

Before we summarize the constraints obtained so far, we derive *weak* constraints. They are upper bounds on M such that $\psi_{3/2}$ and/or χ_{S1} do not decay before the neutralino freezes out of the η plasma. This, together with the bounds $\Gamma_{3/2} > t_{\text{BBN}}^{-1}$ and $\Gamma_{\chi_{S1}} > t_{\text{BBN}}^{-1}$ from eqs. (6.2.130) and (6.2.129), form two bands in which the particle can decay so that its decay is safe (related to BBN) and in principle non-negligible (the particle decays after t_χ^{freezout}). For the thermal cross sections of the Wino, Bino and Higgsinos, we know that they freeze out at the values $T_\chi^f \simeq (3.69, 4.27, 4.10)$ GeV, respectively [61]. However, without damaging our conclusions, we take the reference value $\langle\sigma v\rangle = 10^{-7}\ \text{GeV}^{-2}$, which yields $T_\chi^f = 3.86$ GeV. Therefore, for both χ_{S1} and $\psi_{3/2}$ to decay after the neutralino

[13] The Wino thermal cross section can be found from anomaly mediated SUSY breaking [187], while the Bino and the Higgsinos cross sections have been given in [188].

[14] We disregard coannihilations. If one does consider them, they end up increasing $\langle\sigma v\rangle$ (though not necessarily for Winos) which in turn decreases their relic density.

[15] We defined the right-handed slepton mass $m_{\tilde{l}_R}$ to be equal to m_χ. Considering a greater $m_{\tilde{l}_R}$ decreases its $\langle\sigma v\rangle$, increasing thus its relic density.

Location	Constraint	Meaning	Legend
Eq. (6.2.130) and eq. (6.2.147)	$\frac{M}{M_{\rm P}} \gtrsim 3.82 \cdot 10^{-6} h^{-1/2}$ and $\frac{M}{M_{\rm P}} \lesssim 2.56 \cdot 10^{-5} h^{-1/2}$	$\psi_{3/2}$ decays before BBN and $\psi_{3/2}$ decays after neutralino freezout	upper yellow band
Fig. 6.4	Numerical and $\frac{M}{M_{\rm P}} < 4.80 \cdot 10^{-2} h$	$s_\eta > s_{\phi_{\rm ISS}}$ and $\rho_\eta > \rho_{\phi_{\rm ISS}}$	blue shaded region
Eq. (6.2.129) and eq. (6.2.146)	$\frac{M}{M_{\rm P}} \gtrsim 1.75 \cdot 10^{-3} h^{-1/2}$ and $\frac{M}{M_{\rm P}} \lesssim 9.12 \cdot 10^{-5} h^{-1/2}$	χ_{S1} decays before BBN and χ_{S1} decays after neutralino freezout	lower yellow band

Table 6.5: All constraints on the ISS parameters M and h we take into account in this section. Their location in the text; their meaning; and their depiction in this section figures are also given. Again, notice that the blue shaded region enlarges for the plots of χ_{S1} when the entropy production from gravitinos is not considered. The latter case is discussed in the text.

freezout, M must assume the upper values, respectively[16],

$$\frac{M}{M_{\rm P}} \lesssim 9.12 \cdot 10^{-3} h^{-1/2} \quad , \tag{6.2.146}$$

$$\frac{M}{M_{\rm P}} \lesssim 2.56 \cdot 10^{-5} h^{-1/2} \quad . \tag{6.2.147}$$

For a better understanding of the constraints on the parameter space in fig. (6.5) and (6.6), we bring them into table (6.5) and take them into account for the next figures of this section.

In the remainder of this section, we discuss the figures 6.5 and 6.6, which comprise basically dark matter generation and entropy constraints (for $a_\eta = 10^{-3}$ and $a_\eta = 10^{-1}$), theoretically introduced in secs. 6.2.3 and 6.2.4. A general thing first: the blue shaded regions stand for regions which respect small ISS entropy production, i.e. the regions below the orange line (χ_{s1} case on the upper subfigures) and the red-dashed line ($\psi_{3/2}$ case on the lower subfigures). We start the discussion by fig. 6.5.

- Upper subfigures: They deal with both the χ production from χ_{S1} as well as the entropy density $s_{\chi_{S1}}$ produced from the decays of χ_{S1}.
  - *Left corner* ($a_\eta = 10^{-3}$). The black line (6.2.123) stands for χ production directly after the χ_{S1} particles decay; the green one (6.2.140) is not evaluated right after χ_{S1} decays, but after χ annihilations which take place after χ_{S1} decays; and the blue dashed curve (6.2.138) measures if either the black or the green line are valid (above it, the green line should be used, whereas the black line should be used below). The yellow band comprises the epoch after

[16] These results come from $\rho_\eta^r(R_{{\rm d}i}) = \frac{\pi}{30} g_\eta \left(T_\chi^f\right)^4$, for $i = \psi_{3/2}, \chi_{S1}$. One should replace the left-hand side by either $\rho_\eta (R_{{\rm d}\eta}/R_{{\rm d}i})^4$, and the M dependence will show up once we replace $R_{{\rm d}\eta}/R_{{\rm d}i} \propto (\Gamma_i/\Gamma_\eta)^{1/2}$.

χ standard thermal freezout (6.2.146) and before BBN (6.2.129), expressed in terms of $\Gamma_{\chi_{S1}}$ (or equivalently h and M). Having defined the elements, we may comment on their consequences: χ can attain $\Omega_\chi h_{\rm d}^2 \simeq 0.12$ either from the black or the green line since (i) χ from χ_{S1} decays must be within the (yellow+blue=green) band; (ii) within the green band and above the blue dashed line, χ production following the green line (valid from the blue dashed line argument) is $\Omega_\chi h_{\rm d}^2 < 0.12$ above the green line, being 0.12 on the latter; (iii) similarly, within the green band, but now below the blue dashed line, χ production directly from χ_{S1} decays respects $\Omega_\chi h_{\rm d}^2 < 0.12$ below black line, being 0.12 on the latter. Finally, the orange line (now above $M = M_{\rm P}$, but visible for $a_\eta = 10^{-1}$) is the upper bound on the entropy density produced by χ_{S1} decays, i.e. $s_\eta = s_{\chi_{S1}}$. The entropy density $s_{3/2}$ from the gravitino decays is not considered in and above the χ_{S1} yellow band because in this regions $\psi_{3/2}$ would decay before neutralino freezout, thus χ production from gravitino sources are negligible.

- *Right corner* ($a_\eta = 10^{-1}$). The definitions of the black, green and blue-dashed lines are the same as for $a_\eta = 10^{-3}$, as well as the yellow band. Similarly to the left upper subfigure, χ can yield $\Omega_\chi h_{\rm d}^2 \simeq 0.12$ either from the black line or the green line where due to analogical arguments, however the intersection point among the black, green and blue-dashed curves is at $h \simeq 7 \cdot 10^{-2}$, opposed to $h \simeq 10^{-2}$. This difference is due to a_η. Notice the orange line, explained above, appears here below $M = M_{\rm P}$; it does not however constrain much of the parameter space.

The red dashed curve is shown for reference.

- Lower subfigures: They deal with both the χ production from $\psi_{3/2}$ as well as the entropy density $s_{3/2} + s_{\chi_{S1}}$.
  - *Left corner* ($a_\eta = 10^{-3}$). The definitions of the black, green and blue-dashed lines are similar to the ones used for χ_{S1}, and are governed by eqs. (6.2.122), (6.2.140), (6.2.137). The yellow band comprises the epoch after χ standard thermal freezout (6.2.147) and before BBN (6.2.130), expressed in terms of $\Gamma_{3/2}$ (or equivalently h and M). The conclusion is: if we considered just $\psi_{3/2}$ as the product of ISS decays, we could obtain $\Omega_\chi h_{\rm d}^2 \simeq 0.12$ for both black and green lines roughly at the intersection of those with the blue-dashed curve ($h \simeq 0.17$), since above the latter the green one can provide $\Omega_\chi h_{\rm d}^2 \simeq 0.12$, and below it the black one also can provide $\Omega_\chi h_{\rm d}^2 \simeq 0.12$. However, we have to deal with the whole picture, $\psi_{3/2}$ and χ_{S1}. In this case, if we are within the gravitino yellow band, χ_{S1} decays after BBN and this is problematic, since as we have seen in eq. (6.2.131) $\Omega_{\chi_{S1}} h_{\rm d}^2$ cannot be ignored.
  - *Right corner* ($a_\eta = 10^{-1}$). The definitions of the black, green and blue-dashed lines as well as the yellow band are the same as for $a_\eta = 10^{-3}$. Also, the

conclusions are the same: though taking into account just $\psi_{3/2}$ could provide enough neutralino relic density, χ_{S1} relic density is non-negligible after BBN.

After finding suitable solutions for neutralino dark matter within the parameter set used in fig. 6.5, now we turn to 6.6 where we allowed the neutralino thermal cross section to have a lower value $\langle\sigma v\rangle = 10^{-10}$ GeV^{-2}, thereby studying its consequences.

For the lower subfigures, the problem we discussed for $\psi_{3/2}$ ($a_\eta = 10^{-3}$ and 10^{-1}) still stands, i.e. χ_{S1} cannot decay before BBN while at the same time $\psi_{3/2}$ generates the right relic density $\Omega_\chi h_{\rm d}^2 \simeq 0.12$. For the upper part of fig. 6.6, the three lines intersection moves to $h \simeq 7 \cdot 10^{-2}$ (for $a_\eta = 10^{-3}$) and to $h \simeq 4 \cdot 10^{-1}$ (for $a_\eta = 10^{-1}$), however above the green band. This fact implies that the green line stays above the green band (i.e. χ_{S1} decays while χ has not yet frozen out), which means that $\Omega_\chi h_{\rm d}^2 \leq 0.12$ from χ production via subsequent annihilations only happens above the green line and is therefore irrelevant. On the other hand, below the blue-dashed line, we have $\Omega_\chi h_{\rm d}^2 \simeq 0.12$ on the black line and < 0.12 below it. Still, notice that in this case, for the χ production via direct decays to be relevant, the parameters (M, h) must be in the green band.

Along with nonthermal production of neutralinos, we have to discuss their thermal production from freezout. The contributions, due to purely thermal neutralino freezout from the η plasma, assumes the values for Wino, Bino and Higgsino [60, 61, 189]:

$$\Omega_{\rm Wino}^{\rm freezout} h_{\rm d}^2 \simeq 7.03 \cdot 10^{-4} \quad , \tag{6.2.148}$$

$$\Omega_{\rm Bino}^{\rm freezout} h_{\rm d}^2 \simeq 0.0261 \quad , \tag{6.2.149}$$

$$\Omega_{\rm Higgsino}^{\rm freezout} h_{\rm d}^2 \simeq 0.010 \quad . \tag{6.2.150}$$

Notice then that for $m_\chi = 100$ GeV, the Bino and Wino relic densities yield ~ 0.1 of the required $\Omega_{\rm CDM} h_{\rm d}^2 \simeq 0.12$. In these cases, this means that if one wants to obtain $\Omega_\chi h_{\rm d}^2 \simeq 0.12$ for $m_\chi = 100$ GeV, he has to consider (h, M) points slightly off the black and green lines so that $\Omega_\chi^{\chi_{S1}} h_{\rm d}^2 \sim 0.9 \cdot \Omega_{\rm CDM} h_{\rm d}^2$. In the end, we would have $\Omega_\chi^{\rm freezout} h_{\rm d}^2 + \Omega_\chi^{\chi_{S1}} h_{\rm d}^2 \simeq \Omega_{\rm CDM} h_{\rm d}^2$.

For the case when χ_{S1} decays above the green band, that means the thermal freezout must account for all dark matter density, hence $\Omega_\chi^{\rm freezout} h_{\rm d}^2 \simeq 0.12$. This can be accomplished considering e.g. a Bino LSP, if one considers $m_{\tilde{l}_R} \simeq 220$ GeV.

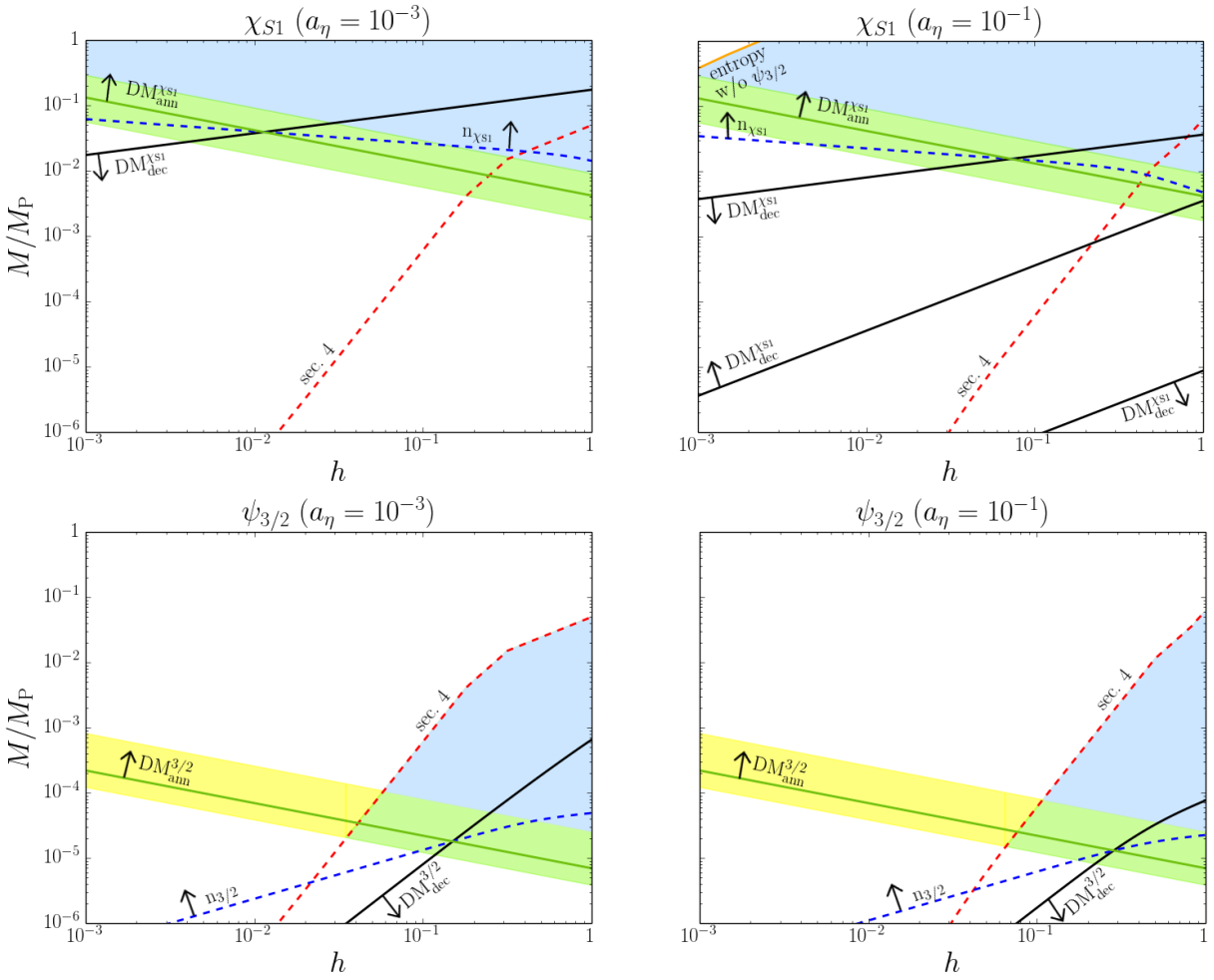

Figure 6.5: All the constraints on the ISS parameters M and h for dark matter production from either decays $\mathrm{DM}_{\rm dec}$ or decays followed by annihilations $\mathrm{DM}_{\rm ann}$ for χ_{S1} and $\psi_{3/2}$ — for a thermal cross section $\langle\sigma v\rangle = 10^{-7}$ GeV^{-2} and for small (large) coupling $a_\eta = 10^{-3}$ ($a_\eta = 10^{-1}$). Notice that the blue shaded regions combined with the yellow bands for χ_{S1} or $\psi_{3/2}$ yield the green regions. The yellow band for χ_{S1} does not appear separately from the green region separately, but is "hidden" behind the green region, whereas for $\psi_{3/2}$ that is not the case. The arrows for the green and black lines point in the direction where $\Omega_\chi h_{\rm d}^2 < 0.12$, whereas the arrow for the blue-dashed line points in the direction where $n_\chi/s > H\,\langle\sigma v\rangle^{-1}/s$, hence neutralino production $\mathrm{DM}_{\rm ann}$ via ISS decays and subsequent annihilation is important. Below that line, we have $n_\chi/s < H\,\langle\sigma v\rangle^{-1}/s$, thus neutralino production must be studied with $\mathrm{DM}_{\rm ann}$.

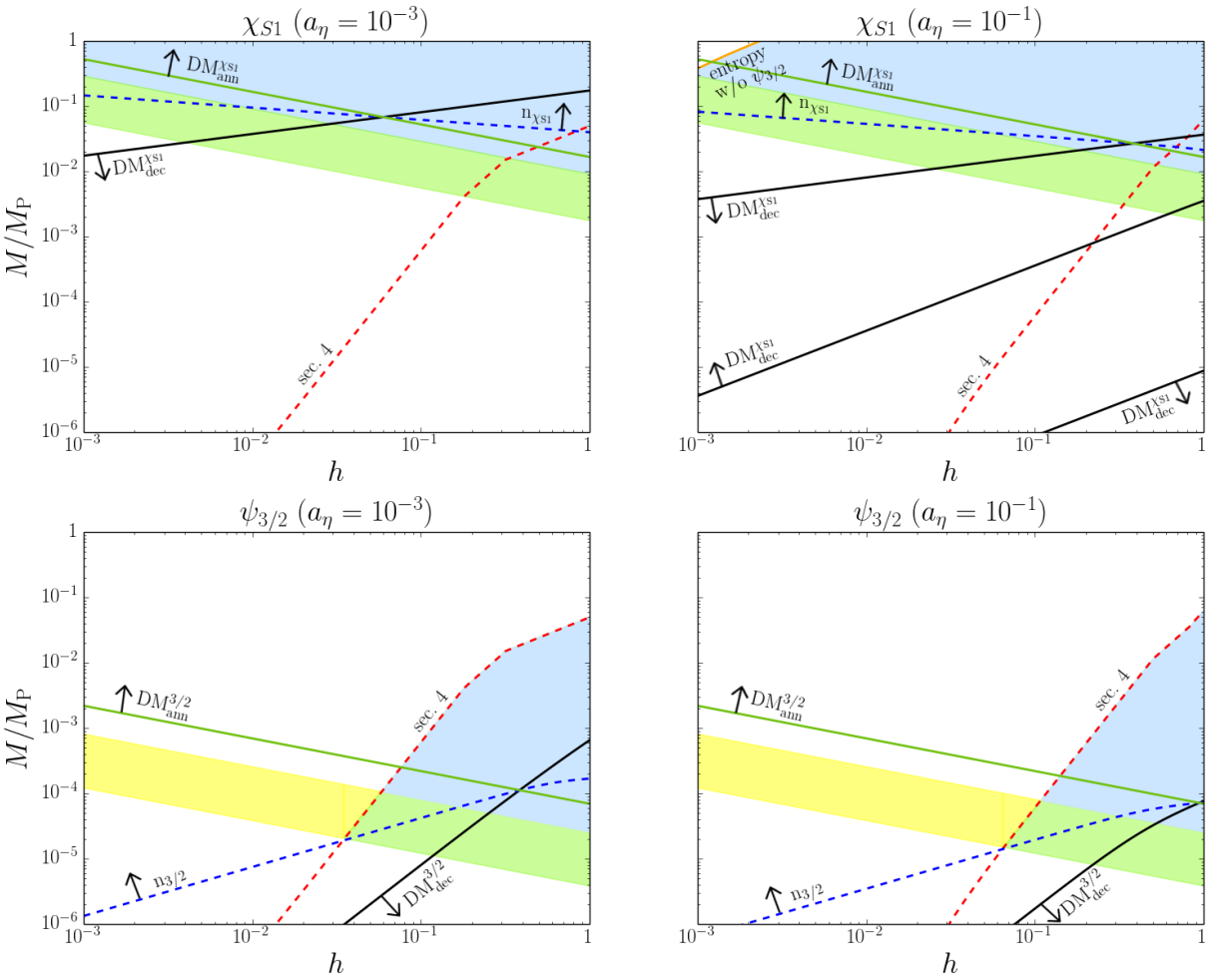

Figure 6.6: All the constraints on the ISS parameters M and h for fark matter production from either direct decays $\mathrm{DM}_{\rm dec}$ or decays followed by annihilations $\mathrm{DM}_{\rm ann}$ for χ_{S1} and $\psi_{3/2}$ — for a thermal cross section $\langle\sigma v\rangle = 10^{-10}$ GeV^{-2} for a large (small) parameter $a_\eta = 10^{-3}$ ($a_\eta = 10^{-1}$). The arrows directions were explained in fig. 6.5.

7 Summary and Conclusions

In this work the Dark Matter subject has been studied mainly from a theoretical point of view. It is known that dark matter has not been observed as of yet, thus we present the most stringent experimental detection limits, direct and indirect upper bounds. Although its existence has not been confirmed, the evidences for it were several along the years, the first observation was carried by Fritz Zwicky at 1933 probing star velocities profiles, as we discussed in detail along other evidence examples.

For the theoretical description of *particle* dark matter, important concepts and frameworks have to be introduced. When we look at the universe at MegaParsec scales, one inevitably stumbles onto the observation that our universe is approximately isotropic and homogeneous, which requires understanding of general relativity and more specifically the FLRW cosmology. Still within the general theory for dark matter related calculations, we discussed the thermodynamics of the early universe as well as the Boltzmann equation for relic density evaluation alongside a related standard example for the sake of clarity.

For the remainder of the thesis, we then focused on thermal and non-thermal dark matter studies, which aim to generate the required amount of DM relic density, $\Omega_{\rm DM}h^2 \simeq 0.12$. On the first of the three works, we have computed (using recent lattice QCD results for the equation of state) the energy and entropy densities of the Standard Model with emphasis on temperatures around the deconfinement transition at $T_c = 154$ MeV. These results are described by the functions $g\,(T)$ and $h\,(T)$; the function $g_*^{1/2}\,(T)$ was also carefully treated, since it depends on the first derivative of h, and can be used in public codes for computing the relic density, e.g. `DarkSUSY`, `MicrOMEGAs` and `SuperIso`. Our predictions for the WIMP relic density differ from earlier treatments by up 9% (12%) for a thermal annihilation cross section $\langle\sigma v\rangle$ which is constant ($\propto T$), for masses between 3 and 15 GeV, for which range the QCD effects are most prominent and for which our detailed treatment of $g_*^{1/2}$ differs the most from the earlier treatments.

In special, we used our improved treatment of the thermodynamics of the early universe to update the calculation of the required $\langle\sigma v\rangle$ to reproduce the observed DM relic density, assuming the former to be independent on the temperature. The required value for 10 GeV $< m_\chi <$ 10 TeV is closer to $2\cdot10^{-26}$ cm^{3}s^{-1} than to the often cited $3\cdot10^{-26}$ cm^{3}s^{-1}, whereas for $m_\chi \lesssim 3$ GeV it exceeds $4\cdot10^{-26}$ cm^{3}s^{-1}. In the final part, we compared the required constant $\langle\sigma v\rangle$ with upper bounds on indirect detection that come from searches for energetic γ rays in WIMP annihilation as well as from CMB anisotropy constraints. The strongest bounds come from γ ray searches, which assume WIMP annihilation into hadronic or $\tau^+\tau^-$ states. We find that, for the most stringent channel $u\bar{u}$, the WIMP with $m_\chi > 100\,$GeV is allowed, while yielding the right relic density

amount.

For the other case study, we explained the evaluation of the DM relic density within a non-supersymmetric BSM model, assuming a majorana dark matter. The model is based on the local gauge symmetry $\mathrm{SU}(2)_L \otimes \mathrm{U}(1)_{Y'} \otimes \mathrm{U}(1)_{B-L}$ and there are four singlet scalars ϕ_i, one doublet scalar Φ and three right-handed neutrinos besides the SM field content. We find that one right-handed neutrino N_{DM} naturally transforms according to a global $\mathbb{Z}_2$ symmetry, following the equations of minimum. In the model rich scalar sector, we find a massless Goldstone boson J within the physical spectrum. Following the constraints of energy loss in stars through $\gamma + e^- \to e^- + J$; relativistic degrees of freedom N_{eff} of the universe; Z and Higgs invisible decay widths, the most important results were: the ratio of the new doublet VEV and the VEV of the four extra singlet scalars has to be in the range $\epsilon \equiv v_\Phi / v_\phi \lesssim 3.8 \cdot 10^{-4}$; and couplings κ_{H2} $\left(\text{coupling of } H^\dagger H \phi_2^\dagger \phi_2\right)$ and κ_{123} $\left(\text{coupling of } \phi_1 \phi_2 \left(\phi_3^*\right)^2\right)$ have to be in the ranges $\kappa_{H2} < 0.2$ and $-0.442 \lesssim \kappa_{123} \leq 0$. In addition, for $\epsilon \ll 1$ one is able to obtain analytical expressions for the scalar masses, largely simplifying the analysis.

For the DM production, we have worked basically with the free parameters κ_{H2}, κ_{123} and M_{DM}, which have been chosen because they play a very important role in determining both the N_{DM} annihilation cross section and the N_{DM} elastic scattering off the nucleon. Roughly speaking, we find that for $M_{\mathrm{DM}} \lesssim 500$ GeV, the right relic density is achieved around the resonance regions. For $M_{\mathrm{DM}} > 500$ GeV, regions other than resonances yield the correct relic density, due to the fact that the couplings DM-scalars are $\propto M_{\mathrm{DM}}/v_\phi$. κ_{123} strongly controls the trilinear scalar interactions, thus by making it bigger, it is possible to lower the DM relic profile curve and obtain more intersection points with the line $\Omega_{\mathrm{DM}} h^2 \simeq 0.12$. For DM direct detection (DD), the parameter κ_{H2} is the most relevant since it is the only one which effectively couples N_{DM} to the quarks in our model. We found that if we choose $\kappa_{H2} = 10^{-2}$, our entire curves are below LUX data, the most stringent limits upper bounds on spin-independent DD. If one takes however $\kappa_{H2} = 0.1$, it can still be lower than LUX, but this time the right relic density is only achieved above $M_{\mathrm{DM}} \sim 500 - 600$ GeV or at the resonances below 500 GeV.

Finally, after providing a brief framework on a deviation of the standard thermal WIMP scenario, we explore an example model where very massive particles might decay into electroweak particles, thus (roughly said) providing the necessary DM relic density. More specifically, we analyzed the production of neutralino (Wino, Bino and Higgsinos) DM candidates within a setup mixing the MSSM with the string theory motivated KL moduli sector whose AdS vacuum energy is uplifted with the help of the ISS model (a dual description to SQCD) as an F-term SUSY breaking. After an extensive description of the combined model, we obtain constraints on the ISS sector parameters M and h by imposing the condition of small entropy production ($s_\eta > s_{\phi_{\mathrm{ISS}}}$) on the ISS oscillating fields S_1, S_2 and Q_1. The small entropy requirement enables mainstream baryogenesis mechanisms to work besides easing the analysis on the fields time evolutions.

The main decay rates of the oscillating fields are found to be into: (gravitino pairs) $(Q_1, Q_2, S_2) \to \psi_{3/2} + \psi_{3/2}$; ($\chi_{S1}$ pairs) $S_1 \to \bar{\chi}_{S1} + \chi_{S1}$; ($\chi_{S1}$ pairs plus scalar) $Q_1 \to$

$\bar{\chi}_{S1} + \chi_{S1} + (\mathrm{Re}Q_2, \mathrm{Im}Q_2)$ and $Q_2 \to \bar{\chi}_{S1} + \chi_{S1} + \mathrm{Im}Q_2$. A detailed study of oscillations from the inflaton η and the ISS fields ϕ_{ISS} was then performed, where we noted S_1, S_2 and Q_1 as the relevant fields for the subsequent analysis in entropy dilution. (M, h) were then constrained to be within the triangle region formed approximately by the points $(10^{-6}, 2 \cdot 10^{-2})$, $(10^{-6}, 1)$ and $(5 \cdot 10^{-2}, 1)$, where the non-relativistic behaviour of the ISS products have been taken into account. As an important side issue, we treated the effect of the massless scalar $\mathrm{Im}Q_2$, whose relativistic degrees of freedom contribute to the quantity N_{eff} which measures the effective number of relativistic degrees of freedom of today, and obtained that its contribution can still be accounted in the observational uncertainty of N_{eff}.

Considering a neutralino dark matter χ, expressions for DM production via direct decays from gravitinos or χ_{S1} were obtained, as well as expressions for the subsequent decays of $\psi_{3/2}$ or χ_{S1} followed by neutralino annihilations. We compare these expressions with the constraints for small entropy production as well as constraints on the decay epochs of $\psi_{3/2}$ and χ_{S1} (so that they decay before BBN). The parameter space of M and h has been severely constrained, mainly because of the extremely small χ_{S1} decay rate (much smaller than the gravitino one). Through fig. 6.6, it can be noticed that this feature enables before-BBN decays for both particles while generating enough DM relic density in a reduced area of the parameter space, i.e. practically the region where χ_{S1} decays before BBN and after χ freezout. As discussed previously in more detail, while the gravitino could generate enough neutralinos, the before-BBN constraint for χ_{S1} forbids that solution. For χ_{S1} decays before BBN, sufficient DM can be generated, either through direct decays of χ_{S1} or through the subsequent annihilation of neutralinos. We conclude that for $m_\chi = 100$ GeV, the standard thermal scenario yields at most ~ 0.1 of the required DM relic density, hence the nonthermal scenario is able to provide the remaining ~ 0.9 DM content.

With this work, we believe a substantial understanding of the Dark Matter subject has been conveyed, providing the general and the expert reader with the main foundations of the topic as well as some specific current research studies on DM generation.

A Minimization equations

The general minimization conditions coming from $\partial V_{B-L}/\partial R_i = 0$, where V_{B-L} is the scalar potential in eq. (5.2.2) and $R_i = \{H_R^0,\, \Phi_R^0,\, \phi_{1R},\, \phi_{2R},\, \phi_{3R},\, \phi_{XR}\}$ are the neutral real components of the scalar fields, can be written as:

$$
\begin{aligned}
0 &= v_H \left(2\lambda_H v_H^2 + \kappa_{H\Phi} v_\Phi^2 + \kappa_{H1} v_{\phi_1}^2 + \kappa_{H2} v_{\phi_2}^2 + \kappa_{H3} v_{\phi_3}^2 + \kappa_{HX} v_{\phi_X}^2 - 2\mu_H^2\right) \\
&\quad -\sqrt{2}\kappa_{H\Phi X} v_\Phi v_{\phi_X}; && \text{(A.1)} \\
0 &= v_\Phi \left(\kappa_{H\Phi} v_H^2 + 2\lambda_\Phi v_\Phi^2 + \kappa_{\Phi 1} v_{\phi_1}^2 + \kappa_{\Phi 2} v_{\phi_2}^2 + \kappa_{\Phi 3} v_{\phi_3}^2 + \kappa_{\Phi X} v_{\phi_X}^2 - 2\mu_\Phi^2\right) \\
&\quad -\sqrt{2}\kappa_{H\Phi X} v_H v_{\phi_X}; && \text{(A.2)} \\
0 &= v_{\phi_1} \left(\kappa_{H1} v_H^2 + \kappa_{\Phi 1} v_\Phi^2 + 2\lambda_1 v_{\phi_1}^2 + \kappa_{12} v_{\phi_2}^2 + \kappa_{13} v_{\phi_3}^2 + \kappa_{1X} v_{\phi_X}^2 - 2\mu_1^2\right) \\
&\quad +v_{\phi_2} v_{\phi_3} \left(\kappa_{123} v_{\phi_3} + \kappa_{123X} v_{\phi_X}\right); && \text{(A.3)} \\
0 &= v_{\phi_2} \left(\kappa_{H2} v_H^2 + \kappa_{\Phi 2} v_\Phi^2 + \kappa_{12} v_{\phi_1}^2 + 2\lambda_2 v_{\phi_2}^2 + \kappa_{23} v_{\phi_3}^2 + \kappa_{2X} v_{\phi_X}^2 - 2\mu_2^2\right) \\
&\quad +v_{\phi_1} v_{\phi_3} \left(\kappa_{123} v_{\phi_3} + \kappa_{123X} v_{\phi_X}\right); && \text{(A.4)} \\
0 &= v_{\phi_3} \left(\kappa_{H3} v_H^2 + \kappa_{\Phi 3} v_\Phi^2 + \kappa_{13} v_{\phi_1}^2 + \kappa_{23} v_{\phi_2}^2 + 2\lambda_3 v_{\phi_3}^2 + \kappa_{3X} v_{\phi_X}^2 + 3\kappa'_{3X} v_{\phi_3} v_{\phi_X}\right. \\
&\quad \left. -2\mu_3^2\right) + v_{\phi_1} v_{\phi_2} \left(2\kappa_{123} v_{\phi_3} + \kappa_{123X} v_{\phi_X}\right); && \text{(A.5)} \\
0 &= v_{\phi_X} \left(\kappa_{HX} v_H^2 + \kappa_{\Phi X} v_\Phi^2 + \kappa_{1X} v_{\phi_1}^2 + \kappa_{2X} v_{\phi_2}^2 + \kappa_{3X} v_{\phi_3}^2 + 2\lambda_X v_{\phi_X}^2 - 2\mu_X^2\right) \\
&\quad -\sqrt{2}\kappa_{H\Phi X} v_\Phi v_H + v_{\phi_3} \left(\kappa_{123X} v_{\phi_1} v_{\phi_2} + \kappa'_{3X} v_{\phi_3}^2\right). && \text{(A.6)}
\end{aligned}
$$

Bibliography

[1] H. Fritzsch, M. Gell-Mann, and H. Leutwyler. Advantages of the color octet gluon picture. *Physics Letters B*, 47(4):365 – 368, 1973.

[2] J.J. Thomson. XL. Cathode rays. *The London, Edinburgh, and Dublin Philosophical Magazine and Journal of Science*, 44(269):293–316, 1897.

[3] E.J. Williams and G.E. Roberts. Evidence for transformation of mesotrons into electrons. *Nature*, 145(3664):102, 1940.

[4] M.L. Perl *et al.* Evidence for Anomalous Lepton Production in $e^+ - e^-$ Annihilation. *Phys. Rev. Lett.*, 35:1489–1492, Dec 1975.

[5] F. Reines and C.L. Cowan. Free Antineutrino Absorption Cross Section. I. Measurement of the Free Antineutrino Absorption Cross Section by Protons. *Phys. Rev.*, 113:273–279, 1959.

[6] G. Danby *et al.* Observation of High-Energy Neutrino Reactions and the Existence of Two Kinds of Neutrinos. *Phys. Rev. Lett.*, 9:36–44, 1962.

[7] G.S. Abrams *et al.* Measurements of Z-boson resonance parameters in e^+e^- annihilation. *Phys. Rev. Lett.*, 63:2173–2176, 1989.

[8] C.N. Yang and R.L. Mills. Conservation of Isotopic Spin and Isotopic Gauge Invariance. *Phys. Rev.*, 96:191–195, 1954.

[9] J. Goldstone. Field theories with Â« Superconductor Â» solutions. *Il Nuovo Cimento (1955-1965)*, 19(1):154–164, 1961.

[10] A. Salam and J.C. Ward. Vector field associated with the unitary theory of the Sakata model. *Il Nuovo Cimento (1955-1965)*, 20(2):419–421, 1961.

[11] S.L. Glashow. Partial-symmetries of weak interactions. *Nuclear Physics*, 22(4):579 – 588, 1961.

[12] P.W. Higgs. Broken Symmetries and the Masses of Gauge Bosons. *Phys. Rev. Lett.*, 13:508–509, 1964.

[13] F. Englert and R. Brout. Broken Symmetry and the Mass of Gauge Vector Mesons. *Phys. Rev. Lett.*, 13:321–323, 1964.

[14] G.S. Guralnik, C.R. Hagen, and T.W.B. Kibble. Global Conservation Laws and Massless Particles. *Phys. Rev. Lett.*, 13:585–587, 1964.

[15] G.'t Hooft. Renormalizable Lagrangians for massive Yang-Mills fields. *Nuclear Physics B*, 35(1):167 – 188, 1971.

[16] C.S. Wu, E. Ambler, R.W. Hayward, D.D. Hoppes, and R.P. Hudson. Experimental Test of Parity Conservation in Beta Decay. *Phys. Rev.*, 105:1413–1415, 1957.

[17] H. Albrecht *et al.* Observation of B0-B0 mixing. *Physics Letters B*, 192(1):245 – 252, 1987.

[18] D.P. Barber *et al.* Discovery of Three-Jet Events and a Test of Quantum Chromodynamics at PETRA. *Phys. Rev. Lett.*, 43:830–833, 1979.

[19] R. Brandelik *et al.* Evidence for planar events in e^+e^- annihilation at high energies. *Physics Letters B*, 86(2):243 – 249, 1979.

[20] C. Berger *et al.* Evidence for gluon bremsstrahlung in e^+e^- annihilations at high energies. *Physics Letters B*, 86(3):418 – 425, 1979.

[21] W. Bartel *et al.* Observation of planar three-jet events in e^+e^- annihilation and evidence for gluon bremsstrahlung. *Physics Letters B*, 91(1):142 – 147, 1980.

[22] M. Banner *et al.* Observation of single isolated electrons of high transverse momentum in events with missing transverse energy at the CERN pp collider. *Physics Letters B*, 122(5):476 – 485, 1983.

[23] G. Arnison *et al.* Experimental observation of isolated large transverse energy electrons with associated missing energy at $s = 540$ GeV. *Physics Letters B*, 122(1):103 – 116, 1983.

[24] G. Arnison *et al.* Experimental observation of lepton pairs of invariant mass around $95\text{GeV}/c^2$ at the CERN SPS collider. *Physics Letters B*, 126(5):398 – 410, 1983.

[25] P. Bagnaia *et al.* Evidence for $Z^0 \to e^+e^-$ at the CERN pp collider. *Physics Letters B*, 129(1):130 – 140, 1983.

[26] M. Breidenbach *et al.* Observed Behavior of Highly Inelastic Electron-Proton Scattering. *Phys. Rev. Lett.*, 23:935–939, 1969.

[27] J.D. Bjorken. Asymptotic Sum Rules at Infinite Momentum. *Phys. Rev.*, 179:1547–1553, 1969.

[28] R.P. Feynman. Very High-Energy Collisions of Hadrons. *Phys. Rev. Lett.*, 23:1415–1417, 1969.

[29] J.J. Aubert *et al.* Experimental Observation of a Heavy Particle J. *Phys. Rev. Lett.*, 33:1404–1406, 1974.

[30] J.E. Augustin *et al.* Discovery of a Narrow Resonance in e^+e^- Annihilation. *Phys. Rev. Lett.*, 33:1406–1408, 1974.

[31] S.W. Herb *et al.* Observation of a Dimuon Resonance at 9.5 GeV in 400-GeV Proton-Nucleus Collisions. *Phys. Rev. Lett.*, 39:252–255, 1977.

[32] [CDF Collaboration] F. Abe *et al.* Observation of Top Quark Production in $\overline{p}p$ Collisions with the Collider Detector at Fermilab. *Phys. Rev. Lett.*, 74:2626–2631, 1995.

[33] [Atlas collaboration] G. Aad *et al.* Observation of a new particle in the search for the Standard Model Higgs boson with the ATLAS detector at the LHC. *Physics Letters B*, 716(1):1 – 29, 2012.

[34] [CMS Collaboration] S. Chatrchyan *et al.* Observation of a new boson at a mass of 125 GeV with the CMS experiment at the LHC. *Physics Letters B*, 716(1):30 – 61, 2012.

[35] [Super-Kamiokande Collaboration] Y. Fukuda *et al.* Evidence for Oscillation of Atmospheric Neutrinos. *Phys. Rev. Lett.*, 81:1562–1567, 1998.

[36] [SNO Collaboration] Q.R. Ahmad *et al.* Direct Evidence for Neutrino Flavor Transformation from Neutral-Current Interactions in the Sudbury Neutrino Observatory. *Phys. Rev. Lett.*, 89:011301, 2002.

[37] M.E. Peskin. Dark Matter and Particle Physics. *Journal of the Physical Society of Japan*, 76(11):111017–111017, 2007.

[38] F. Zwicky. The redshift of extragalactic nebulae. *Helv. Phys. Acta*, 6:110, 1933.

[39] S. Smith. The mass of the virgo cluster. *The Astrophysical Journal*, 83:23, 1936.

[40] P. Rosati, S. Borgani, and C. Norman. The Evolution of X-Ray Clusters of Galaxies. *Annual Review of Astronomy and Astrophysics*, 40(1):539–577, 2002.

[41] Y. Sofue and V. Rubin. Rotation Curves of Spiral Galaxies. *Annual Review of Astronomy and Astrophysics*, 39(1):137–174, 2001.

[42] V. Rubin, N. Thonnard, and W. Ford Jr. NGC 3067-Additional evidence for non-luminous matter. *The Astronomical Journal*, 87:477–485, 1982.

[43] V. Trimble. Existence and nature of dark matter in the universe. *Annual review of astronomy and astrophysics*, 25(1):425–472, 1987.

[44] [WMAP Collaboration] G. Hinshaw *et al.* Nine-year Wilkinson Microwave Anisotropy Probe (WMAP) Observations: Cosmological Parameter Results. *The Astrophysical Journal Supplement Series*, 208(2):19, 2013.

[45] [Planck Collaboration] P.A.R. Ade *et al.* Planck 2015 results. XIII. Cosmological parameters. *Astron. Astrophys.*, 594:A13, 2016.

[46] R.H. Sanders and S.S. McGaugh. Modified Newtonian Dynamics as an Alternative to Dark Matter. *Annual Review of Astronomy and Astrophysics*, 40(1):263–317, 2002.

[47] D. Clowe *et al.* A Direct Empirical Proof of the Existence of Dark Matter. *The Astrophysical Journal Letters*, 648(2):L109, 2006.

[48] [SNCP collaboration] S. Perlmutter *et al.* Measurements of Ω and Λ from 42 High-Redshift Supernovae. *The Astrophysical Journal*, 517(2):565, 1999.

[49] [High z Supernova Search Team] A.G. Riess *et al.* Observational Evidence from Supernovae for an Accelerating Universe and a Cosmological Constant. *The Astronomical Journal*, 116(3):1009, 1998.

[50] [WMAP collaboration] E. Komatsu *et al.* Seven-year Wilkinson Microwave Anisotropy Probe (WMAP) Observations: Cosmological Interpretation. *The Astrophysical Journal Supplement Series*, 192(2):18, 2011.

[51] [SDSS collaboration] M. Tegmark *et al.* Cosmological parameters from SDSS and WMAP. *Phys. Rev. D*, 69:103501, 2004.

[52] [SDSS collaboration] D.J. Eisenstein *et al.* Detection of the Baryon Acoustic Peak in the Large-Scale Correlation Function of SDSS Luminous Red Galaxies. *The Astrophysical Journal*, 633(2):560, 2005.

[53] B. Jain and A. Taylor. Cross-Correlation Tomography: Measuring Dark Energy Evolution with Weak Lensing. *Phys. Rev. Lett.*, 91:141302, 2003.

[54] M. Boylan-Kolchin, J.S. Bullock, and M. Kaplinghat. The Milky Way's bright satellites as an apparent failure of ΛCDM. *Monthly Notices of the Royal Astronomical Society*, 422:1203–1218, 2012.

[55] A. Klypin, A.V. Kravtsov, O. Valenzuela, and F. Prada. Where Are the Missing Galactic Satellites? *The Astrophysical Journal*, 522(1):82, 1999.

[56] B. Moore *et al.* Dark Matter Substructure within Galactic Halos. *The Astrophysical Journal Letters*, 524(1):L19, 1999.

[57] K. Bamba, S. Capozziello, S. Nojiri, and S.D. Odintsov. Dark energy cosmology: the equivalent description via different theoretical models and cosmography tests. *Astrophysics and Space Science*, 342(1):155–228, 2012.

[58] M. Srednicki, R. Watkins, and K.A. Olive. Calculations of relic densities in the early universe. *Nuclear Physics B*, 310(3):693–713, 1988.

[59] P. Gondolo and G. Gelmini. Cosmic abundances of stable particles: Improved analysis. *Nuclear Physics B*, 360(1):145 – 179, 1991.

[60] E. Kolb and M. Turner. *The early universe*, volume 69. Westview press, 1994.

[61] K. Griest and D. Seckel. Three exceptions in the calculation of relic abundances. *Phys. Rev. D*, 43:3191–3203, 1991.

[62] L. Baudis. Direct Detection of Cold Dark Matter. 2007. 0711.3788.

[63] [XENON Collaboration] E. Aprile *et al.* First Dark Matter Search Results from the XENON1T Experiment. *Phys. Rev. Lett.*, 119:181301, 2017.

[64] [LUX Collaboration] D.S. Akerib *et al.* Results from a Search for Dark Matter in the Complete LUX Exposure. *Phys. Rev. Lett.*, 118:021303, 2017.

[65] [PandaX-II Collaboration] A. Tan *et al.* Dark Matter Results from First 98.7 Days of Data from the PandaX-II Experiment. *Phys. Rev. Lett.*, 117:121303, 2016.

[66] [CDMS Collaboration] Z. Ahmed *et al.* Search for Weakly Interacting Massive Particles with the First Five-Tower Data from the Cryogenic Dark Matter Search at the Soudan Underground Laboratory. *Phys. Rev. Lett.*, 102:011301, 2009.

[67] [XENON collaboration] E. Aprile *et al.* Dark Matter Results from 225 Live Days of XENON100 Data. *Phys. Rev. Lett.*, 109:181301, 2012. arXiv:1207.5988 [astro-ph.CO].

[68] P. Agrawal, Z. Chacko, C. Kilic, and R.K. Mishra. A Classification of Dark Matter Candidates with Primarily Spin-Dependent Interactions with Matter. 2010. arXiv:1003.1912.

[69] J.M. Losecco *et al.* Limits on the flux of energetic neutrinos from the sun. *Physics Letters B*, 188(3):388 – 392, 1987.

[70] M. Mori *et al.* Search for neutralino dark matter heavier than the W boson at Kamiokande. *Phys. Rev. D*, 48:5505–5518, 1993.

[71] [MACRO Collaboration] M. Ambrosio *et al.* Limits on dark matter WIMPs using upward-going muons in the MACRO detector. *Phys. Rev. D*, 60:082002, 1999.

[72] [The Super-Kamiokande Collaboration] S. Desai *et al.* Search for dark matter WIMPs using upward through-going muons in Super-Kamiokande. *Phys. Rev. D*, 70:083523, 2004.

[73] [AMANDA Collaboration] J. Ahrens *et al.* Limits to the muon flux from WIMP annihilation in the center of the Earth with the AMANDA detector. *Phys. Rev. D*, 66:032006, 2002.

[74] V. Aynutdinov et al. The Baikal neutrino experiment: Status, selected physics results, and perspectives. *Nuclear Instruments and Methods in Physics Research Section A: Accelerators, Spectrometers, Detectors and Associated Equipment*, 588(1):99 – 106, 2008. Proceedings of the First International Conference on Astroparticle Physics.

[75] O. Adriani *et al.* Cosmic-Ray Positron Energy Spectrum Measured by PAMELA. *Phys. Rev. Lett.*, 111:081102, 2013.

[76] [Fermi-LAT Collaboration] M. Ackermann *et al.* Measurement of Separate Cosmic-Ray Electron and Positron Spectra with the Fermi Large Area Telescope. *Phys. Rev. Lett.*, 108:011103, 2012.

[77] [AMS Collaboration] M. Aguilar *et al.* First Result from the Alpha Magnetic Spectrometer on the International Space Station: Precision Measurement of the Positron Fraction in Primary Cosmic Rays of 0.5–350 GeV. *Phys. Rev. Lett.*, 110:141102, 2013.

[78] A. Geringer-Sameth and S.M. Koushiappas. Exclusion of Canonical Weakly Interacting Massive Particles by Joint Analysis of Milky Way Dwarf Galaxies with Data from the Fermi Gamma-Ray Space Telescope. *Phys. Rev. Lett.*, 107:241303, 2011.

[79] [Fermi-LAT Collaboration] M. Ackermann *et al.* Constraining Dark Matter Models from a Combined Analysis of Milky Way Satellites with the Fermi Large Area Telescope. *Phys. Rev. Lett.*, 107:241302, 2011.

[80] [Fermi-LAT Collaboration] M. Ackermann *et al.* Dark matter constraints from observations of 25 Milky Way satellite galaxies with the Fermi Large Area Telescope. *Phys. Rev. D*, 89:042001, 2014.

[81] [Fermi-LAT Collaboration] M. Ackermann *et al.* Searching for Dark Matter Annihilation from Milky Way Dwarf Spheroidal Galaxies with Six Years of Fermi Large Area Telescope Data. *Phys. Rev. Lett.*, 115:231301, 2015.

[82] X. Chen and M. Kamionkowski. Particle decays during the cosmic dark ages. *Phys. Rev. D*, 70:043502, 2004.

[83] N. Padmanabhan and D.P. Finkbeiner. Detecting dark matter annihilation with CMB polarization: Signatures and experimental prospects. *Phys. Rev. D*, 72:023508, 2005.

[84] S. Galli, F. Iocco, G. Bertone, and A. Melchiorri. Updated CMB constraints on dark matter annihilation cross sections. *Phys. Rev. D*, 84:027302, 2011.

[85] M. Drees, F. Hajkarim, and E.R. Schmitz. The effects of QCD equation of state on the relic density of WIMP dark matter. *Journal of Cosmology and Astroparticle Physics*, 2015(06):025, 2015.

[86] B.L. Sánchez-Vega and E.R. Schmitz. Fermionic dark matter and neutrino masses in a $\mathcal{B}-\mathcal{L}$ model. *Phys. Rev. D*, 92:053007, 2015.

[87] J. Ellis, J.S. Hagelin, D.V. Nanopoulos, K. Olive, and M. Srednicki. Supersymmetric relics from the big bang. *Nuclear Physics B*, 238(2):453–476, 1984.

[88] Z. Fodor. Electroweak phase transitions. *Nuclear Physics B - Proceedings Supplements*, 83-84:121–125, 2000. Proceedings of the XVIIth International Symposium on Lattice Field Theory.

[89] K. Kajantie, M. Laine, K. Rummukainen, and M. Shaposhnikov. Is There a Hot Electroweak Phase Transition at $m_H \gtrsim m_W$? *Phys. Rev. Lett.*, 77:2887–2890, Sep 1996.

[90] F. Csikor, Z. Fodor, and J. Heitger. End Point of the Hot Electroweak Phase Transition. *Phys. Rev. Lett.*, 82:21–24, Jan 1999.

[91] Y. Aoki, G. Endrodi, Z. Fodor, S.D. Katz, and K.K. Szabo. The order of the quantum chromodynamics transition predicted by the standard model of particle physics. *Nature*, 443:675, 2006.

[92] [HotQCD Collaboration] A. Bazavov *et al.* Equation of state in $(2+1)$-flavor QCD. *Phys. Rev. D*, 90:094503, Nov 2014.

[93] S. Borsányi, Z. Fodor, C. Hoelbling, S.D. Katz, S. Krieg, and K.K. Szabo. Full result for the QCD equation of state with 2+1 flavors. *Physics Letters B*, 730:99–104, 2014.

[94] M. Laine and Y. Schröder. Quark mass thresholds in QCD thermodynamics. *Phys. Rev. D*, 73:085009, 2006.

[95] S. Borsányi *et al.* The QCD equation of state with dynamical quarks. *Journal of High Energy Physics*, 2010(11):77, 2010.

[96] [HPQCD Collaboration] C.T.H. Davies *et al.* Precise Charm to Strange Mass Ratio and Light Quark Masses from Full Lattice QCD. *Phys. Rev. Lett.*, 104:132003, 2010.

[97] [Particle Data Group] K.A. Olive *et al.* Review of Particle Physics. *Chinese Physics C*, 38(9):090001, 2014.

[98] P. Huovinen and P. Petreczky. QCD equation of state and hadron resonance gas. *Nuclear Physics A*, 837(1):26 – 53, 2010.

[99] K.A. Olive. The thermodynamics of the quark-hadron phase transition in the early universe. *Nuclear Physics B*, 190(3):483–503, 1981.

[100] K.A. Olive, D.N. Schramm, and G. Steigman. Limits on new superweakly interacting particles from primordial nucleosynthesis. *Nuclear Physics B*, 180(3):497–515, 1981.

[101] G. Mangano, G. Miele, S. Pastor, T. Pinto, O. Pisanti, and P.D. Serpico. Relic neutrino decoupling including flavour oscillations. *Nuclear Physics B*, 729(1):221–234, 2005.

[102] S. Pastor and J. Lesgourgues. Neutrino Mass from Cosmology. *Advances in High Energy Physics*, 2012:34, 2012.

[103] P. Gondolo, J. Edsjö, P. Ullio, L. Bergström, M. Schelke, and E.A. Baltz. DarkSUSY: computing supersymmetric dark matter properties numerically. *Journal of Cosmology and Astroparticle Physics*, 2004(07):008, 2004.

[104] G. Bélanger, F. Boudjema, A. Pukhov, and A. Semenov. micrOMEGAs_3: A program for calculating dark matter observables. *Computer Physics Communications*, 185(3):960–985, 2014.

[105] A. Arbey and F. Mahmoudi. SuperIso Relic v3.0: A program for calculating relic density and flavour physics observables: Extension to NMSSM. *Computer Physics Communications*, 182(7):1582–1583, 2011.

[106] M. Hindmarsh and O. Philipsen. Dark matter of weakly interacting massive particles and the QCD equation of state. *Phys. Rev. D*, 71:087302, 2005.

[107] F. Karsch, E. Laermann, and A. Peikert. The pressure in 2, 2+1 and 3 flavour QCD. *Physics Letters B*, 478(4):447–455, 2000.

[108] K. Kajantie, M. Laine, K. Rummukainen, and Y. Schröder. Pressure of hot QCD up to $g^6\ln(1/g)$. *Phys. Rev. D*, 67:105008, May 2003.

[109] G. Boyd *et al.* Thermodynamics of SU(3) lattice gauge theory. *Nuclear Physics B*, 469(3):419–444, 1996.

[110] B. Beinlich, F. Karsch, E. Laermann, and A. Peikert. String tension and thermodynamics with tree level and tadpole improved actions. *The European Physical Journal C*, 6(1):133–140, Jan 1999.

[111] [CP-PACS Collaboration] M. Okamoto *et al.* Equation of state for pure SU(3) gauge theory with renormalization group improved action. *Phys. Rev. D*, 60:094510, Oct 1999.

[112] [CP-PACS Collaboration] Y. Namekawa *et al.* Thermodynamics of SU(3) gauge theory on anisotropic lattices. *Phys. Rev. D*, 64:074507, 2001.

[113] R.V. Gavai, S. Gupta, and S. Mukherjee. Speed of sound and specific heat in the QCD plasma: Hydrodynamics, fluctuations, and conformal symmetry. *Phys. Rev. D*, 71:074013, 2005.

[114] G. Steigman, B. Dasgupta, and J.F. Beacom. Precise relic WIMP abundance and its impact on searches for dark matter annihilation. *Phys. Rev. D*, 86:023506, 2012.

[115] L. Goodenough and D. Hooper. Possible Evidence For Dark Matter Annihilation In The Inner Milky Way From The Fermi Gamma Ray Space Telescope. 2009. 0910.2998.

[116] D. Hooper and L. Goodenough. Dark matter annihilation in the Galactic Center as seen by the Fermi Gamma Ray Space Telescope. *Physics Letters B*, 697(5):412 – 428, 2011.

[117] T. Daylan *et al.* The characterization of the gamma-ray signal from the central Milky Way: A case for annihilating dark matter. *Physics of the Dark Universe*, 12:1 – 23, 2016.

[118] F. Calore, I. Cholis, C. McCabe, and C. Weniger. A tale of tails: Dark matter interpretations of the Fermi GeV excess in light of background model systematics. *Phys. Rev. D*, 91:063003, 2015.

[119] Q. Yuan and B. Zhang. Millisecond pulsar interpretation of the Galactic center gamma-ray excess. *Journal of High Energy Astrophysics*, 3-4:1 – 8, 2014.

[120] E. Carlson and S. Profumo. Cosmic ray protons in the inner Galaxy and the Galactic Center gamma-ray excess. *Phys. Rev. D*, 90:023015, 2014.

[121] N. Mirabal. Annihilating dark matter or noise?: A statistical examination of the Fermi GeV excess around the Galactic Centre. 2014. 1411.7410.

[122] M.S. Madhavacheril, N. Sehgal, and T.R. Slatyer. Current dark matter annihilation constraints from CMB and low-redshift data. *Phys. Rev. D*, 89:103508, 2014.

[123] T.R. Slatyer, N. Padmanabhan, and D.P. Finkbeiner. CMB constraints on WIMP annihilation: Energy absorption during the recombination epoch. *Phys. Rev. D*, 80:043526, 2009.

[124] G. Steigman. CMB constraints on the thermal WIMP mass and annihilation cross section. *Phys. Rev. D*, 91:083538, 2015.

[125] J.C. Montero and V. Pleitez. Gauging U(1) symmetries and the number of right-handed neutrinos. *Phys.Lett.*, B675:64–68, 2009.

[126] J.C. Montero and B.L. Sánchez-Vega. Neutrino masses and the scalar sector of a B-L extension of the standard model. *Phys.Rev.*, D84:053006, 2011.

[127] S.L. Glashow and S. Weinberg. Natural conservation laws for neutral currents. *Phys. Rev. D*, 15:1958–1965, 1977.

[128] T.P. Cheng and M. Sher. Mass-matrix ansatz and flavor nonconservation in models with multiple Higgs doublets. *Phys. Rev. D*, 35:3484–3491, 1987.

[129] G. Gilbert. Wormhole-induced proton decay. *Nuclear Physics B*, 328(1):159 – 170, 1989.

[130] R. Holman, S.D.H. Hsu, T.W. Kephart, E.W. Kolb, R. Watkins, and L.M. Widrow. Solutions to the strong-CP problem in a world with gravity. *Physics Letters B*, 282(1-2):132 – 136, 1992.

[131] M. Kamionkowski and J. March-Russell. Planck-scale physics and the Peccei-Quinn mechanism . *Physics Letters B*, 282(1-2):137 – 141, 1992.

[132] E.Kh. Akhmedov *et al.* Planck scale effects on the majoron. *Physics Letters B*, 299(1-2):90–93, 1993. arXiv:hep-ph/9209285.

[133] J.C. Montero and B.L. Sánchez-Vega. Natural Peccei-Quinn symmetry in the 3-3-1 model with a minimal scalar sector. *Phys. Rev. D*, 84:055019, 2011.

[134] D.A. Dicus, E.W. Kolb, V.L. Teplitz, and R.V. Wagoner. Astrophysical bounds on the masses of axions and Higgs particles. *Phys. Rev. D*, 18:1829–1834, 1978.

[135] [Particle Data Group] G.G. Raffelt. Axions and other very light bosons: part II (astrophysical constraints). 2006.

[136] M.C. Gonzalez-Garcia and Y. Nir. Implications of a Precise Measurement of the Z Width on the Spontaneous Breaking of Global Symmetries. *Phys.Lett.*, B232:383, 1989.

[137] S. Weinberg. Goldstone Bosons as Fractional Cosmic Neutrinos. *Phys. Rev. Lett.*, 110:241301, 2013.

[138] [SuperCDMS collaboration] R. Agnese *et al.* Search for Low-Mass Weakly Interacting Massive Particles Using Voltage-Assisted Calorimetric Ionization Detection in the SuperCDMS Experiment. *Phys. Rev. Lett.*, 112:041302, 2014. arXiv:1309.3259 [physics.ins-det].

[139] A. Alloul *et al.* FeynRules 2.0 - A complete toolbox for tree-level phenomenology. *Computer Physics Communications*, 185(8):2250–2300, 2014. arXiv:1310.1921 [hep-ph].

[140] A. Belyaev, N.D. Christensen, and A. Pukhov. CalcHEP 3.4 for collider physics within and beyond the Standard Model. *Computer Physics Communications*, 184(7):1729–1769, 2013. arXiv:1207.6082 [hep-ph].

[141] G. Bélanger *et al.* micrOMEGAs 4.1: Two dark matter candidates. *Computer Physics Communications*, 192(0):322–329, 2015. arXiv:1407.6129 [hep-ph].

[142] J. Erler *et al.* Improved constraints on Z' bosons from electroweak precision data. *Journal of High Energy Physics*, 2009(08):017, 2009. arXiv:0906.2435 [hep-ph].

[143] F. del Aguila, J. de Blas, and M. Pérez-Victoria. Electroweak limits on general new vector bosons. *Journal of High Energy Physics*, 2010(9), 2010. arXiv:1005.3998 [hep-ph].

[144] R. Diener, S. Godfrey, and I. Turan. Constraining extra neutral gauge bosons with atomic parity violation measurements. *Phys. Rev. D*, 86:115017, 2012. arXiv:1111.4566 [hep-ph].

[145] B.L. Sánchez-Vega, J.C. Montero, and E.R. Schmitz. Complex scalar dark matter in a B-L model. *Phys. Rev. D*, 90:055022, 2014.

[146] T. Appelquist, B.A. Dobrescu, and A.R. Hopper. Nonexotic neutral gauge bosons. *Phys. Rev. D*, 68:035012, 2003. arXiv:hep-ph/0212073.

[147] M. Carena *et al.* Z' gauge bosons at the Fermilab Tevatron. *Phys. Rev. D*, 70:093009, 2004. arXiv:hep-ph/0408098.

[148] J. Ellis and T. You. Updated global analysis of Higgs couplings. *Journal of High Energy Physics*, 2013(6), 2013. arXiv:1303.3879 [hep-ph].

[149] P.P. Giardino, K. Kannike, I. Masina, M. Raidal, and A. Strumia. The universal Higgs fit. *Journal of High Energy Physics*, 2014(5), 2014.

[150] [Atlas collaboration] G. Aad *et al.* Search for Invisible Decays of a Higgs Boson Produced in Association with a Z Boson in ATLAS. *Phys. Rev. Lett.*, 112:201802, 2014.

[151] [CMS collaboration] S. Chatrchyan *et al.* Search for invisible decays of Higgs bosons in the vector boson fusion and associated ZH production modes. *The European Physical Journal C*, 74(8), 2014.

[152] [LUX Collaboration] D.S. Akerib *et al.* First Results from the LUX Dark Matter Experiment at the Sanford Underground Research Facility. *Phys. Rev. Lett.*, 112:091303, 2014.

[153] [COUPP collaboration] E. Behnke *et al.* First dark matter search results from a 4-kg $CF_3\mathbf{I}$ bubble chamber operated in a deep underground site. *Phys. Rev. D*, 86:052001, 2012. arXiv:1204.3094.

[154] [SIMPLE collaboration] M. Felizardo *et al.* Final Analysis and Results of the Phase II SIMPLE Dark Matter Search. *Phys. Rev. Lett.*, 108:201302, 2012. arXiv:1106.3014.

[155] G.F. Giudice, E.W. Kolb, and A. Riotto. Largest temperature of the radiation era and its cosmological implications. *Phys. Rev. D*, 64:023508, 2001.

[156] G.L. Kane, P. Kumar, B.D. Nelson, and B. Zheng. Dark matter production mechanisms with a nonthermal cosmological history: A classification. *Phys. Rev. D*, 93:063527, 2016.

[157] T.C. da C. Guio and E.R. Schmitz. Dark matter from a F-term dynamical SUSY breaking sector dual to $\mathcal{N} = 1$ SQCD. 2018. arXiv:1805.01521.

[158] S. Kachru, R. Kallosh, A. Linde, and S.P. Trivedi. de Sitter vacua in string theory. *Phys. Rev. D*, 68:046005, 2003.

[159] R. Kallosh and A. Linde. Landscape, the scale of SUSY breaking, and inflation. *Journal of High Energy Physics*, 2004(12):004, 2004.

[160] R. Kallosh and A. Linde. O'KKLT. *Journal of High Energy Physics*, 2007(02):002, 2007.

[161] K. Intriligator, N. Seiberg, and D. Shih. Dynamical SUSY breaking in meta-stable vacua. *Journal of High Energy Physics*, 2006(04):021, 2006.

[162] E. Dudas, A. Linde, Y. Mambrini, A. Mustafayev, and K.A. Olive. Strong moduli stabilization and phenomenology. *The European Physical Journal C*, 73(1):2268, 2013.

[163] E. Witten. Dynamical breaking of supersymmetry. *Nuclear Physics B*, 188(3):513 – 554, 1981.

[164] G.F. Giudice and R. Rattazzi. Theories with gauge-mediated supersymmetry breaking. *Physics Reports*, 322(6):419 – 499, 1999.

[165] N. Seiberg. Electric-magnetic duality in supersymmetric non-Abelian gauge theories. *Nuclear Physics B*, 435(1):129 – 146, 1995.

[166] G.F. Giudice and A. Masiero. A natural solution to the μ-problem in supergravity theories. *Physics Letters B*, 206(3):480 – 484, 1988.

[167] J.L. Evans, M. Ibe, K.A. Olive, and T.T. Yanagida. Universality in pure gravity mediation. *The European Physical Journal C*, 73(7):2468, 2013.

[168] J.L. Evans, M. Ibe, K.A. Olive, and T.T. Yanagida. Non-universalities in pure gravity mediation. *The European Physical Journal C*, 73(10):2611, 2013.

[169] R. Kallosh, A. Linde, K.A. Olive, and T. Rube. Chaotic inflation and supersymmetry breaking. *Phys. Rev. D*, 84:083519, 2011.

[170] A. Linde, Y. Mambrini, and K.A. Olive. Supersymmetry breaking due to moduli stabilization in string theory. *Phys. Rev. D*, 85:066005, 2012.

[171] I. Affleck and M. Dine. A new mechanism for baryogenesis. *Nuclear Physics B*, 249(2):361 – 380, 1985.

[172] M.A.G. Garcia and K.A. Olive. Affleck-Dine baryogenesis and inflation in supergravity with strongly stabilized moduli. *Journal of Cosmology and Astroparticle Physics*, 2013(09):007, 2013.

[173] T. Konstandin. Quantum transport and electroweak baryogenesis. *Physics-Uspekhi*, 56(8):747, 2013.

[174] D.E. Morrissey and M.J. Ramsey-Musolf. Electroweak baryogenesis. *New Journal of Physics*, 14(12):125003, 2012.

[175] T. Moroi. Effects of the gravitino on the inflationary universe. *(PhD thesis) Tohoku U.*, 1995. arXiv: hep-ph/9503210.

[176] R. Barbier, C. Bérat, M. Besançon, M. Chemtob, A. Deandrea, E. Dudas, P. Fayet, S. Lavignac, G. Moreau, E. Perez, and Y. Sirois. R-Parity-violating supersymmetry. *Physics Reports*, 420(1):1 – 195, 2005.

[177] J.L. Evans, M.A.G. Garcia, and K.A. Olive. The moduli and gravitino (non)-problems in models with strongly stabilized moduli. *Journal of Cosmology and Astroparticle Physics*, 2014(03):022, 2014.

[178] M. Dine, L. Randall, and S. Thomas. Baryogenesis from flat directions of the supersymmetric standard model. *Nuclear Physics B*, 458(1):291 – 323, 1996.

[179] A. Linde. Relaxing the cosmological moduli problem. *Phys. Rev. D*, 53:R4129–R4132, 1996.

[180] K. Nakayama, F. Takahashi, and T.T. Yanagida. Adiabatic solution to the Polonyi/moduli problem. *Phys. Rev. D*, 84:123523, 2011.

[181] G.D. Coughlan, W. Fischler, E.W. Kolb, S. Raby, and G.G. Ross. Cosmological problems for the polonyi potential. *Physics Letters B*, 131(1):59 – 64, 1983.

[182] S. Nakamura and M. Yamaguchi. A note on Polonyi problem. *Physics Letters B*, 655(3):167 – 171, 2007.

[183] J. Polonyi. *Budapest preprint KFKI-1977-93 (unpublished)*, 1977.

[184] M. Bolz, A. Brandenburg, and W. Buchmüller. Thermal production of gravitinos. *Nuclear Physics B*, 606(1):518 – 544, 2001.

[185] M. Kawasaki, K. Kohri, T. Moroi, and A. Yotsuyanagi. Big-bang nucleosynthesis and gravitinos. *Phys. Rev. D*, 78:065011, 2008.

[186] H.P. Nilles, K.A. Olive, and M. Peloso. The inflatino problem in supergravity inflationary models. *Physics Letters B*, 522(3):304 – 314, 2001.

[187] T. Moroi and L. Randall. Wino cold dark matter from anomaly mediated SUSY breaking. *Nuclear Physics B*, 570(1):455 – 472, 2000.

[188] T. Moroi, M. Yamaguchi, and T. Yanagida. On the solution to the polonyi problem with O(10 TeV) gravitino mass in supergravity. *Physics Letters B*, 342(1):105 – 110, 1995.

[189] M. Drees and M.M. Nojiri. Neutralino relic density in minimal $N = 1$ supergravity. *Phys. Rev. D*, 47:376–408, 1993.